Steps towards Silicon Optoelectronics

A thesis presented by

Artem Starovoytov

M.Sc.(Moscow Institute of Physics and Technology, 1994)

to

The School of Applied Sciences

in partial fulfillment of the requirements

for the degree of

Doctor of Philosophy

in the subject of Physics

De Montfort University

Leicester, UK

July, 1999

Abstract

This thesis addresses the issue of a potential future microelectronics technology, namely the possibility of utilising the optical properties of nanocrystalline silicon for optoelectronic circuits. The subject is subdivided into three chapters.

Chapter 1 is an introduction. It formulates the oncoming problem for microelectronic development, explains the basics of Integrated Optoelectronics, introduces porous silicon as a new light-emitting material and gives a brief review of other competing light-emitting material systems currently under investigation. Examples of existing porous silicon devices are given.

Chapter 2 reviews the basic physics relevant to the subject of this thesis and informs on the present situation in this field of research, including both experimental and theoretical knowledge gained up-to-date. The chapter provides the necessary background for correct interpretation of the results reported in Chapter 3 and for a realistic decision on the direction for future work.

Chapter 3 describes my own experimental and computational results within the framework of the subject, obtained at De Montfort University. These include: one-step preparation of laterally structured porous silicon with photoluminescence and microscopy characterisation, Raman spectroscopy of porous silicon, a polarisation study of the photoluminescence from porous silicon, computer simulations of the conductivity of two-component media and of laser focused atomic deposition for nanostructure fabrication.

Thus, this thesis makes a dual contribution to the chosen field: it summarises the present knowledge on the possibility of utilising optical properties of nanocrystalline silicon in silicon-based electronics, and it reports new results within the framework of the subject. The main conclusion is that due to its promising optoelectronic properties nanocrystalline silicon remains a prospective competitor for the cheapest and fastest microelectronics of the next century.

Acknowledgments

The author acknowledges his supervisor Professor Sue Bayliss (Solid State Research Centre) for constant help in the form of scientific advice and organisational actions, his second supervisor Professor Nick Philips (Modern Optics) for allowing use of his facilities, all the technical staff of the University (including R.G.Wright, D.Bazeley, C.Warrington and A.Woodford), all the other students in the laboratory for routine help, and De Montfort University as a whole (including Applied Sciences School staff) for giving him the opportunity to do this research.

Separate thanks to Lorenzo Pavesi from University of Trento, to my supervisor Sue Bayliss and to the EU Inco-Copernicus, for choosing me to participate in the "Silicon-Based Microphotonics" Summer 1998 course of the "Enrico Fermi International School of Physics" held by the Italian Physical Society in Varenna (Italy).

Contents

List of Figures

List of Tables

Chapter 1
Introduction

"A dramatic improvement could be realized if architectures employing fine-line on-chip optical interconnects were available. However, development of the devices having high efficiency electro-optical conversion for receiving and transmitting signals is also required."

From the SIA 1997 roadmap

In this chapter:

This chapter deals not with physics but with the motivation for the chosen subject. It formulates the oncoming problem for microelectronic development, explains the basics of Integrated Optoelectronics, introduces porous silicon as a new light-emitting material, and gives a review of light-emitting material systems currently under investigation, thus justifying the quest for silicon-based light-emitters. Nanocrystalline silicon is introduced as probably the most prominent competitor for this.

1.1 Oncoming problems for Modern Electronics

The history of computer technology is impossible to separate from the history of civilisation as a whole. The use of microelectronics has been extended to all product categories: from mainframe computers to automobiles and house appliances. Semiconductor devices are now the basis of our business efficiency, of industrial competitiveness, and have pervaded our homes, offices and cars. The corner-stone of this expansion is the tremendous increase in performance and the reduction in cost of information processing and storage.

Three major revolutionary break-through events can be distinguished in the past: first, the invention of electronic digital data processing (1940s), second, the invention of the semiconductor transistor (in 1950's), and third, the development of integrated circuit technology in the late 1960s, allowing simultaneous build-up of millions of devices on one wafer to form microprocessors and memory chips. During the last 25 years, the capacity of memory chips increased by a factor of 64000 and the cost per bit now stands at 10^{-7} ECU; microprocessor chips have improved their performance 3000-fold and the cost per transistor is now less than 10^{-5} ECU. This evolution was accompanied by an exponential increase in factory capital cost, which increased from \$10 million in 1970 to more than \$1 billion in 1994. It is in fact the economy of scale that makes silicon so successful; the ability to integrate millions of devices into a single circuit, combined with the ability to make hundreds of circuits on the same wafer. The number of components per chip doubles every 2 years: this formula is referred to as *the Moor's Law.*

There is, however, a major concern, that we are coming to the end of this exponential growth of capacity and decrease of dimensions [1]. The size of semiconductor devices has already approached the theoretical resolution limit of the lithographic process. Structuring thin layers on a sub-100nm scale requires switching to deep UV lithography, which is accompanied by enormous technical difficulties. On the other hand, quantum effects (coupling, doping fluctuations, tunnelling currents,...) will start to appear, which will obviously change the properties of the device. Yet, the main problem is due to interconnects. With the present density of semiconductor devices on a chip, several layers of structured metal are required for contacting. The heat generated in smaller devices and in thinner interconnects needs to be drained effectively, which

becomes more difficult for more densely packed elements. Therefore, Moor's law will no longer be sustained if no qualitative, physically new solution is found. We have, probably, come to the critical moment of the next revolutionary break-through in electronic technology. The front-line prospective solution presently under consideration is optical interconnects.

1.2 Optical Interconnects and Integrated Optoelectronics

The serial nature of conventional circuit architectures results in long interconnection lines on the chips, with most of the devices being idle at any one point in time. In combination to the continuous downscaling of integrated circuits (IC), this has resulted in electrical interconnects representing a formidable bottleneck to further performance increase and miniaturisation. In fact, the performance of some advanced circuits is already limited by interconnects and not by device speed.

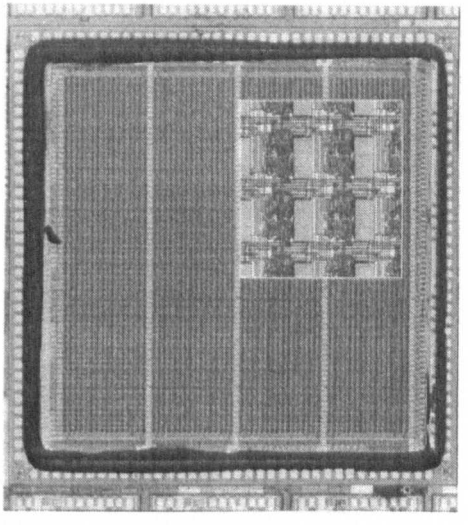

Figure 1. Optoelectronic Si multiple quantum well switching chip. Insert shows details of modulators. 4096-element light modulator-array is bonded to Complementary-Metal-Oxide-Semiconductor circuitry. GaAs/GaAlAs devices sense and reflectively modulate 850nm light (see reference in text).

The monolithic or hybrid integration of opto-electronic interconnects in microelectronic circuits aimed at the development of new architecture and packaging is the subject of intense research now and will be for the near future. 3D integration of light sources, detectors, electro-optic modulators and holographic surfaces or other optical components in a chip, including re-configurable (re-programmable) interconnects and the use of optics in neural chips are the further possibilities towards a long-term solution. Thus, the increasing complexity and speed requirements of next generation ICs and multi-chip modules can be fulfilled. As the first step, fast interconnects over distances of a few centimetres can be made available which fit into the chip architecture. Data rates per channel of the order of 1 Gbit/s are required. By using massively parallel connections, overall rates in the terabit per second range should be made available.

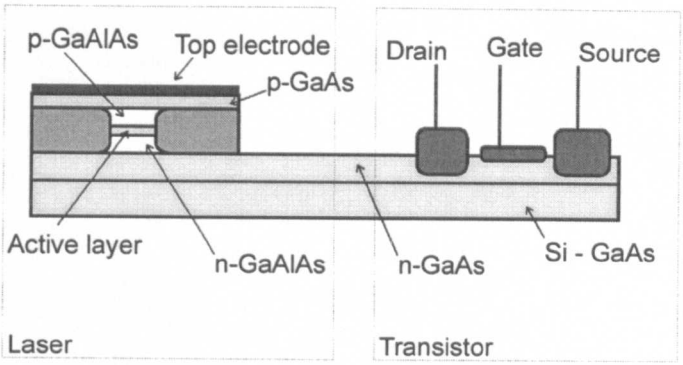

Figure 2. Conceptual scheme of GaAs field-effect transistor integrated monolithically with a buried heterostructure GaAs/GaAlAs laser (emission direction is perpendicular to the picture). The application of a gate voltage is used to control the bias current of the laser. The voltage can modulate the light at frequencies up to 10 GHz.

Another interesting possibility is Integrated Optoelectronics, where optical signals are transmitted and processed between the thousands of devices on one chip. Potentially this may give higher rates, lower power dissipation, and increased density of the devices. In Fig.1 the example of an optoelectronic switching chip is shown [2]. Fig.2 shows a scheme of monolithic integration of field effect transistor and heterostructure laser [3]. Such integrated elements interconnected by optical waveguides together with metal contacts would make a new generation of microprocessors possible. 3D architecture of processors with interchip optical communication through free space is also being considered.

The waveguiding of optical signals in microchips does not seem to be a problem. GaAs planar waveguides (Fig.3) are widely used today. Porous silicon studies could enable the use of Si as a guiding material in the future, due to the possibility of varying the refractive index of the material in a wide range (1.3-3.0) [4]. Different ways of modulating or switching the optical channels have been developed. Fig.4 demonstrates one of the techniques [5]. A similar switching of optical signal in semiconductor waveguides with the same arrangement is possible if a p-n junction is formed within the waveguide: applied electric field changes the free carrier concentration which results in the local variation of refractive index.

Semiconductor photodetectors can be successfully used for transformation of optical to electrical signals. These include p-n and p-i-n diodes, avalanche Schottky-Barrier and Metal-Semiconductor-Metal (MSM) detectors. New SiGe detectors have

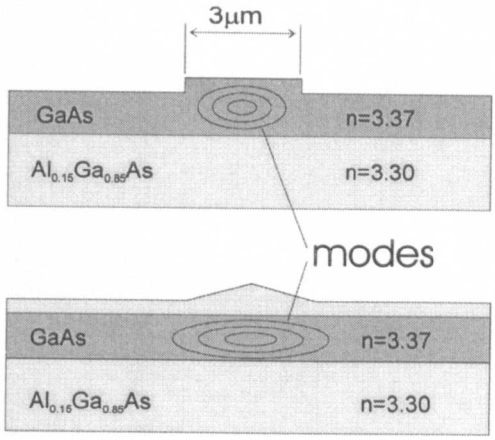

Figure 3. Typical cross-sections of a planar optical waveguide. The mode is confined in a thin layer with higher refractive index. Confinement in the perpendicular direction is achieved either by the structuring of the thickness of the guiding layer (top) or by structuring of the additional upper passive layer (bottom). The first case gives better confinement, allowing single mode operation.

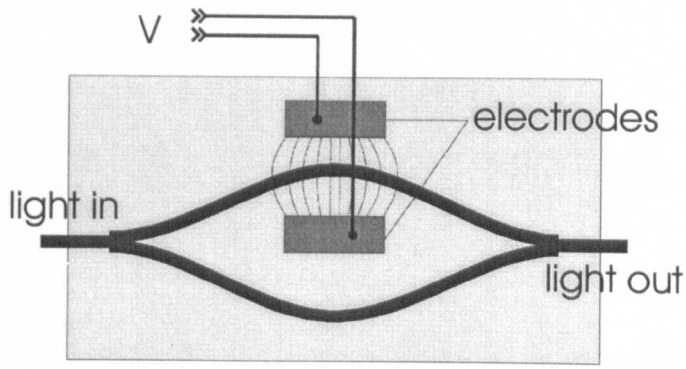

Figure 4. Conceptual drawing of a modulator, fabricated in thin film technology on Si. Electro-optic effect in BaTiO3 is used for phaze modulation of one of the two passes to switch between constructive and destructive interference on the output.

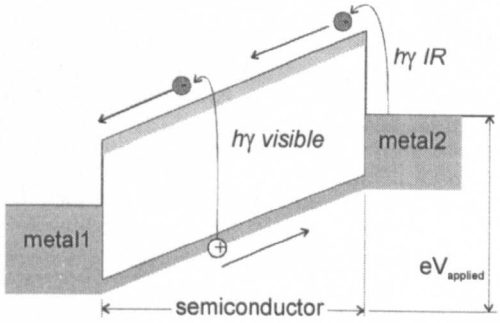

Figure 5. Schematic operation of a MSM diode, for n-type Si. Incoming light from the waveguide creates carriers in a silicon layer between two metal electrodes.

attracted research attention recently. The operation of a typical MSM detector is shown schematically in Fig.5. A pulse response time of 3.5ns has been reported for such a Si-based device [6].

The most difficult objective for Si-based integrated optics is, obviously, the design of light emitters. The process of growth or integration of LEDs on silicon wafers should be low cost and compatible with the highly developed microchip technology, while the devices should be fast, stable and energy-efficient. This presents a great challenge for current scientific research.

1.3 Discovery of luminescent porous silicon

Porous silicon was first observed in 1956 when attempts were made to electro-chemically polish silicon wafers for the then emerging electronics industry [7]. Polishing techniques using hydrofluoric acid based etch solutions were applied and it was noticed that under certain conditions the wafer was covered with a reddish/brown deposit.

In the fall of 1990, Leigh Canham of the UK's Defence Research Agency reported that one could obtain visible room-temperature photoluminescence from porous silicon layers, formed on silicon surfaces by electro-chemical etching [8].

The light-emitting properties that Canham reported for porous silicon were intriguing for several reasons. First, the emission energy was well above the bandgap of bulk silicon. Second, the energy (or the color) could be tuned throughout the visible spectrum by changing the preparation conditions, which is important for display technologies that require red, green and blue devices. Finally, the quantum efficiency was comparable to that of direct-bandgap semiconductors.

Canham's paper generated worldwide speculation that a silicon-based optoelectronic technology was at hand, and it kicked off a flurry of research activity directed at porous silicon. Steady progress has been made in uncovering the fundamental properties of the mechanism of luminescence. Porous silicon's suitability for optoelectronic applications has also been an active area of research, and room-temperature LEDs with efficiencies greater than 0.1% as well as test structures that integrate LEDs with electronic devices have been fabricated [9].

The graph in Fig.6 demonstrates the rapid growth of scientific interest in porous silicon in the last decade of the century, following Canham's report in 1990. Solid squares show the number of search results for "porous+silicon", left axis. The results for "luminescence+porous+silicon" are shown in empty squares, right axis. The second graph obviously does not include all the papers on the subject, as "luminescence" is not always present in the title - for example, the original Canham paper is not included. The popularity of the subject appears to be in decline now, but a new field of interest is arousing, namely "nano-crystalline+silicon", shown in circles. Naturally, the potentiality of the research in this new area would not be realised so widely without a decade of research on the origin and properties of luminescence from porous sili-

con. It should be mentioned here, that porous silicon still is to be considered as the main competitor for silicon-based light-emission (see Table 1), and that applications of porous silicon other than for optical devices are also being developed, including gas sensors [10], thermoisolation materials, and materials for prothesis or cell-to-electrode interfaces in bio-medicine [11].

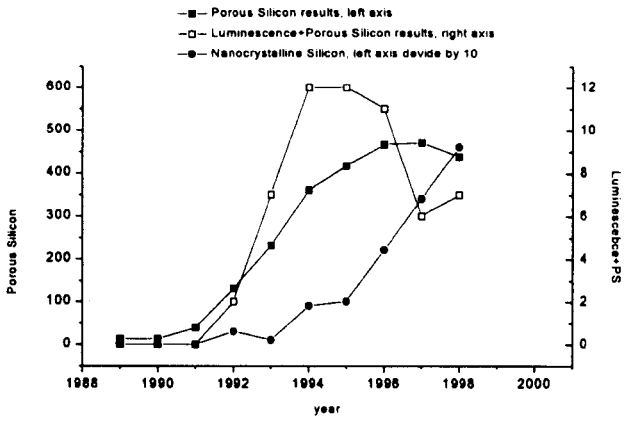

Figure 6. Search results from BIDS service showing the explosive growth of the interest to porous silicon. Only a small fraction of papers on luminescent property of Porous Silicon is included in the second graph, as the search was limited to those containing "luminescence" in the title. The third graph (circles) shows a rapid interest developing in nano-crystalline silicon studies during a very recent time.

Group approach	Material systems	Positive features	Difficulties	Hopes
Indirect gap Si and alloys	Si, SiGe	Manufacturability	Low emission rates	Micro-Quantum-Well effects
Direct gap alloys	GeSn, SiGeC	Manufacturability	Underdeveloped	
RareEarth doped Si	Er-doped Si	Best wavelength fot fiber optics	Temperature dependance of efficiency	Other hosts, codoping
Nanocrystaline Si	PS, NS, Si clusters in alloys	Native Si material, well developed processing technology	Low quantum efficiency, slow internal modulation (PS), instability, manufacturing	Size distribution narrowing, better passivation

Table 1. Material systems for Si-based light emitters

1.4 Light emitting material systems for Integrated Optics

At present, III-V direct band-gap semiconductor components are used for optical purposes in microelectronic devices. The integration of these discrete elements to silicon wafers is a costly and technologically complex process. On the other hand, silicon is the basis of the modern microelectronics. A huge amount of technology based on silicon has been developed. The material is mechanically reliable and reasonably cheap. The processes involved in technological lines are well understood. Therefore it is most likely that silicon will continue to dominate in electronics of the future. This makes the quest for silicon light emission well justified.

If fast, efficient and low cost silicon-based light emission could be achieved, this would represent a major revolution in microelectronics, because light emitters, waveguides and detectors could be produced by silicon processing alone.

Silicon based light emitters are compatible with the present Integrated Circuit technology. However, all fabrication technologies which are currently under investigation require additional wafer process. Furthermore, the optical output power, quantum efficiency, bandwidth and the degradation in some types of silicon-based emitters are critical issues, which may prevent the use of these devices. In Table 1, the main approaches for silicon-based light emission are compared in terms of their positive and negative features [1].

The major competitors are Er-implanted silicon, Group IV alloys (with or without quantum-well structures) and nanocrystalline silicon. Presently, all of these are in

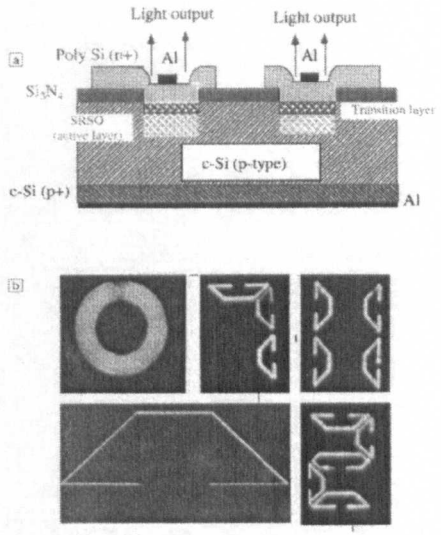

Figure 7. LEDs based on oxidized highly porous silicon (marked SRSO) as an active layer. Schematic structure of the device (transition layer is made of low-porosity Si) (top) and examples of microdisplays produced (bottom).

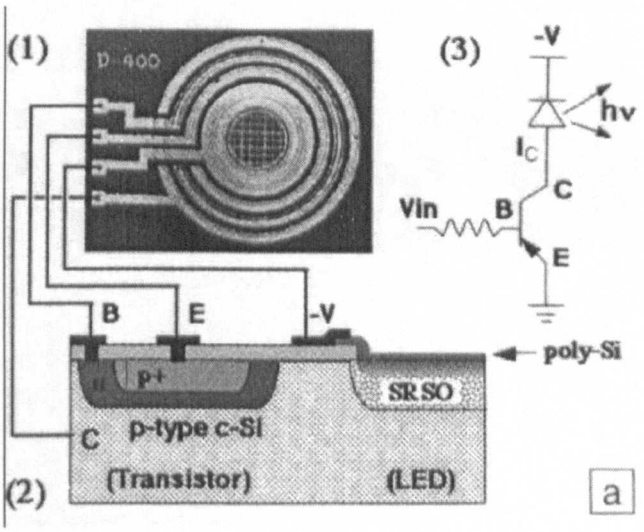

Figure 8. An integrated circuit containing PS-based LED and bipolar junction transistor. Structure scheme (1,2) and an equivalent circuit (3).

research stage. Each has unique drawbacks. Erbium-implanted silicon, for example, has limitations in terms of working temperature, Auger nonradiative deexcitation and the dissolution limit of Er in Si, [12] although, recent reports show considerable improvements of the characteristics of the material [13]. Materials produced with CVD (Si in SiO_2 or in SiN_x, SiGe dots and super-layers) have structural defects which are difficult to control. The problems with porous silicon are the preparation procedure, stability, spectral width and frequency characteristics, although working devices have already been demonstrated both IC-integrated (Figures 7, 8) [9], and emitter-waveguide-detector integrated [14]. Joint approach of Er-doped films deposited onto porous silicon have also been studied [15]. However, forms of nanocrystalline silicon other than porous seem to be more promising today.

1.5 Nanocrystalline silicon as, probably, the best solution

Understanding the mechanism of luminescence in porous silicon has led to a rapid increase of interest in other ways to prepare nanocrystalline silicon. Fig.9 shows examples of different forms of nanocrystalline silicon. Having similar luminescent properties as porous silicon, if assembled synthetically, these are materials free from most of the problems associated with porous silicon. For example, the spectral width of the luminescence is expected to be reduced by size selection of nanoclusters. Frequency characteristics will also exceed those of porous silicon due to the absence of a fractal-like microstructure. Up to now, 10^{-4} sec radiative lifetime and quantum efficiency close to 50% at 20K have been reported for surface oxidized nanocrystals prepared by a high-temperature aerosol technique [16]. The alternative way of producing silicon nanocrystals is by controlled thermal recrystallisation of amorphous Si/SiO_2. Nanocrystalline layers thus produced can even be built up into multilayers, an example is shown in Figure 10 taken from [17].

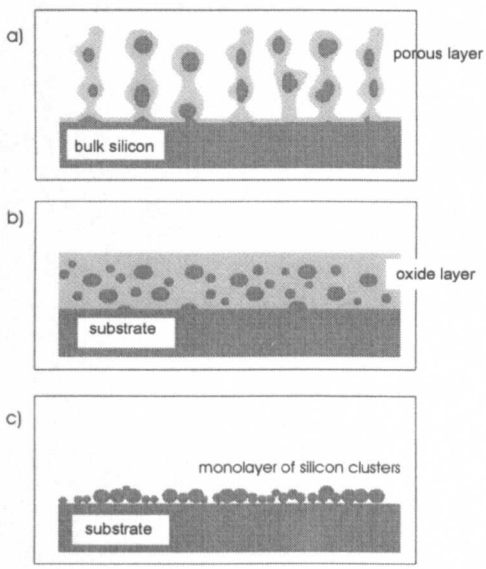

Figure 9. Different forms of nanocrystalline silicon: highly oxidised porous silicon (a), implanted silicon in silicon oxide or another matrix (b), deposited synthesized silicon nanoclusters (c).

Along with continuous improvement of the luminescent properties of nanocrystalline material, research all over the world is focused on methods for injecting carriers into nanocrystals. Finally, geometrical structure of the device and technological dif-

ficulties of incorporation of active nanocrystalline Si media with optical elements are subject of discussion.

The study of luminescence from porous silicon, however, has not ended, because firstly, synthesized nanocrystalline films are yet far behind in terms of power efficiency at room temperature, and secondly, the mechanisms involved in the visible luminescence of porous silicon and of nanocrystalline silicon are not completely clear yet. These subjects and the related technological and scientific problems are addressed in this thesis.

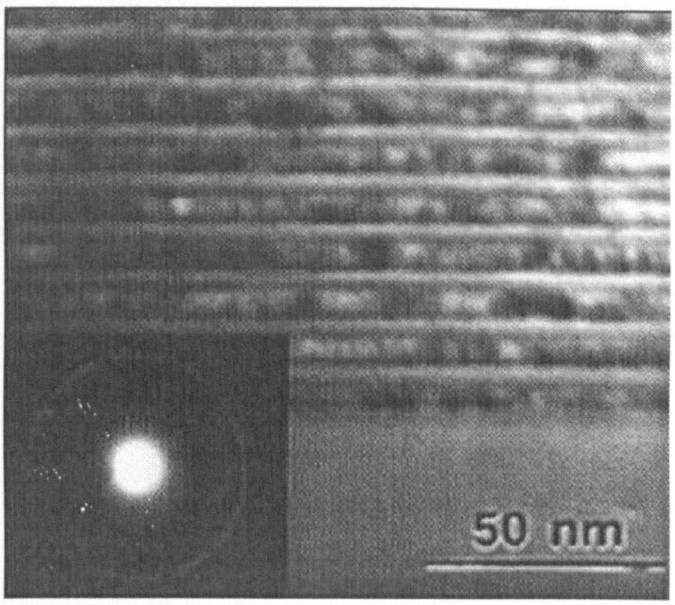

Figure 10. An example of the Si/SiO_2 superlattice. The inset shows electron-diffraction pattern indicating a crystalline structure but with random orientation of nanocrystals.

Chapter 2
Review (relevant physical background and up-to-date research results)

"As we get into marvelous phenomenon of real nature - instead of the idealised spheres of perfect conductors inside of other spheres that we can solve so neatly - we discover that we don't know very much"

R. Feynman

In this chapter:

- Relevant basic physics (pp. 26 - 33, 52 - 59)
- Up-to-date achievements luminescent silicon research (pp. 34 - 51)
- Theoretical concepts for Quantum Dots (subset from [18]) (63 - 72)
- Review of recently reported analytical and computational results for silicon nanostructures (72 - 77)

2.1 Basics of semiconductor physics

Here are some of the basic concepts of a semiconductor physics, which will be used in the following chapters. In most cases the simplest 1D case is discussed.

2.1.1 Electrons in semiconductors

Electrons in crystals (Periodic potential). Electron states in crystals can be described by the wave-function

$$\phi(x) = u_k(x)\, e^{ikx} \tag{2.1}$$

where $u_k(x)$ is periodic over the lattice (see Appendix A).

The associated energy E_k should belong to one of the allowed energy intervals called energy bands. Other energies fall in forbidden gaps, where no propagating electron wave is possible.

The dispersion relation $E_k = E(k)$ depends on the periodic crystal potential and defines the electronic band structure of a crystal. Collective interval of k values, such as

$$\frac{m\pi}{d} < |k| < \frac{(m+1)\pi}{d} \tag{2.2}$$

for each integer m, where d is a crystal period, is called a *Brillouin zone*, the first zone being the interval $|k| < \pi/d$.

Zone population. The uppermost occupied Brillouin zone is called the *valence band*. The next band up in energy is called the *conduction band*.

Due to different possible spins, each Brillouin zone can accommodate a number of electrons which is twice the number of unit cells in a crystal. That is why crystals with even number of electrons per unit cell are insulators: the valence band is completely full and the conduction band is empty, no electric current is possible. For semiconductors, however, the valence-to-conduction band separation is comparable with the thermal activation energy of electrons, this causes some non-zero occupation of the conduction band, according to the *Fermi-Dirac distribution law* [19], where the parameter E_F is known as the *Fermi energy*:

$$f(E) = \frac{1}{e^{\frac{E-E_F}{k_B T}} + 1} \tag{2.3}$$

This means, that at non-zero temperatures there is always some electron population of the conduction band, and some population of free electron states in the valence band. The schematic band diagram of a direct-gap semiconductor at non-zero temperature is shown in Fig 11. Here some of the electrons from the top of the valence band are thermally excited to the bottom of the conduction band. Only the low energy states in the conduction band (those with minimum $|k|$) are occupied. The empty states in the valence band are called holes and can be considered as positively charged particles in a periodic potential.

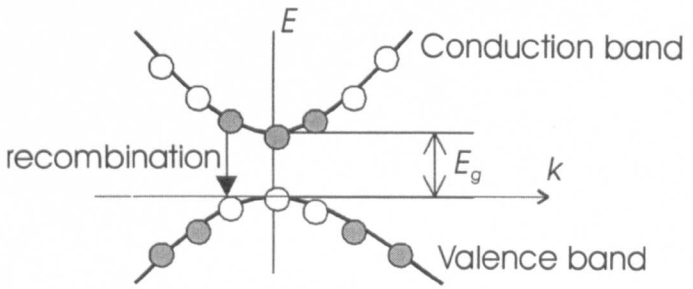

Figure 11. The schematic band diagram of a direct-gap semiconductor at non-zero temperature.

Point-like electron (Group velocity). The classical motion of a point-like electron in the lattice may be characterised by the wave packet of the form [19]

$$\Psi(x,t) = \sum_k a_k u_k(x)\, e^{i(kx - Et/\hbar)} \tag{2.4}$$

with amplitudes a_k having a Gaussian distribution in the vicinity of a central value $k^{\max}$. By substituting a linear approximation $E(k^{\max} + \Delta k) = E^{\max} + (dE/dk)\,\Delta k$ it can be shown that the wavepacket (2.4) propagates with the so-called *group velocity*:

$$v_{gr} = \frac{1}{\hbar}\frac{dE}{dk} \tag{2.5}$$

Dispersion relation (Effective mass). The relation $E(k)$ in the vicinity of a band edge can often be approximated as

$$E(k) = E(k_0) + \frac{\hbar^2 (k - k_0)^2}{2m_{e,h}} \tag{2.6}$$

where k_0 corresponds to the band minimum (or maximum), and $m_{e,h}$ is the effective mass of the electron or hole and may be positive or negative depending on the cur-

vature of the band. In a general case the effective mass is found from the following consideration.

Under the influence of an external force, the change of electron energy is equal to the work done on electron:

$$\Delta E = \frac{dE}{dk}\Delta k = \langle force \rangle \, v_{gr} \Delta t$$

By using (2.5) we obtain $d(\hbar k)/dt = \langle force \rangle$, and using it to take a time derivative of (2.5), we find

$$\frac{dv_{gr}}{dt} = \langle force \rangle \left(\frac{1}{\hbar^2} \frac{d^2E}{dk^2} \right)$$

which means that electron motion can be described by the Newton's law

$$\frac{d^2x}{dt^2} = \frac{\langle force \rangle}{m}$$

with an effective mass given by:

$$m = \left(\frac{1}{\hbar^2} \frac{d^2E}{dk^2} \right)^{-1} \tag{2.7}$$

The effective mass of the hole is the negative of its associated electron (the electron in the same band with the same k-value).

Interband transitions. Electron can return from the conduction to the valence band, provided the electron state in the valence band with the same k-value is empty. This process may be considered as a recombination of the electron and a hole. The requirement for k-conservation may be understood in terms of momentum conservation (if we disregard the momentum of the emitted light quanta in comparison with momenta of electron and hole), or quantum-mechanically, in terms of non-zero overlapping of electron and hole wave-functions (For $k_e \neq k_h$ the integral of the product of the spatial parts of the wave-functions over the whole crystal vanishes).

The energy liberated in such a recombination process can be expressed as:

$$\hbar\omega = E_e - E_h = E_g + \frac{\hbar^2 k^2}{2m_e} + \frac{\hbar^2 k^2}{2m_h} \tag{2.8}$$

where m_e and m_h are the effective masses at the electron and hole respectively. The liberated energy $\hbar\omega$ is emitted in the form of a unit of *electromagnetic radiation* (light).

Band-to band optical transitions in semiconductors. The probability rate for an interband optical transition of the electron in a crystal from state a to b is given by the so called "*Fermi's Golden Rule*" from time-dependant perturbation theory (see, for

example, [19]):

$$W_{ab} = \frac{2\pi}{\hbar} |H'_{ab}|^2 \delta (E_b - E_a - \hbar\omega) \tag{2.9}$$

For perturbation matrix element H'_{ab} between the electron states with wave-numbers $\mathbf{k}_a$ and $\mathbf{k}_b$ to be non-zero, the condition $\mathbf{k}_a - \mathbf{k}_b = \mathbf{k}_{photon}$ should be satisfied, where the photon momentum $\mathbf{k}_{photon}$ can be disregarded, so that $\mathbf{k}_a \cong \mathbf{k}_b$. The $\delta (E_b - E_a - \hbar\omega)$ part of the equation (2.9) corresponds to the energy conservation requirement, and can be replaced with $\delta \left(\frac{\hbar^2 k^2}{2m_r} + E_g - \hbar\omega \right)$, where $m_r = m_c m_v / (m_c + m_v)$ is the reduced effective mass. The total number N of transitions per second is given by multiplying (2.9) by $\rho (k)$, the number of states per unit k, and integrating over all values of k. Finally (details in [19]) it is found that $N \sim (\hbar\omega - E_g)^{1/2}$. Consequently, the same dependance is obeyed by the absorption coefficient:

$$\alpha (\omega) = C (\hbar\omega - E_g)^{1/2} \tag{2.10}$$

where C is a numeric coefficient which can be obtained from the absorption data.

2.1.2 Doping and junctions

Intrinsic and doped semiconductors. *In intrinsic* (undoped) semiconductors all the carriers are created by excitation of electrons from the valence to the conduction band, so that the concentrations of conduction band electrons and valence band holes are the same ($N_e = N_h = N_i$, where N_i is referred to as *intrinsic carrier concentration*). The conductivity of undoped semiconductors is low and depends exponentially on the temperature, according to (2.3).

The necessary electronic properties of semiconductors are achieved by *doping* - the incorporation in the crystal lattice of other atoms, with 5 or 3 valence electrons, referred to as donors or acceptors respectively. This produces access concentrations of electrons or holes. The energy difference between the donor's extra electron state and the bottom of the conduction band is comparable with the thermal energy of the carriers, thus the number N_e of electrons added to conduction band nearly equals N_D - the concentration of donors. Similarly, $N_h \lesssim N_A$ for acceptor doping. These are called the majority carriers and the semiconductor is said to be n-doped or p-doped respectively. The concentration of minority carriers is sufficiently reduced, keeping the product $N_e N_h$ dependent only on temperature.

The last statement may be understood from the positions of statistical mechanics. The probability of electron-hole pair generation by thermal energy fluctuation is proportional to $\exp(-E_g/k_BT)$, and does not depend on doping. The rate of recombination, on the other hand, is proportional to the product N_eN_h, and should equal the generation rate if the semiconductor is in equilibrium. Thus we have for the concentrations N_e and N_h.of a doped semiconductor

$$N_eN_h = N_i^2 = const \times \exp(-E_g/k_BT) \tag{2.11}$$

where the *const* has only a weak temperature dependence.

PN-junction. When n-doped and p-doped volumes of the same semiconductor are brought into contact, the flow of electrons from the n-side to the p-side exceeds that from the p-type to the n-type due to the difference in concentrations, which means a resultant non-zero electric current through the interface. As a result of this, the n-side gets a positive charge and the p-part gets charged negatively. This flow continues until a potential difference is built up across the interface sufficient to force the total flow to zero. The equilibrium carrier concentrations and the electrostatic potential distribution across the interface are as in Figure 12.

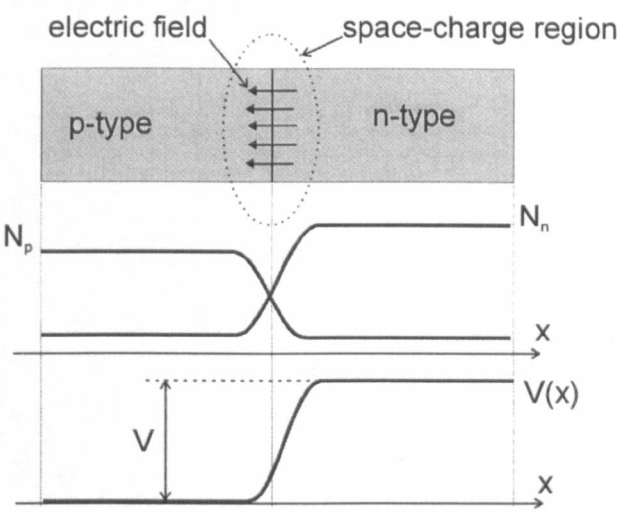

Figure 12. Equilibrium electric potential and carrier consentrations across the pn-junction (no bias).

The height of the potential V can be figured out from a general principle of statistical mechanics for equilibrium populations of two states with different energies. The

ratios of, for example, hole concentrations $N_h(p)$ in the p-part and $N_h(n)$ in the n-part should obey:

$$\frac{N_h(p)}{N_h(n)} = \exp\left(-\frac{W_h(p) - W_h(n)}{k_B T}\right) = \exp\left(+\frac{eV}{k_B T}\right) \tag{2.12}$$

The same equation is valid for concentrations N_e of electrons in agreement with (2.11).

The relationship (2.12) can be understood in a different way. The current I_{h0} of holes in n-side toward the junction is proportional to $N_h(n)$. All the holes will cross to the p-side, because of the favourable slope of the junction potential $V(x)$. On the other hand, the current of holes approaching from p-side $I_h(p \to n)$ is proportional to $N_h(p)$, but only the fraction $\exp\left(-\frac{eV}{k_B T}\right)$ of the total number of holes will cross to the n-side, again, according to statistical mechanics. This gives

$$\frac{I_h(p \to n)}{I_h(n \to p)} \equiv \frac{I_h(p \to n)}{I_{h0}} = \frac{N_h(p)\exp\left(-\frac{eV}{k_B T}\right)}{N_h(n)} \tag{2.13}$$

which coincides with (2.12) if currents are equalised: $I_h(n \to p) = I_h(p \to n)$.

Now, if an external potential ΔV is applied to the poles of the junction (the positive sign of ΔV corresponds to the positive terminal of the applied voltage on p-side), this will change the potential drop V across the junction[1]. The current $I_h(p \to n)$ of holes across the junction from the p-side will now have $V - \Delta V$ in the exponent of (2.13), which means the following dependence for this current with the applied voltage ΔV:

$$I_h(p \to n) = I_{h0}\exp\left(\frac{e\Delta V}{k_B T}\right)$$

The opposite current $I_h(n \to p)$ of holes from the n-side is limited by $N_h(n)$ and is independent of the voltage drop $V + \Delta V$ according to this simplified approach. Thus, it will not change with ΔV. For the total hole current we have:

$$I_h = I_h(p \to n) - I_h(n \to p) = I_{h0}\left[\exp\left(\frac{e\Delta V}{k_B T}\right) - 1\right] \tag{2.14}$$

Same consideration is valid for electron current I_e, hence, the total current I is given by (2.14) without h-index. The dependence $I(\Delta V)$ is shown in Figure 13. The current increases exponentially with $\Delta V > 0$, the regime is referred to as the *forward bias*. For the negative ΔV (*reverse bias*), the current saturates at some value $-I_0$.

This way of understanding the processes in pn-junction is simplified, although sufficient for the purposes of this thesis. The more detailed treatment should include

[1] The thickness of the junction region (where $dV/dx \neq 0$) will change accordingly, the relationship is studied in the next subsection.

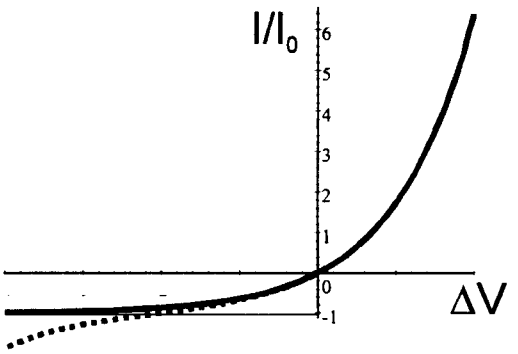

Figure 13. Exponential $I-V$ characteristic of pn-junction. Dotted line shows the dependence under the reverse bias, when the *generation current* is included.

the full transport equations for carriers in the vicinity of the junction region. This is done in, for example, [20]. One of the results of the full treatment is, for example, that the current under reverse bias does not saturate if the processes of electron-hole pair generation inside the junction region are taken into account. Once generated, the pair is not likely to recombine, as electron and hole are "pulled away" by the electric field dV/dx, thus each generated pair contributes to the current. The generation rate depends not just on illumination and temperature, but also on the thickness of the junction region, which, in turn, depends on the applied voltage. The corresponding slope of the reversed part of $I\ (\Delta V)$ is shown in Figure 13 with a dotted line.

Schottky barrier. When a semiconductor is brought into contact with the metal, the space-charge region with $dV/dx \neq 0$ arises similarly to pn-junction, but all the potential barrier is developed on the semiconductor side of an interface. The corresponding bending of the energy bands in semiconductor near the interface is known as *Schottky barrier* [21].

To evaluate the thickness of such a barrier, Gauss Theorem can be applied to the volume designated in the Figure 14:

$$S \times E\left(x\right) = \frac{1}{\varepsilon\varepsilon_0}\int_V q \cdot dv = \frac{eN_D S x}{\varepsilon\varepsilon_0}$$

where S is the cross-section of the integration volume, e is the electron charge, N_D is the doping concentration, and ε is the static dielectric constant in the depleted region. The potential distribution $U\left(x\right)$ is then obtained as

$$U\left(x\right) = U\left(0\right) - \int_0^x E\left(x\right) \cdot dx = U\left(0\right) - \frac{eN_D x^2}{2\varepsilon\varepsilon_0}$$

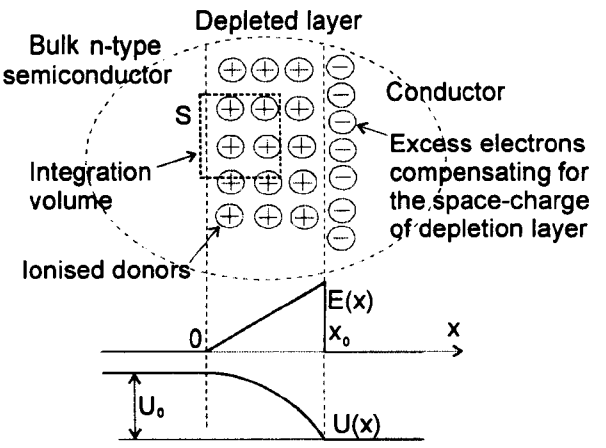

Figure 14. Depletion approximation scheme for calculation of the thickness of Shottky barrier. The layer fully depleted of majority carriers arises in semiconductor near the interace, with bare (ionised) donors forming a space-charge region.

The thickness of the depleted region associated with the total barrier height $U_0 = |U(x) - U(0)|$ can now be estimated as

$$x_0 = \sqrt{\frac{2U_0\varepsilon\varepsilon_0}{eN_D}} \tag{2.15}$$

The value for U_0 is usually taken from the difference of the electron work functions in the metal and semiconductor considered. Strictly speaking, the height of the barrier also depends on the energy difference between the conduction band and the Fermi level in semiconductor (the doping) and the density of the surface states. These effects are treated in details in [22].

2.2 Luminescent silicon

2.2.1 Proposed models for the Porous silicon Phenomenon

A major challenge has been posed for semiconductor physics in the last decade of our century by the discovery of the tunable visible luminescence from porous silicon. The first knowledge about the material was the nanoscale fractal-like morphology (from microscopy data) and the complex chemistry of the surface (from infrared spectroscopy data). Many models to explain photoluminescence have been proposed, and these are constantly being assessed and adjusted according to new experimental results. In the following only the green-to-red band, the so-called *slow band*, of the photoluminescence spectrum of porous silicon is discussed[2].

Since the discovery of efficient visible luminescence of anodised silicon [8], the overwhelming majority of researchers have agreed with the *Quantum Confinement Model* as the main mechanism of luminescence. However, a wide range of alternative hypotheses have also been put forward. All the proposed ideas can be grouped into four classes [25]:

1. those based on quantum confinement alone (crystalline silicon quantum wires and dots) [8], [26],
2. nanocrystal deep and shallow surface states [27], [28],
3. specific defects or molecules (SiH_x-complexes [29], [30], siloxane $Si_6O_3H_6$ derivatives [31], molecular Si clusters [32], carbon clusters [33], SiO_x defect states [34]),
4. structurally disordered phases (amorphous phases [4], vacancies in nanocrystals [35], relaxed surface [36], [37]).

Below follow the basic ideas of the most popular concepts.

---

[2] A carbonyl-related chromophore mechanism was proposed [23] for the *fast* blue emission, although nanostructure-based mechanisms have also been proposed [24].

Quantum Confinement Model. The band-gap up-shift in structures with reduced dimensions can easily be understood from the *Heisenberg uncertainty principle* point of view: if a particle is confined within δx interval in space, its momentum p_x is uncertain to within δp_x given by:

$$\delta x * \delta p_x \sim \hbar \tag{2.16}$$

Suppose an electron is confined within a nanocrystal of 1nm diameter. Then, using (2.16), $\delta p_x \sim \hbar/\delta x$, which causes the minimum kinetic energy up-shift $\delta E_x = (\delta p_x)^2 / 2m_e$ of the order of 0.1eV in our case (depending on the effective mass m_e). Confinement in other (y and z) directions adds similar contributions to the energy. The increase of the effective band-gap is roughly doubled, due to the similar confinement of holes. Thus, confinement energy components may bring the wavelength of the emitted (absorbed) photons into the visible region, even if the bulk material has a narrow bandgap corresponding to IR wavelength. Being more precise, the energies of confined particles are not just up-shifted, but quantised to a set of certain values. This effect is treated in detail in section 2.6.1.

As to the high efficiency of porous silicon luminescence, unusual for silicon as an indirect gap material, it is readily explained within the quantum confinement model as a result of exciton-to-optical field coupling being proportional to the strength of confinement (the inverse of the ratio between the confinement volume and the volume of the exciton in the bulk material).

Role of Surface States. A modification of the quantum confinement model was proposed by F. Koch. He suggested that absorption occurs into the quantised states of silicon nanoparticles, but after absorption the carriers relax into surface-related defect states with light emission occurring when carriers in the defect states recombine [38], [28]. To distinguish between the pure quantum confinement and this extended model a shift between the true bandgap and the emitted energy should be detected. It is difficult to perform this kind of study, because of the porous silicon intrinsic inhomogeneity: measurements of the bandgap are likely to look at a different group of nanoparticles from that involved in light emission. Some evidence for this energy difference has been reported as a result of optical absorption and photoelectron spectroscopy studies [39]. In [40] the experimental results for differently prepared silicon nanoparticle systems are analysed with the aim of interpreting all the facts within one model. Although the opti-

cal transitions between the confined electron states are not ruled out as the mechanism of luminescence, the important role of the perturbed Si layer on the surface (Si atoms bonded to O and H atoms) is stated.

Surface molecules. As a recent example of surface molecule-related mechanisms, works [41] and [42] can be considered. The papers start with the observation that in-situ photoluminescence appears in a very early stage of the etching, before the pores are formed. Detailed quantum chemical modeling of electronic transitions involving oxyhydride-like fluorophor is then described. The results are consistent with the known 550-700 nm broad spectrum of photoluminescence from porous silicon, the known time-dependence of luminescence at different wavelengths and the known infrared spectra of porous silicon.

2.2.2 Experimental studies of the mechanism of luminescence

It should be noted here that mostly results in favour of quantum confinement model are discussed below, because these are more relevant.

Correlation of sizes and spectra. According to basic quantum confinement estimations, 2-2.5 eV optical transitions result from crystallites with dimensions near 2-3nm. A first step toward testing the quantum confinement model would be to determine if crystallites of this size make up a large fraction of the silicon-based sample giving rise to this photoluminescence energy. Transmission electron microscopy and Raman scattering measurements have shown that the crystallites of these dimensions are present in porous silicon, examples in review [43]. An example of direct measurement of crystalline sizes followed by relating it to spectroscopic results can be found in [44]. However, these techniques do not allow a measurement of the sizes and spectra of the same nanocrystals. Additionally, the photoluminescence spectral features of porous silicon are very broad (200-300nm), which suggests a wide size distribution. A more convincing experiment was reported in [45]. In that study free standing silicon nanocrystals were chemically synthesised and than separated by means of liquid chromatography into groups with different average sizes. Spectroscopic study of these groups showed emission spectrum shifts to higher energies for lower average particle sizes, in perfect agreement with quantum confinement predictions.

Conventional structural studies were also used to relate the nanostructure sizes to the positions of the emission peaks. In [46] porous silicon samples emitting in red, yellow and green were produced by varying anodisation conditions. The samples were than studied with NEXAFS and EXAFS (x-ray absorption fine structure) techniques. Indirect confirmations of the size-to-wavelength correlation were obtained from: 1) the decreased influence of Si-Si bonds and the increased influence of Si-O bonds on the NEXAFS results for blue-shifted samples, suggesting the increased surface-to volume ratio, and 2) the decrease of the neighbor coordination numbers for blue-shifted samples, especially for 2nd and 3rd shells, suggesting the loss of medium-range order, possibly due to the reduction of nanocrystalline dimensions. Moreover, based on the modelling analysis, the conclusion was drawn that the nanostructures were of wire- rather than of dot-shape, which is also in agreement with the currently assumed mechanism of anodisation.

Raman Spectroscopy also can provide information on the sizes of nanocrystallites in porous silicon. This is discussed in section 3.4.

Momentum-conserving phonons. Further evidence in favour of the quantum confinement model is provided by the resonant excitation of the luminescent band [47]. Step-like features with energy separation from the excitation light corresponding quite closely to the energies of momentum-conserving phonons in crystalline silicon, clearly suggest that crystalline silicon is the luminescent material, even though the emitted energy is well above the bandgap of the bulk silicon. This is the major argument usually used to rule out surface-related emission mechanisms, see for example [48]. Another opinion is that the existence of phonon features in the resonantly excited photoluminescence only suggests that the absorption of photons occurs in indirect gap material [49]. The same authors, however, concluded in their later work [50], where selective hole burning with phonon-related energy offsets was detected, that luminescence of porous silicon arises from recombination between confined states.

The relative rate of non-phonon and phonon-assisted absorption-emission processes is also of interest. The spatial confinement of electrons and holes inside nanocrystals increases the uncertainty of their crystal momentum, thus allowing optical transitions in which phonons are not involved. This breakdown of the k-conservation rule in Si nanocrystals was studied in [51]. Non-phonon processes have been found to prevail

over phonon-assisted processes for emission energies over 1.9 eV, with a continuous increase of the ratio with energy. Assuming that the spectral intensity of the photoluminescent signal at a particular wavelength is defined by the density of silicon crystallites of a particular size, the result provides further evidence in favour of the quantum confinement model.

Luminescence lifetime measurements. Not only the increased bandgap but also the increase of optical efficiency must be explained. Insight into this effect has been obtained from luminescence lifetime measurements. These measurement involve the excitation of porous silicon with a short laser pulse, and then measurement of the light emission as a function of time after the pulse, to determine the rate of carrier recombination. The lifetime of photoluminescence in porous silicon depends strongly on the wavelength. For 1.7eV emission, for example, the lifetime is of the order of miliseconds, whereas for 3eV emission this changes to microseconds [52]. Using a thermal velocity of about $10^7 \text{cm} \cdot \text{s}^{-1}$ and assuming a 5nm nanoparticle size, classical estimation shows that a free carrier will hit the nanoparticle surface 10^9 times before recombining to give off light. Thus, another indirect confirmation for quantum confinement is provided: a carrier hits the surface more times per unit time in smaller nanocrystals, which decreases the lifetime.

Polarisation dependence. The polarisation dependence of porous silicon photoluminescence gives another indirect suggestion in favour of the quantum confinement model. The main observation is that the polarisation of the emitted light in photoluminescence experiments is preferentially the same as that of the excitation light [53], [54]. This is because the electron-hole pairs are preferentially generated in those nanocrystals which have their longer ellipsoid axis parallel to the electric field of the excitation light. In light emission, again the polarisation has a preferential direction corresponding to the longer ellipsoid axis of the emitting nanoparticle. This suggests that the geometry of the envelope wavefunction plays the crucial role both in absorption and in emission processes, rather than surface or amorphous defects or any molecular species, whose optical properties should be independent of the orientation. In addition, the information on the symmetry of excitonic states in silicon nanocrystals and on different heavy and light hole subband warping, was obtained from analysis of polarisation ratios along different crystal directions at different temperatures [55].

Polarisation studies also provide insight into the mechanism of anodisation. In works [56] and [57] the observation of polarisation memory effect is reported, where the preferential orientation of long ellipsoid axes of nanocrystals was defined not only by wafer orientation and by direction of electric current, but also by the polarisation of illumination during the etching[3].

The author's own study of polarisation effects in porous silicon photoluminescence is reported in section 3.5, where qualitative agreement with calculated results is shown and conclusions are drawn concerning the shape of the lowest excitonic wavefunctions in silicon nanowires.

The role of oxygen. Although the size-to-spectrum correlation was widely found to be consistent with a quantum confinement model, it has not been found possible to obtain continuous spectrum shift to blue for in-air photoluminescence by merely reducing the crystalline size[4]. This problem was addressed in [58], where a different mechanism for photoluminescence of oxygen-passivated silicon nanocrystals is suggested, involving surface-trapped electrons or excitons. While being not important for crystalline sizes larger than 3 nm (which corresponds to emission energies of up to 1.8 eV), the mechanism prevails for smaller nanocrystals (higher energies), limiting the peak photoluminescence values for oxidised porous silicon to below 2.2 eV.

2.2.3 Nano-crystalline silicon Techniques

The major synthetic (rather than anodisation) ways of producing silicon nanoclusters are listed below. Two groups of techniques may be distinguished depending on whether the resulting nanocrystals are prepared in a matrix (Figure 9, b) or in free space with the optional possibility of parallel matrix evaporation or later passivation (Figure 9, c).

Examples of the first group are:

1. PECVD (Plasma Enhanced Chemical Vapor Deposition): the PECVD process is based on the decomposition of a gaseous compound near the substrate surface,

[3] Mechanisms involved in preparation of porous silicon by anodisation process are discussed in section 3.2.

[4] "Continuous" in a sense that the main green-to-red band of luminescent spectrum shifts to blue, rather than the second defect-like blue band appears along with the main one.

similar to the related epitaxy and CVD (Chemical Vapor Deposition). One of the reaction products is a solid matter which precipitates onto the surface such that a new layer is formed. Silicon layers can be fabricated using the process gas silane (SiH_4) (see Figure 15). The advantage of the process is that it is fully compatible with the developed CMOS technology. Unfortunately, the photoluminescence efficiency of $\sim 0.04\%$ of such layers is still lower than that of porous silicon [59], [60].

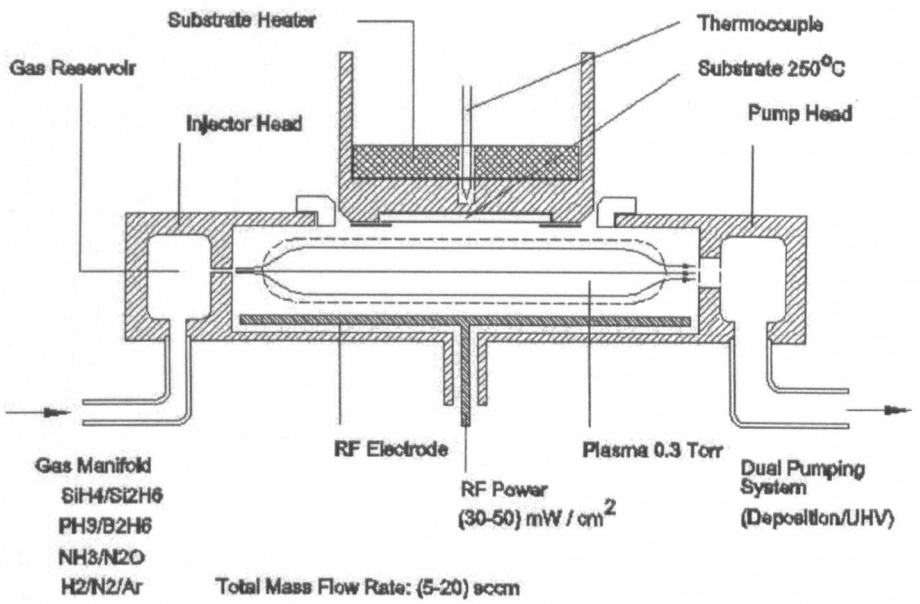

Figure 15. PECVD (Plasma Enhanced Chemical Vapor Deposition) scheme.

2. Ion Implantation: ions are accelerated up to a very high energy level, and then shot into the surface which is to be implanted. Typical depths of atom accumulation range between 100 and 300 nm. When a SiO_2 substrate is implanted with an extra dose of Si atoms, the latter diffuse together and form nanocrystals. This relaxation process may be intensified by heating (annealing). Annealing is also useful for removing structural defects in a freshly prepared layer. The size of Si nanocrystals may be controlled by the implantation dose, with a higher dose producing larger crystals. The visible photoluminescence of such layer was studied, for example, in [61] and [62], where good spectrum-to-size correlation was observed, in agreement with the quantum confinement concept. The role of surface-defect recombination based on the cluster-cluster interaction effect was suggested as responsible for

difference from basic quantum confinement predictions [63]. It is worth noting, that authors of an exciting report on the optical gain in silicon nanoclusters [64] were using ion implantation for preparation of their samples.

3. Co-sputtering. An example of luminescent silicon nanoclusters preparation by this technique can be found in [65]. A SiO_2 target on which were placed pieces of Si wafer was attacked by a low pressure RF-frequency Ar plasma. Si and O atoms were deposited onto Si wafer substrate, with subsequent annealing at 800^0C in N_2 atmosphere. EXAFS results demonstrated the formation of Si regions during the annealing process, and the accompanying appearance of blue photoluminescence, which was attributed to the presence of silicon nanocrystals observed in TEM.

Free-standing Si nanoclusters can be produced by:

1. Sputtering: similar to co-sputtering, but with a single target material and an inert gas plasma [65]. Only a low density of the sputtered material clusters is possible to avoid continuous layer formation.

2. Laser ablation: similar to sputtering, but intense laser pulses are used for hitting the target and local melting/vaporising the silicon, rather than RF-plasma [66]. In recent work [67] the target itself was used as a substrate. The trajectories of the ablated particles differ for different sizes, allowing spatial separation of areas covered with particles of different mean size. An interesting result reported in the last reference is that although the mean particle size was shown to be proportional to laser pulse power, it was impossible to continuously tune the position of the photoluminescence maximum by varying the power. This is, probably, the sign of two different luminescence mechanisms for red-green and blue-UV luminescence.

3. Coagulation in gas media. This is the most promising modern technique, where clusters are formed in collisions of gaseous (free) atoms of the material. An example of a cluster source of this kind is schematically shown in Figure 16 together with a magnetic separator for mass (size) selection and an atomic beam source for matrix deposition or passivation.[5] The machine can make materials

[5] The author thanks Derek Eastham from the Daresbury Laboratory for the kind permission to use his original drawing.

which consist of clusters of one type free or embedded in a matrix of another. Whilst it is only possible to make microscopic thin films, these are sufficient for use as electronic or optical materials or for magnetic sensors. The new cluster machine allows one to make composites with uniform particle sizes (down to 1nm) for a large selection of materials. A schematic diagram of a very small cluster, more like a "big molecule", is shown in Figure 17. The interest to thus created clusters has recently been boosted due to the study of new optical properties of semiconductor nanoclusters caused by quantum confinement. The technique presents the most direct way to test the quantum confinement model of visible luminescence from silicon nanocrystals, see [68] and [69] for example. It is also possible to equip the vacuum chamber with an Atomic Force Microscope[6] to view the freshly prepared clusters, an excellent example of such an image can be found in [70].

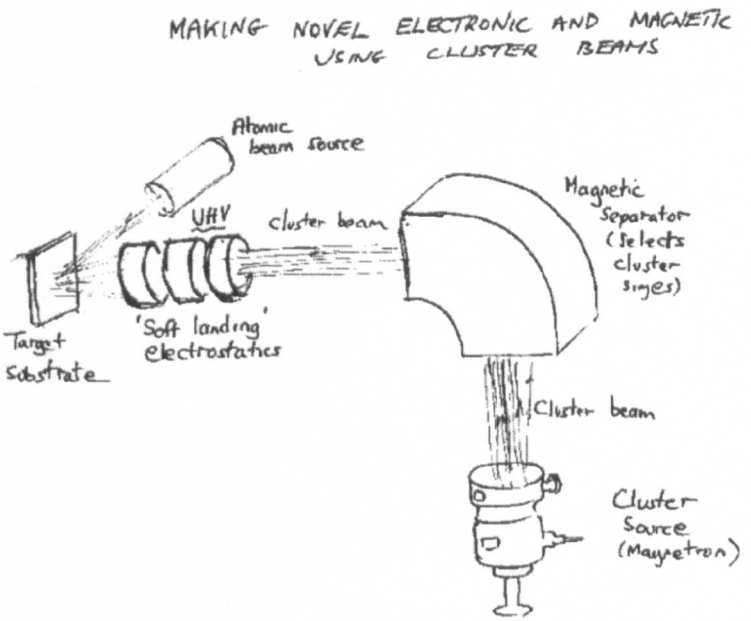

Figure 16. An original drawing by Derek Eastham of a cluster source built in Daresbury Laboratory.

4. Optical manipulation of atoms is another very new approach, where atoms are selectively deposited into certain sites, defined by the optical field. If the

[6] See page 81 for operation principles of AFM.

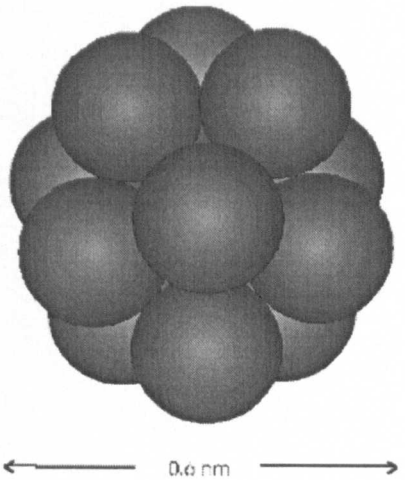

Figure 17. A small icosahedral cluster of atoms, each sphere represents a single atom.

resolution of the process would be brought down to several nanometers, controlled nanocluster formation would become possible. An example of such optically laterally controlled deposition was described in [71]. A detailed discussion of the technique and the results of computer modeling are presented in section 3.7.

2.3 Electroluminescence from Porous silicon

2.3.1 Physics of electroluminescence

As discussed above, visible light emission from porous silicon can be understood as a result of recombination of confined carriers. In the case of photoluminescence, the carriers are photo-generated by incoming photons with energies higher than the increased bandgap of the material. For real microelectronic applications, however, a way of generating free carriers electrically is required.

The first encouraging results on electroluminescence from porous silicon were obtained with liquid contacts [72]. High external quantum yield in the range of 0.1-1%, low applied voltages and voltage-induced spectral shifts, are the main attractive features of this type of contact. The advantage of the technique compared to solid contacts is that the liquid penetrates into the pores and makes a contact to the whole of the porous silicon film.

The efficiencies of electro-luminescence from porous silicon achieved with solid state contacts are much lower. The problem of the electrical conductivity of porous silicon arises, because, firstly, the electrons injected on one physical side should meet with holes injected on the other side for radiative recombination to occur. Secondly, the carriers are to be generated in or transported to nano-structures of that particular kind responsible for radiative recombination in the visible range, competing with recombination in other, namely larger structures.

2.3.2 Problems of contacting and conductivity of porous silicon

The usual way to measure the conductivity of porous silicon is via time-of-flight technique. Excess carriers are generated below the top electrode by a short (~0.3ns) strongly absorbed (UV) laser pulse. Depending on the direction of the external field either electrons or holes drift to the opposite electrode. The drift mobility of excess carriers is calculated as $\mu = L^2/t_{tr}U$, where t_{tr} is the carrier transit time through the thickness of the sample L, and U is the externally applied voltage. Results of such measurements for different sizes of structural elements are reported, for example in [73]. The experimental transient characteristics reveal a strong spatial dispersion of

the packet of drifting carriers, when the peak current moment t_{tr}^{max} can be used for calculation of mobility μ. It is concluded that the dispersion results from the movement of carriers throughout a network of paths different in geometry and electrical properties.

For low porosity samples (40-50%) the resistivity of porous silicon, even when prepared from degenerate Si substrates, is similar to that of intrinsic bulk silicon [74]. This has been explained by the high density of surface states in porous silicon, comparable to the dopant density [75]. This causes loss of carriers and also reduces the mobility of the majority carriers. The mobility edge is shifted up compared to the bulk silicon, due to the local electric field variations induced by the bound electrons in surface states.

For nanosized porous silicon the resistivity is very high, in the range of 10^{10}-10^{12} Ωcm. Quantum confinement results in the modulation of the effective bandgap. These fluctuations have a major impact on transport, because they increase scattering and cause localisation. The proposed mechanisms of conductivity in nanoporous silicon are hopping between the localised surface states at the Fermi level and thermal activation of electrons to the transport edge with hopping or tunnelling between tail states [76]. The Coulomb blockade effect was measured in nanoporous silicon samples, with porous film becoming insulating at low temperatures [77]. Large electric fields have to be applied in order to obtain measurable currents, and measurements are done in a sandwich configuration. The analysis of results is complicated due to the contact problem: it is difficult to know the depth of the electrode penetration into the porous layer, and the actual contact surface area.

The conductivity also has a super-linear behavior with applied voltage, which is explained either by the exponential increase of tunnelling probability for higher fields, or by the increased rate of thermal activation of carriers at higher temperatures [78]. The space charge model should be mentioned here, according to which for high voltage all the traps become filled. The Fermi-level is no longer fixed to the middle of the gap and shifts towards the band edge resulting in a decrease of activation energy. The mathematical problem of conductivity of two-component media is related to the subject being discussed. Results of computer simulation of such conductivity are presented in section 3.6.

High frequency conductivity is roughly proportional to the frequency, which suggests that hopping at the Fermi level is the main mechanism for carrier transport. For

lower frequencies, the fractal nature of the silicon network has been shown to impose geometrical constraints on the charge transport [79].

Oxidation is known to increase the resistivity of porous silicon, and this can be understood in terms of substituting insulating silicon-oxide for silicon at the surfaces of nanostructures. The study of the effect of oxidation on conductivity is reported in [80] and [81]. The effect was also studied in [82], where carrier diffusion effects on photoluminescence were measured and modelled, showing the dependence on oxide thickness and porosity.

One of the latest works on the subject of conductivity of porous silicon [83] determines the density of state distribution near the Fermi level in porous silicon from the analysis of the current-voltage and current-thickness characteristics of a planar structure in the space- charge-limited-current regime. The distribution is found to be U-shaped with a minimum at the Fermi level. Theoretical analyses are offered to explain both characteristics, which imply that the current is entirely controlled by localised states situated at the quasi-Fermi level.

To conclude, the problem of inhomogeneity of porous silicon should be stated. It is difficult to unambiguously relate the conductivity of the porous layer to its luminescent properties, because the current flow is likely to take place in structures that are, on average, larger than those emitting light. The energy gaps deduced from the photoluminescence excitation measurements are larger than those derived from the spectral response of the photoconductivity [84].

2.3.3 Existing porous silicon light-emitting devices

In porous silicon electroluminescent device electrons are to be injected into the porous layer with energies above the bottom of the conduction band, and holes into the valence band. Different approaches to this problem and different requirements for the colour and width of the spectrum lead to different structures for EL devices. The most impressive examples of porous or nanocrystalline silicon-based LEDs [9], [17] were discussed in the Introduction. To complete this subsection, other known reported devices are summarised in a table together with achieved parameters. Table 2 gives the definitions of performance parameters, and the requirements for microelectronic

Parameter (units)	Description	Display need	Optical interconnect need
External efficiency(%) or EQE	A power efficiency (emitted to injected) or quantum efficiency (photons per electron)	>1%	>10%
Brightness (Wcm^{-2})	The power density of output	10^{-3} Wcm^{-2} at 5-10V	0.1 Wcm^{-2} at 3.3V
Modulation speed: 3dB frequency(Hz), rise time(s), fall time(s)	Frequency at which the modulation depth of EL response to sine voltage wave falls by two. Rise and fall 1/e response times to a single square voltage pulse	>1 KHz rise<1ms fall<1ms	>GHz, rise<1ns fall<1ns
Peak (nm)	The wavelength of the peak of the emission band	Red, green and blue colors are needed	Compatible with detector and waveguide technologies
Spectral width(nm)	FWHM	~0.1eV	Limited by dispersion effects
EL threshold voltage (V)	The lowest voltage at which EL is observed using an adapted eye	5-10V	<3.3V, for integration with CMOS circuity
Stability(time)	A minimum time befor a significant degradation of the EL signal	$>10^5$ hours	$>10^5$ hours

Table 2. Parameters used to describe the performance of LED devises

applications of EL devices. Information on the reported EL devices (taken from: [25], [85], [86], [87], [88], [89], [90], [91]) is summarised in Table 3.

Structure of a device	Description	Typical parameters achieved
Single PS layer with a top contact	A layer of porous silicon made from n- or p-type, with gold or indium tin oxide top contact deposited	EL threshold voltage 1.35V, EQE 0.05%, emission in red, may be shifted to blue depending on the contact material and anodisation procedure. 100 nanosec response time was reported. The maximum reported lifetime is 100 hours.
Porosified p-n junction	P^+n^- or p^-n^+ junction is formed in a bulk silicon by implantation, by diffusion or by epitaxial growth. The region is then porosified.	EQE better than 0.1%. Threshold voltage 0.7V. Low stability - only a few hours rise and fall times ~10 μsec
PS layer impregnated with another material	Impregnation with metals or polymers by electrochemical process is used to produce a larger contact area. Impregnation with oxide improves stability.	The highest reported EQE was 0.05%. Shift of the peak from red to blue with operation time was explained by partial oxidation. Improved stability of a device was achieved with aluminium oxide impregnation.
Oxidised PS layer	Si-H bonds on PS surface are replaced with more stable Si-O bonds by anodic oxidation, chemical oxidation or by annealing.	Rise and fall times less then 0.1 μsec Alphanumeric displays and integration with pnp transistors have been demonstrated
PS layer contacted by bulk semiconductor	Structure is built either by selective anodisation or by deposition of amorphous semiconductor onto the PS layer	Higher stability, but lower EQE: <0.01% if selective anodisation of p-type beneath n-type layer was used. However, 0.13% efficiency was reported for devices with amorphous layers.
Micro- cavity PS	The layers of alternating porosity are produced by varying the electric current during anodisation.	The FWHM is sufficiently reduced
Stain-etched PS	Direct electrical contact to the layer to be porosified is not required, which is a technological advantage.	Reported thresholds: 1.5 - 3 V. Emission in red. EQEs are not reported

Table 3. Reported Porous Silicon LEDs

2.4 Porous silicon for passive optical elements

2.4.1 Porous silicon waveguides

To provide confinement and propagation of light within the waveguide, the guiding region has to have a higher refractive index than the surrounding regions. It is possible to fabricate porous silicon-based planar optical waveguides because the refractive index of porous silicon varies from 1.3 to 3.0 with the porosity [4]. In turn, the porosity of porous silicon depends on the anodisation regime and doping. In reference [92], fabrication was reported of a multilayer waveguide consisting of a 62% porosity waveguiding layer sandwiched between 75% porosity upper and lower layers. A strip waveguide was formed on as-prepared planar structure by lithography and reactive ion etching. Waveguiding was observed at $1.28\mu m$ wavelength with propagation losses 10-20 dBcm^{-1}. These high optical losses were then reduced by oxidation of porous silicon down to as low as 5 dBcm^{-1} for both IR and visible light [93], [94].

The main advantage of waveguides based on porous silicon lies in their potential for direct integration with the active region of LEDs and photodetectors to minimise coupling losses.

2.4.2 Porous silicon reflectors and microcavities

The dependence of the refractive index of porous silicon on the preparation conditions (usually on anodisation current) gives an opportunity to produce reflectors or interference filters from porous silicon, tunable to a desired wavelength. Figure 18 shows the structure of such devices together with a typical reflectance spectrum [95], [96], [97]. Bragg reflectors consist of multiple layers with alternating refractive indexes, the so-called quarter-wave layers. The thickness of layers is adjusted so that the reflections from the interfaces are in phase, thus increasing the reflectance for a chosen wavelength. For not-normal incidence, different wavelengths correspond to different angles α between the propagation direction inside the structure and the normal to the interfaces:

$$\lambda(\alpha) = 2dn\cos(\alpha)$$

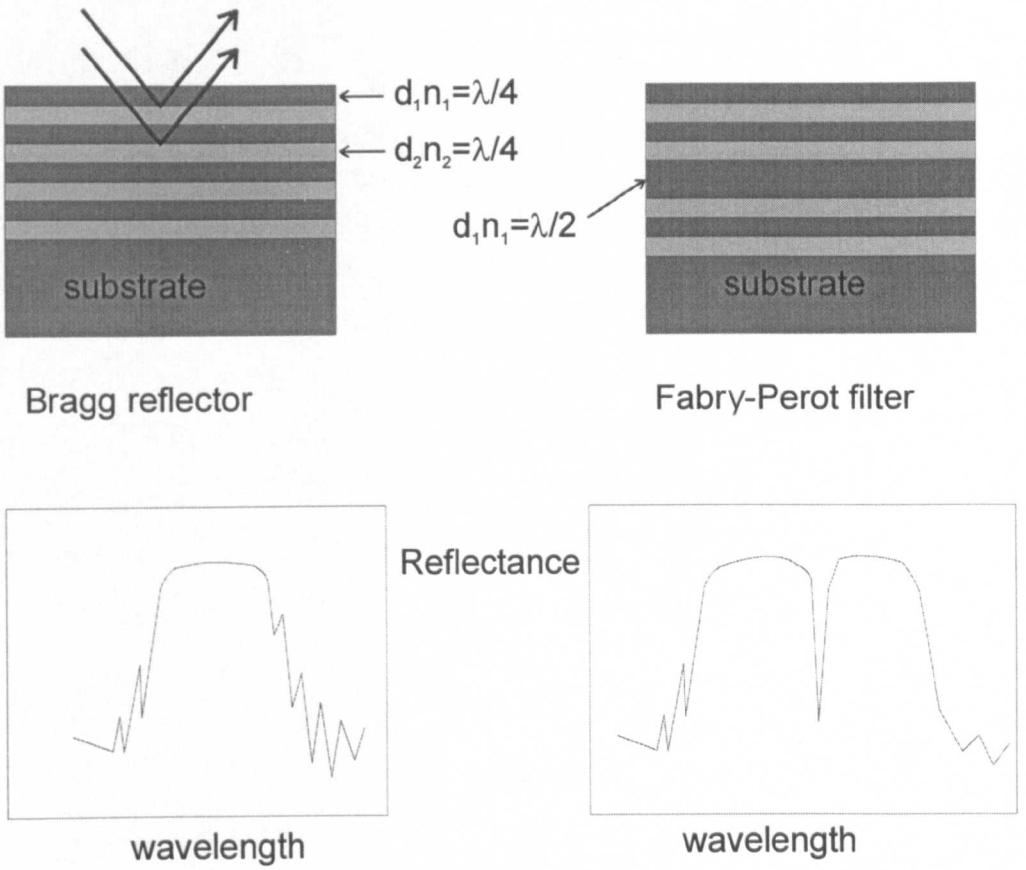

Figure 18. Schematic cross-section of interference filters prepared from porous silicon. Lower figures show the reflectance spectra of these filters.

The wavelength of the maximum reflection can thus be tuned by varying the angle of incidence. The change of colour of the reflected light is easily seen when a multilayered porous silicon sample is viewed at different angles. For filters thicker than 10 μm the anodisation current density has to be adjusted with depth because of diffusion problems during formation.

In case of Fabry-Perot filters, a half-wave layer is additionally incorporated into the multilayer structure. Fabry-Perot filters can also be advantageous for photoluminescence and electroluminescence in order to reduce the full width at half maximum and the decay times of the EL. A resonant cavity light emitting diode was reported in [98].

2.4.3 Photodetectors

These are not truly "passive elements", but should be mentioned here for the completeness of an overview of optical properties.

A very sensitive (with quantum efficiency of 0.97) photodetector based on a metal - porous silicon junction was reported in [99], with a Gaussian spectral response from 630 to 900 nm. The sensitivity of the device decreased only to about 70% of the initial value after 12 days of continuous operation. The stability was shown to improve after rapid thermal oxidation. Superlattices were successfully used to change the spectral response in a desired way and produce colour-sensitivity (the effect being similar to that of a reduced spectral widths of the resonant cavity based LED) [100].

2.5 Silicon laser?

2.5.1 Basic laser physics concepts

Induced and spontaneous transitions. Consider for simplicity a two-level atomic system in Figure 19, with the top energy level 2 and the bottom level 1.

When such a system is subject to electromagnetic radiation of the resonant frequency (shown as radiation quanta), transitions occur between the atomic energy levels with rate proportional to the intensity of the field. This rate is the same for both downward and upward transitions [19], and can be expressed as follows:

$$W_{12} = W_{21} = W_i = \frac{\lambda^3 g(\nu)}{8\pi h c n^2 t_{spont}} I_\nu \tag{2.17}$$

where $g(\nu)$ is the lineshape function of the transition and t_{spont} , known as the *spontaneous lifetime* of the upper state from quantum mechanics, and is inversely proportional to the square of the dipole matrix element of the transition.

The total rates of these induced (*stimulated*) upward and downward transitions are $N_1 W_i$ and $N_2 W_i$ respectively, where N_j denote numbers of atoms in each state. On the other hand, the average populations N_2 and $N_1$of the two energy levels obey Boltzmann's relation

$$\frac{N_2}{N_1} = e^{-(E_2 - E_1)/kT} \tag{2.18}$$

which means $N_2 < N_1$ if $E_2 > E_1$, and consequently $N_2 W_i < N_1 W_i$. However, in the equilibrium state, both rates should be equal. This can be arranged by postulating [101] that there is the a second component in $W_{2\to1}$ independent of intensity:

$$W_{2\to1} = BI + A \tag{2.19}$$

$$W_{1\to2} = BI \tag{2.20}$$

Now the equilibrium condition $N_2(BI + A) = N_1 BI$ can be satisfied for any temperature T by the correct choice of A/B. Transitions associated with the Einstein A coefficient are referred to as *spontaneous*. The quantity t_{spont} used above is the inverse of A.

Amplifying media. *Induced transitions* (those associated with the B coefficient) are of major importance for coherent light amplification in lasers. Let us assume that

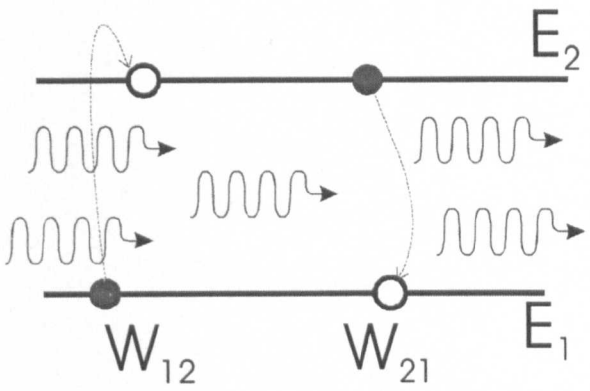

Figure 19. Upward and downward optically induced transitions in a schematic two-layer atomic system.

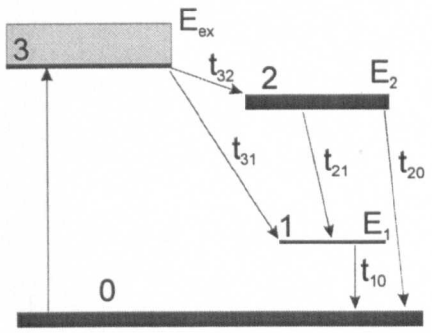

Figure 20. Scheme of a 4-level atomic system. See text for the relationship required between decay times t_{ij} for an inverted population ($N_2 > N_1$) to occur.

by some means we succeeded in elevating a large number of atoms to the upper energy state, so that $N_2 > N_1$. If light of the right frequency is propagating through such a media, the induced downward transitions will occur with a higher rate than the upward ones. Thus the number of quanta of propagating radiation will increase, which means optical power density generation rate

$$p = \frac{P}{V} = (N_2 - N_1) W_i h\nu \tag{2.21}$$

This radiation is added *coherently* (that is, with a definite phase relationship) to that of the travelling wave. In the ideal case of absence of dissipation, the intensity of the wave propagating in the x-direction increases according to:

$$\frac{dI_\nu}{dx} = \left[(N_2 - N_1) \frac{c^2 g(\nu)}{8\pi n^2 \nu^2 t_{spont}} \right] I_\nu = \gamma(\nu) I_\nu \tag{2.22}$$

where the W_i is substituted from (2.17), and the *gain* $\gamma(\nu)$ is introduced.

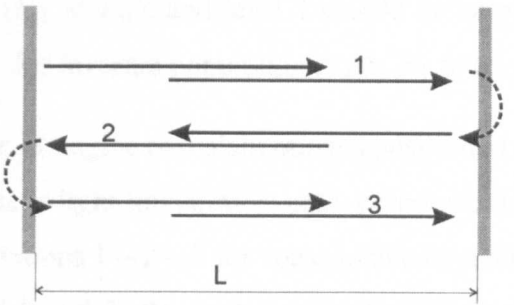

Figure 21. Optical resonator with plane mirrors.

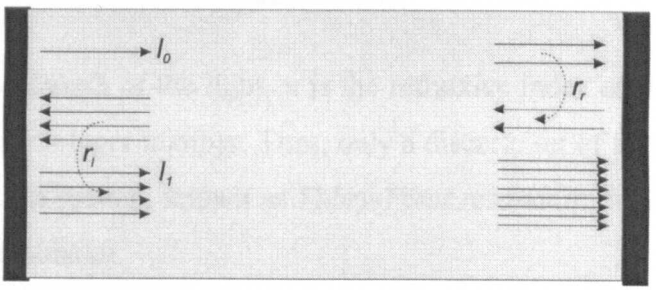

Figure 22. Electro-magnetic field evolution in case of amplifying media placed inside optical resonator (Scheme of laser operation).

The solution is

$$I_\nu(x) = I_\nu(0)\, e^{\gamma(\nu)x} \tag{2.23}$$

This means that the intensity grows exponentially when the population is *inverted* ($N_2 > N_1$) or is attenuated otherwise. The media in which $N_2 > N_1$ are referred to as *amplifying media.*

To create such a medium, that is to invert the population of the atomic energy levels, for a basic example, optical excitation at a frequency higher than ν, can be used. Obviously, excitation at a frequency ν cannot produce the inverted population, because it would stimulate both upward and downward transitions with the same rate. More than two atomic levels should be used in the process. The 4-level scheme, used in most lasers, is shown in Figure 20.

The excitation frequency is adjusted so that it brings electrons from ground 0-state up to the 3-state. These then relax from level 3 to levels 2 or 1. Both 2 and 1-states relax back to the ground 0-state but with different rates. Level 3 should relax to level

2 faster than to level 1 ($t_{32} < t_{31}$), and level 1 should be emptied faster than level 2 ($1/t_{21} + 1/t_{20} < 1/t_{10}$), for inverted population $N_2 > N_1$ to be possible.

Optical resonator. Imagine two plain mirrors positioned toward each other as in Figure 21. Suppose there is light travelling exactly perpendicularly to the mirrors. After two consecutive reflections 1→2→3 for constructive interference to occur between components of the field 1 and 3, the mirror separation L should obey the following relationship:

$$2Ln = m\lambda \tag{2.24}$$

where λ is the wavelength of the light, n is the refractive index of the media between mirrors and m is any integer number. Thus, only a discrete set of allowed wavelengths is possible for such a system, known as *Fabry-Perot resonator*, which is the simplest case of an optical resonator.

Laser. Imagine now that an amplifying media is placed inside a resonator. A plain wave of an electromagnetic field would bounce between the mirrors. The energy stored in the wave would increase with the distance travelled (2.23), and the consequent reflections would interfere constructively provided the resonator (the distance between the mirrors) is adjusted accordingly (2.24). Consider a light (an electromagnetic wave) with intensity I_0 travelling from left to right in the resonator (Figure 22). When this wave comes to the same point, having travelled all round the resonator, its intensity is changed to $I_1 = r_r r_l I_0 e^{2(\gamma-\alpha)L}$ where r_r and r_l are the reflectivity of the right and left mirrors, γ is the gain (2.22), and α accounts for all the distributed losses like scattering and absorption. Thus, for the intensity of travelling light to increase, the condition

$$r_r r_l e^{2(\gamma-\alpha)L} > 1 \tag{2.25}$$

has to be fulfilled. This is called the *amplitude oscillation condition.* The *phase oscillation condition* is (2.24), which ensures the constructive interference of all the reflections in the resonator. It is worth pointing out here that $r_r r_l < 1$ in a real resonator, otherwise no useful light would come out. That is why it is required that $\gamma > \alpha$. The *geometrical losses* (due to some portion of light missing the mirror) are not included in (2.25), which also raises the γ value required for oscillations.

Using (2.22) for γ in amplifying media, the *threshold value* (when laser oscillation becomes possible) of the population inversion $N_2 - N_1$ can now be found as

$$N_t \equiv (N_2 - N_2)_t = \frac{8\pi n^2 t_{spont}}{g(\nu)\lambda^2}\left(\alpha - \frac{1}{L}\ln r_r r_l\right)$$

To conclude the overview of the basic laser physics, it worth noticing that usually there are several resonant frequencies ν_m satisfying the phase condition of the resonator (2.24) within the ν-range satisfying the amplitude condition (2.25). Thus, several *longitudinal* laser modes are possible in most situations. Different *transversal modes* can also be generated depending on the field distribution in the directions transversal to the propagation direction.

2.5.2 Semiconductor lasers

Gain condition in semiconductors. As was shown above (2.10), optical absorption in semiconductors follows the dependance

$$\alpha(\omega) = K(\hbar\omega - E_g)^{1/2} \tag{2.26}$$

Now assume that by some means we can prepare a semiconductor crystal in which (at 0K temperature) states up to some level in the conduction band are all occupied, and those above a certain level in the valence band are empty. This situation can be discussed in terms of quasi Fermi-levels E_{Fc} and E_{Fv} , as shown in Figure 23.Now all the arguments of (2.10) can be repeated with one difference, that the upper (conduction band) states are occupied, while the lower (valence band) states are empty. Downward transitions occur rather than the upward ones, the sign of the absorption coefficient is reversed, and (2.26) gives the equation for gain $\gamma(\omega)$, rather than absorption. Summarising these conclusions, for $\hbar\omega < E_g$ there is no absorption and no amplification, for $E_g < \hbar\omega < E_{Fc} - E_{Fv}$ amplification occurs: $\gamma(\omega) = K(\hbar\omega - E_g)^{1/2}$, and waves with $\hbar\omega > E_{Fc} - E_{Fv}$ will still be absorbed.

Extending this consideration to non-zero temperatures, we must include in the integral the probabilities of initial state being occupied and of the final state being free. The net rate for the downward ($b \rightarrow a$) transitions is found by subtraction of upward ($a \rightarrow b$) transitions from the total number of downward transitions.

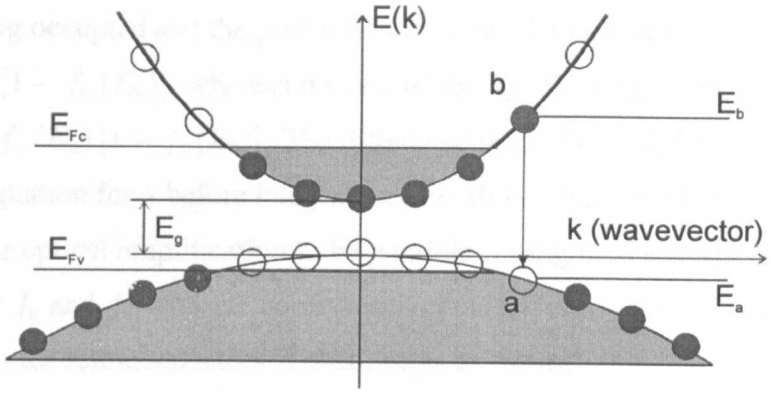

Figure 23. Schematic band structure of semiconductor with two separate quasi-Fermi levels (split by optical pumping or by electric current supplying electrons to the conduction band and holes to the valence band).

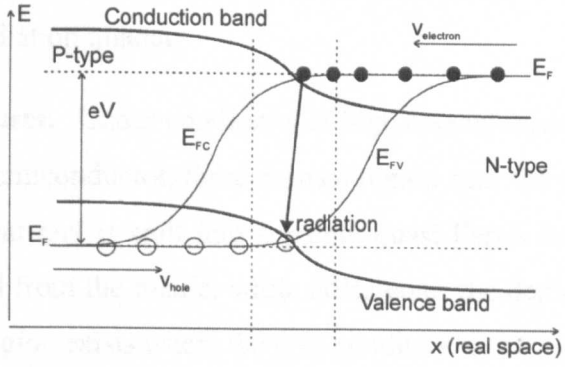

Figure 24. Scheme of p-n junction laser operation.

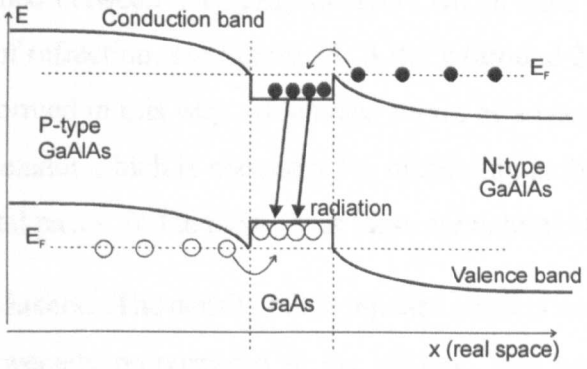

Figure 25. Quantum well laser. The carriers are confined in a 2D well with a narrower bandgap.

The rate of downward transitions is proportional to the product of the probability of state b being occupied and the probability of state a being empty, which, using (2.3), gives $f_c(E_b)[1 - f_v(E_a)]$, whereas the rate of the upward transitions is similarly proportional to: $f_v(E_a)[1 - f_c(E_b)]$. The difference is $f_c(E_b) - f_v(E_a)$, which is to be included in equation for γ before integration over all k-values. $f_c(E_b) - f_v(E_a)$ should be positive for optical amplification to be possible. Using the Fermi-Dirac distribution laws (2.3) for f_c and f_v with the corresponding quasi-Fermi levels E_{Fc} and E_{Fv} , the gain condition for semiconductors is obtained in the form:

$$E_{Fc} - E_{Fv} > \hbar\omega \tag{2.27}$$

Optical gain in semiconductor is only possible when the Fermi level is split into separate quasi-Fermi levels with $E_{Fc} > E_{Fv}$, and the separation of quasi-Fermi levels is higher than the energy of radiation quanta.

P-N junction laser. Under conditions of high current injection in a p-n junction of a direct bandgap semiconductor, there exists a region near the depletion layer where the Fermi level is bent and is split into separate quasi-Fermi levels as in Figure 24. Electrons are injected from the n-side, while holes enter the depletion region from the p-side. Thus, a thin region exists where the gain condition (2.27) is satisfied . Therefore, for an electromagnetic wave with the right frequency ω ($E_g < h\omega < E_{Fc} - E_{Fv}$), optical amplification occurs. P-N junction lasers operate in this way.

Modern semiconductor injection lasers utilize a multilayer structure of a GaAs active layer sandwiched between $Ga_{1-x}Al_xAs$ layers which have a higher energy gap and a smaller index of refraction, see Figure 25. A thick (around 200 nm) and uniform amplifying layer is formed in this way, which also serves as a waveguide for the emission. The optical resonator which is necessary for oscillation is formed by polishing a pair of opposite crystal paces. In the most cases these are natural cleaved faces.

Quantum well lasers. The density of the injected carriers is directly proportional to the current and inversely proportional to the volume, into which the carriers are injected. That is why, by making the thickness of the active layer smaller it is possible to decrease the *threshold current* required for oscillation (the minimum current under which the gain condition is satisfied). This is used in quantum well lasers.

In a typical quantum well laser, a thin active layer (around 10 nm thick) is sandwiched between thicker layers of a material with a wider bandgap. The carriers are free to move in the x and y directions, but are confined in the z direction, perpendicular to the layers.

The major result of this confinement is the step-like density of states for 2D confined carriers. The main differences from the usual heterojunction laser are: firstly, the threshold current is lowered due to the volume decrease; secondly, the equal increments of current yield larger increments of gain in quantum well lasers, due to the effects of the reduction of the volume to which the carriers are supplied together with the reduced dimensionality in k-space, thirdly, there are steps in the current-gain characteristic corresponding to the next confined state of the carriers added.

2.5.3 Nanocrystalline silicon as a lasing material?

The discovery of efficient luminescence from porous silicon raised a worldwide interest in the material in view of possible optoelectronic applications. Porous silicon-based LEDs have been demonstrated. Although the parameters and manufacturability

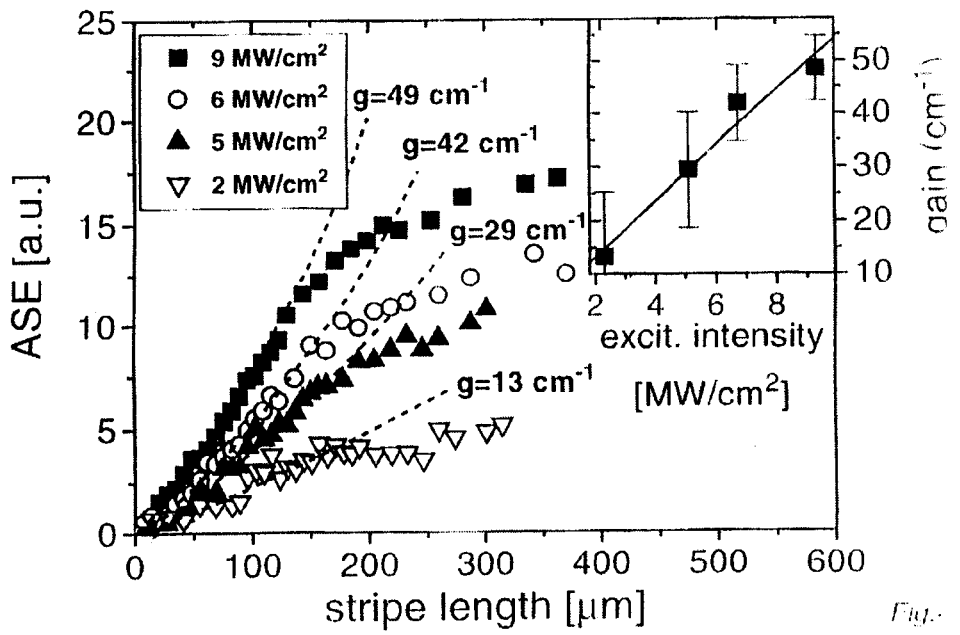

Figure 26. A reproduction of the graph showing gain in silicon nanocrystals, presented by Chech scientists (see ref. in text).

of these devices are not sufficient yet to meet the requirements for displays or integrated optics, the characteristics are gradually improving, along with a better understanding of the physics involved. Now the search for nanocrystalline-silicon-based light-emission shifts its interests toward other techniques of nanocluster fabrication, discussed above. As a further step, the discussion is open as to the possibility of creating a coherent light source using silicon nanocrystals as an optically active material. The first positive experimental result on gain measurement in silicon nanocrystals embedded in a silicon dioxide matrix has recently been reported [64], where silicon nanocrystals were produced by ion implantation [102]. When first reported at an E-MRS June 1998 symposium in Strasbourg, the news of 50 cm^{-1} gain in silicon became the main sensation of the meeting. A copy of the graph presented by the group is shown in Figure 26. The gain was measured by the usual *strip-length technique*, when the change of photoluminescent intensity is measured versus the length of the optically pumped active region.

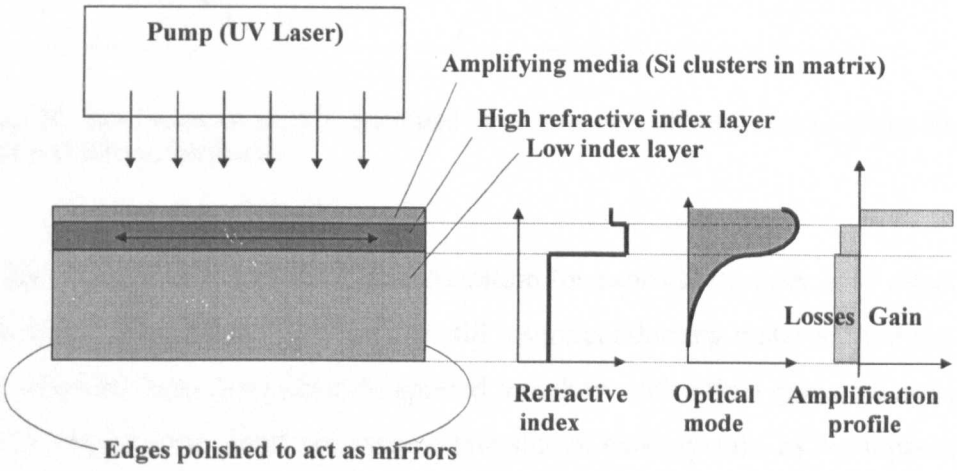

Figure 27. A conceptual drawing of nc-Silicon laser. The optical mode is guided in a planar vaweguide, amplification occurs in the top layer, which consists of silicon nanocrystallites in some matrix. Optical resonator is formed by polished side faces of the structure.

Unfortunately, the accuracy of the measurements does not allow one to draw an unambiguous conclusion. Since then, the discussion is still going on as to whether the reported results were reliable, and what are the next steps in verification of the theoretical and technological possibility of nc-silicon lasers. If optical gain would be

achieved in silicon nanoclusters in some matrix, that would open the possibility for all-silicon lasers to be used in silicon technology rather than integrated GaAs lasers. This would mean great advantages of manufacturability and cost-effectiveness. A conceptual drawing of a nc-Si laser device is shown in Figure 27.

The question of pumping electrons up to the top energy level with a sufficient rate is of the major importance. Firstly, the optical excitation with pumping light quanta of higher energy than that of emitted light could be used. Secondly, electrical pumping should be the final goal as it is needed for possible electronic applications of the device. In the context of electrical pumping, there is no fundamental difference from the free carrier injection in non-coherent light-emitting devices which was previously discussed in section 2.3.

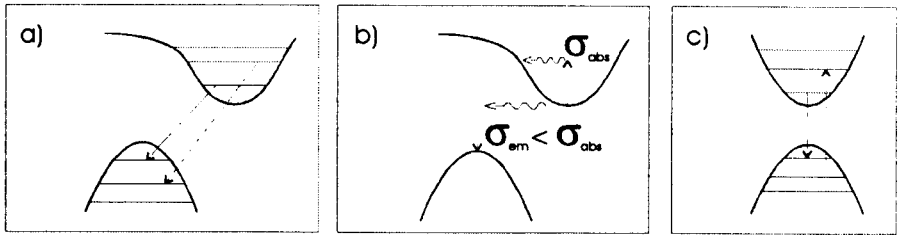

Figure 28. Band schemes used in simplified models for optical transitions in silicon nanocrystals (see text for explanations).

The theoretical question of gain condition for nanosilicon laser is of interest. On the one hand, nanocrystalline silicon is still a semiconducting material, and the terminology of quasi-Fermi levels is to be applied somehow with a final gain equation similar to (2.27). On the other hand, we assume that silicon nanocrystals, as we suppose, have discrete energy levels for electrons and holes corresponding to different envelope wavefunctions defined by the confinement potential (this is treated in detail in subsection 2.6.1). Therefore, an energy diagram similar to that of a separate atom or a molecule (see Figure 20) should be possible, with the final oscillation condition similar to $\gamma > 0$, with gain γ from (2.22).

The next question is whether nanocrystalline silicon should be considered as a direct or an indirect semiconductor. There was experimental (subsection 2.2.2) and theoretical (subsection 2.6.2) evidence for both the direct and indirect nature of its band structure. The scheme in Figure 28 (a) is usually used in discussions of interband tran-

sitions in porous silicon, with quantised levels shown within the indirect band scheme. The drawing in Figure 28 (b) was presented by Philippe Fauchet, the recognised authority in the field of electroluminescence and device integration of porous silicon, in one of his seminars [103] to argue the impossibility of optical gain in silicon: the cross-section of free carrier absorption σ_{abs} is always higher than that of indirect radiative recombination σ_{em}, making absorption processes dominate. This means no positive optical gain. However, if the band diagram of the silicon nanocrystal was more like that in Figure 28 (c), this would mean a fundamental physical possibility of the positive optical gain in nanocrystalline media. The relevant field of theoretical physics is currently being developed, and the basics of it are presented in the next section.

2.6 Theory and computations of optical properties of semiconductor quantum dots

This section describes the relevant theory. It completes the review of the present physical knowledge and practical results in the field of electronic and optical properties of semiconductor nanocrystals. It should not be regarded as the full coverage of the subject, but just as the minimum basic information necessary for correct interpretation of the results presented, and for understanding of the speculations offered in Chapter 3, as well as of some of the points made before in subsections 2.2.1 and 2.2.2. Besides, the information presented here completes the knowledge required for thoughtful further research in the field.

2.6.1 Semiconductor Quantum Dots

Solutions of Schrodinger equation for a spherical quantum dot. Stationary states $\Psi(\mathbf{r})$ of a particle with energy E in a potential well $U(\mathbf{r})$ are found by solving the time-independent Schrodinger equation [19]:

$$\left[-\frac{\hbar^2}{2m}\nabla^2 + U(\mathbf{r})\right]\Psi(\mathbf{r}) = E\Psi(\mathbf{r}) \tag{2.28}$$

When a semiconductor quantum dot is approximated as a 3-dimensional quantum well, m in (2.28) is the effective mass of the particle, which is influenced by the crystal structure of the quantum dot material, E is the confinement energy added to the Bloch energy $E_{K=0}$ (Appendix A), and $\Psi(\mathbf{r})$ is the envelope part of the total wavefunction. The *effective mass approximation* is an important point of the theory. We assume here that a nanosized semiconductor particle is roughly spherical, so that a potential well can be described as: $U(\mathbf{r}) = 0$, for $|\mathbf{r}| < R$; and $U(\mathbf{r}) = U_0$, for $|\mathbf{r}| > R$. This potential is schematically shown in Figure 29 (a). First, we treat the potential well as infinite ($U_0 = \infty$), Figure 29 (b). In this idealised case, the boundary condition for (2.28) is that the wavefunction $\Psi(\mathbf{r})$ vanishes at the barrier:

$$\Psi(\mathbf{r})\,|_{|\mathbf{r}|=R} = 0 \tag{2.29}$$

Using the spherical symmetry of the problem, the variables can be separated:

$$\Psi(\mathbf{r}) = \phi_l(r)\, Y_{l,m}(\theta, \varphi) \tag{2.30}$$

Angular momentum conservation for the particle motion allows one to reduce the problem to a differential equation with one variable r :

$$-\frac{1}{r}\frac{d^2}{dr^2}\left(r\phi\left(r\right)\right)+\left(\frac{l\left(l+1\right)}{r^2}-k^2\right)\phi\left(r\right)=0 \tag{2.31}$$

where $l\left(l+1\right)$ is the eigenvalue of the spherical harmonic part of the wavefunction $Y_{l,m}(\theta,\varphi)$, indexes l and m are the angular quantum numbers (see ref. [19]), and k is the energy eigenvalue:

$$\hbar^2k^2=2mE \tag{2.32}$$

The solutions are spherical Bessel functions $J_l\left(kr\right)$ [104] , with allowed quantised k-values determined from (2.29), which now has the form $\phi_l\left(r=R\right)=0$. The eigenstates have $\phi_{n,l}\left(r\right)Y_{l,m}(\theta,m)$ envelopes, where n is the radial quantum number, corresponding to the number of the allowed k-eigenvalue[7]. The total wavefunction is the product of the confined envelope function and a Bloch wave discussed in Appendix A.

The examples of the radial and angular parts of the lowest eigenfunctions are shown in Figure 30. A set of allowed energies is found from (2.32) :

- for *s-states* $\{l=0,J_o\left(x\right)=\sin\left(x\right)/x\}$ with $kR=\pi n$; where $n=1,2,...$
- for *p-states* $\{l=1,J_1\left(x\right)=\sin\left(x\right)/x^2-\cos\left(x\right)/x\}$ with $\tan\left(kR\right)=\left(kR\right)$; etc.

The eigenfunctions are the same for both electrons and holes (the electrostatic energy in (2.28) has been disregarded in comparison with the confinement energy), however the energies of electron and hole may differ due to different effective masses m_e and m_h.

A schematic plot of the single particle energy levels for electrons and holes is shown in Figure 31, together with the energy band diagram of an idealised bulk semiconductor. For the energy of a confined electron-hole pair, using (2.32) and $kR=\pi n$ we have:

$$E_{pair}=E_g+\frac{\hbar^2\pi^2}{2R^2}\left(\frac{1}{m_e}+\frac{1}{m_h}\right)n^2=E_g+E_Q \tag{2.33}$$

The quantity in brackets is the inverse of a *reduced electron-hole mass* m_r.

[7] Here and later we do not discuss normalisation constants, which are found by requiring that the integral of the probability density $\int\Psi^*\Psi d\mathbf{r}$ over the whole volume is unity.

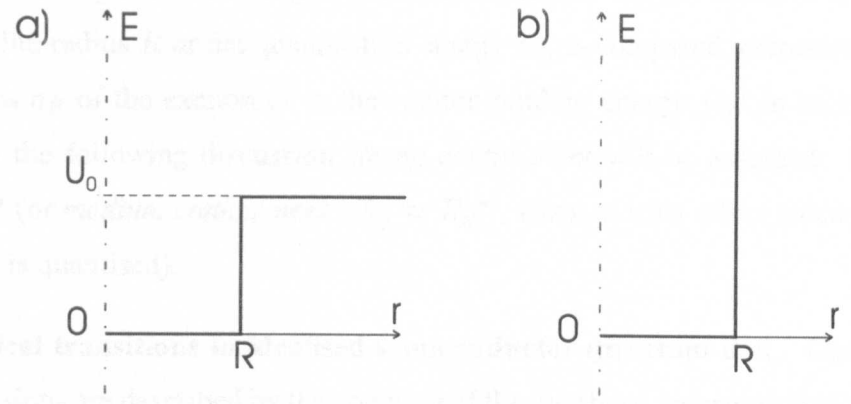

Figure 29. Spherical potential wells with finite (a) and infinite (b) barriers.

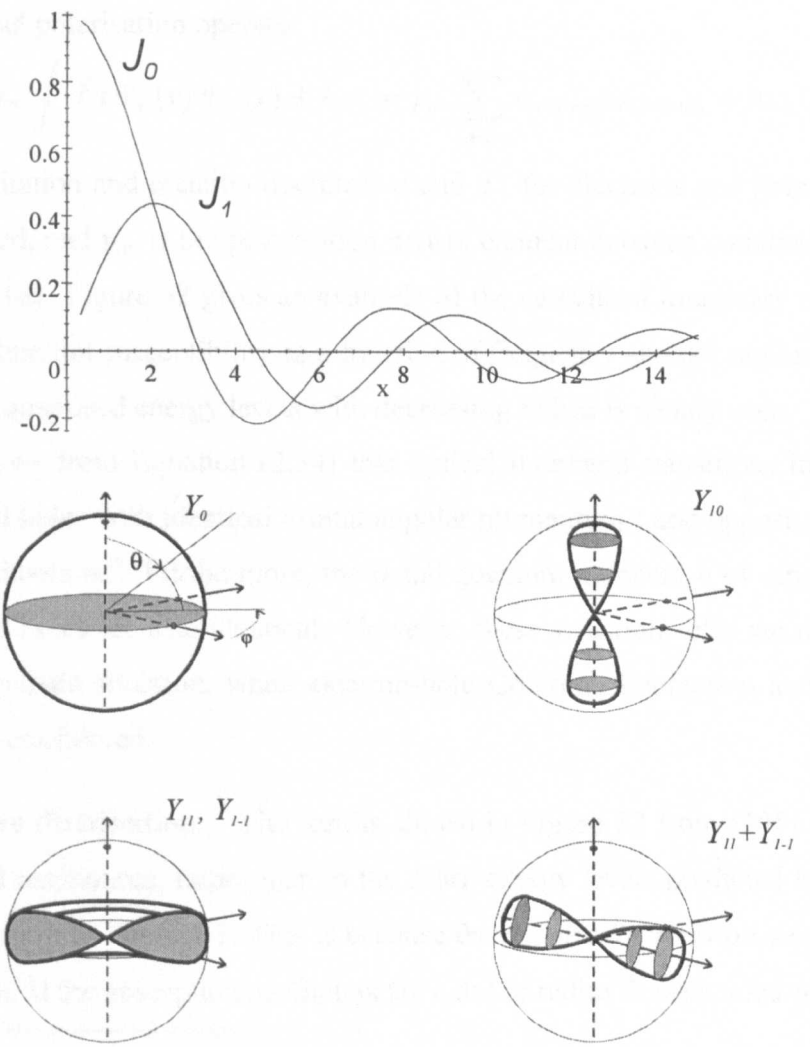

Figure 30. Examples of the lowest radial (top) and angular (bottom) harmonic components of single particle wavefunctions in a spherical potential well.

Different regimes (or strengths) of confinement are usually referred to, in which the crystallite radius R or the quantisation energy E_Q is compared, respectively, to the Bohr radius a_B of the exciton or to the exciton binding energy Ry^* in bulk semiconductor. In the following discussion *strong confinement* will be assumed: $R < a_B$, $E_Q > Ry^*$ (or *medium confinement*: $E_Q \approx Ry^*$, when at least either electron or hole movement is quantised).

Optical transitions in idealised semiconductor quantum dot. Optical interband transitions are described by the coupling of the interband polarisation to the optical electric field via the interaction Hamiltonian

$$H_1 \backsim PE\cos(\omega t)$$

with interband polarisation operator

$$P = p_{cv}\int d^3\mathbf{r}\Psi_e(\mathbf{r})\,\Psi_h(\mathbf{r}) + h.c. = p_{cv}\sum_{l,m,n} a_{e(lmn)}a_{h(l-mn)} + h.c. \qquad (2.34)$$

where annihilation and creation operators a and a^+ for electrons and holes in (lmn)-states are used, and p_{cv} is the polarisation matrix element between conduction and valence band [18]. Figure 32 gives an example of the calculated imaginary (absorptive) part of quantum dot susceptibility as a function of frequency and dot radius [105]. The blue shift of quantised energy levels with decreasing radius is clearly seen.

It follows from Equation (2.34) that optical interband transitions involve only electrons and holes with identical orbital angular momentum l and opposite azimuthal quantum numbers m[8]. Furthermore, the radial quantum numbers n of dipole-coupled electrons and holes are also identical. However, these selection rules are not the case in a more realistic situation, when electron-hole Coulomb interaction and spin-orbit coupling are considered.

Dot size distribution. The results shown in Figure 32 from [105] correspond to broadened resonances, rather than to the sharp energy levels predicted by Equation (2.33) and shown in Figure 31. This is because the *dot size distribution* was taken into consideration. If the absorption coefficient for a dot of radius R is denoted $\alpha_R(\omega)$, than

[8] To include intraband transitions (conduction-to-conduction or valence-to-valence band) which leave the number of excitons unchanged, into the calculated optical responce of a quantum dot, both envelope and Bloch parts of the wavefunctions are to be considered. The analysis in [18] shows, that the change of the angular momentum for the envelope function has to be $\Delta l = \pm 1$ in the case of intraband transition.

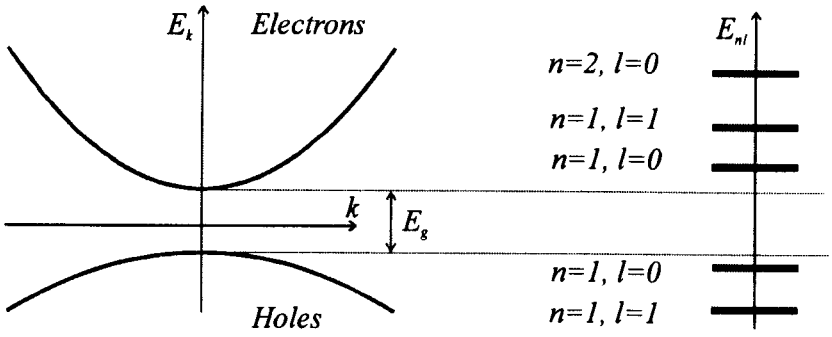

Figure 31. Quantised energy levels for electrons and holes. Bands of an idealised semiconductor are shown on the left.

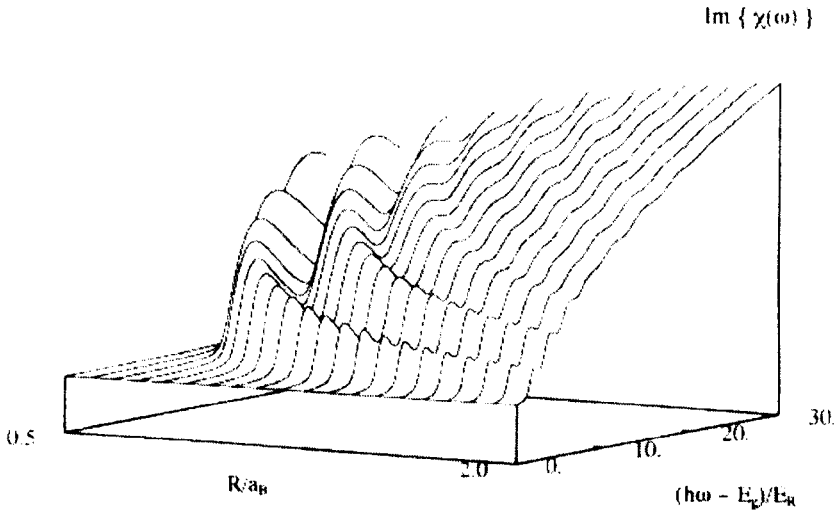

Figure 32. Imaginary part of the quantum dot susceptibility for different ratios of mean dot radius R and exciton Bohr radius in dot material a_B (see reference in text) .

the average absorption coefficient is calculated from:

$$\alpha_{average}(\omega) = \int_0^\infty \alpha_R(\omega) P(R) dR$$

where $P(R)$ is the probability distribution of dot radii. Another example of this broadening effect is shown in Figure 33 for CdS dots, where Gaussian distributions with different widths are modelled [106]. It is clear now, why the separate discrete resonances are not seen in PL data from porous or nanocrystalline silicon: the features are merged into a continuous structure for just 20% broadening of nanocrystallite sizes.

The above examples use the results for direct gap semiconductor quantum dots. This is because the theoretical approach is much more developed for this case. However,

there is no doubts that the dot size distribution has the same effect on the broadening of resonances corresponding to optical transitions between the confined states in quantum dots of indirect gap semiconductor.

In the following subsections the corrections to the idealised solutions are reviewed.

Finite barriers. The barrier at the interface of a realistic quantum dot is not infinite. That is why equation (2.31) should be considered for $r > R$ as well, with a modified $k^2 \backsim (E - U_0)$, and the requirement of continuity of ϕ and $d\phi/dr$ in $r = R$ is used for finding the eigenenergies, rather than $\phi(R) = 0$. The solutions outside the dot ($r > R$) are exponentially evanescent spherical Bessel functions H_l [104]. Modification of the radial parts of wavefuctions are demonstrated in Figure 34 for the two lowest harmonics. The tails of wavefuctions are now propagating outside the quantum dot sphere. The effective confinement is weaker in this case: the wavefunction is spread through a larger volume in space.

Another consequence of the barriers being finite is that the number of confined states is also finite: for particle energies $E > U_0$ the solution outside the dot volume is not exponential, but of the same oscillating form as inside. No bound states exist in 3D well with $U_0 R^2 < \hbar^2/8m$.

Coulomb attraction. To include the Coulomb interaction into the theory, a potential energy term is to be added to the Hamiltonian of the confined electron-hole system. In the strong confinement regime this added term may be treated as a perturbation, because it diverges as $1/R$, while the confinement energy term diverges as $1/R^2$. Besides the change produced to the single particle energy E_Q, another consequence of Coulomb interaction is the change to the shape of idealised wavefunctions (2.30): unperturbed states are mixed, and the selection rules derived from (2.34) are no longer valid. Calculations show the radial distribution of holes and electrons shift toward the center of the dot, with hole shifted more than electrons [18].

Interface polarisation. If a point charge is placed inside a sphere with dielectric constant ε_1 and a sphere itself is embedded in an infinite medium with dielectric constant ε_2, the induced surface polarisation charges at the $\varepsilon_1/\varepsilon_2$ interface will act at a point charge, giving a contribution to the total energy of the system. If more than one point

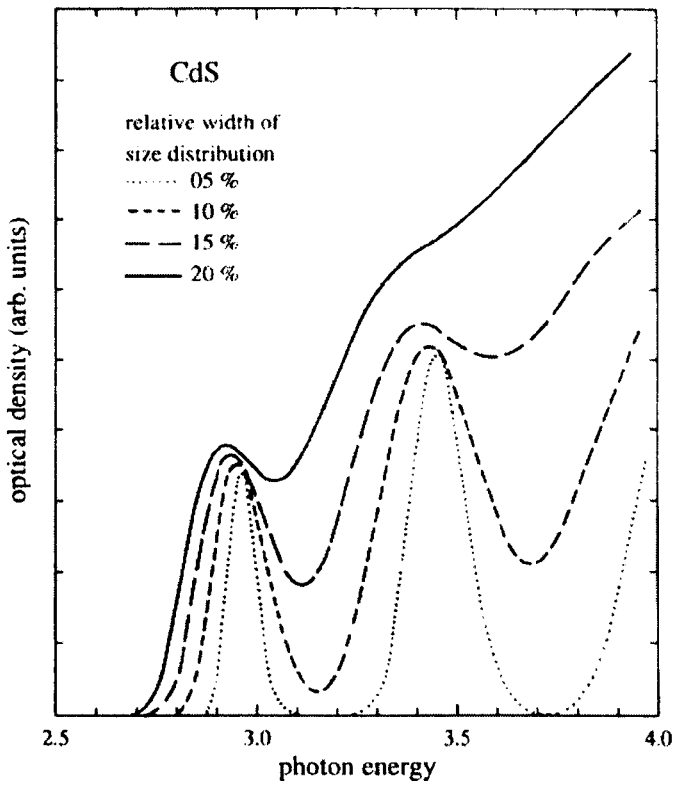

Figure 33. Absorption of CdS quantum dots with a Gaussian size distribution, different relative widths of distribution are indicated (see ref. in text).

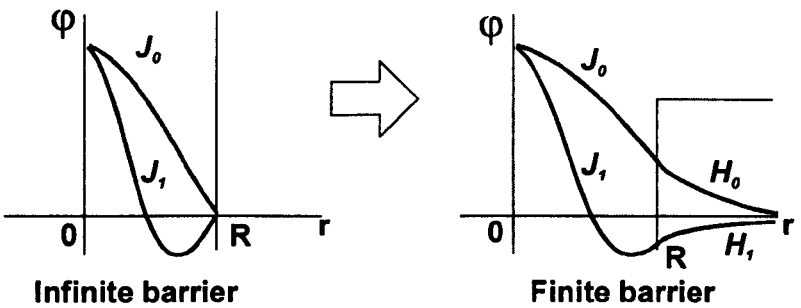

Figure 34. Illustration of the effect of finite barriers on the shape of single particle wavefunctions.

charge is present, the total electrostatic energy of a system is given by the summation of not only the mutual Coulomb interaction terms $q_i q_j/\varepsilon_1 |r_i - r_j|$, but also the interaction terms of each point charge with the surface polarisation charges induced by itself and by all the other charges. The final equation can be found in [18]. This complication makes it more difficult to include electrostatic effects into the analytical theory.

The numerical approach to finding single particle states in such a system is also complicated. For a finite barrier height, the probability density to find a particle outside the dot and on the interface is not zero. The discontinuity of the dielectric constant at the interface leads to the divergence of charge *self-energy* at the interface. To avoid this, a linearly approximated regularised surface potential is used, with thickness of the "cut off" surface layer of the order of interatomic distance. A surface quantum well is formed on the lower-dielectric-constant side of the interface, where a particle may be trapped. Solutions corresponding to surface states are obtained in this way.

Spin-Orbit coupling. If the spin of the electron (or a hole) is taken into consideration, splitting of energy levels occurs, depending on spin s and orbital angular momentum l of a particle being parallel or antiparallel. Further splitting occurs for $k \neq 0$ between so called *light and heavy holes*, depending on the projection of the total angular momentum j_z [107]. The resulting single particle states are the normalised linear combinations of the states found initially (2.30). Calculations suggest, that a hole is shifted toward the dot center even further than due to inclusion of the Coulomb interactions [18]. This again breaks the selection rules for the optical interband transitions.

Numerical schemes overview. Before discussing numerical techniques developed for quantum dots, it is worth noting the different methods used in band structure calculations for bulk crystals.

For weak periodic potential the simplified *nearly-free-electron approximation* can be used, where the band structure is constructed by plotting the values $E(\mathbf{k}) = \hbar^2 (\mathbf{k} - \mathbf{K})^2 / 2m$ for all reciprocal lattice vectors $\mathbf{K}$. Energy gaps are obtained as a result of splitting $E(\mathbf{k})$ graphs at places of band crossing.

The opposite approach is the *Tight-Binding method*, which starts from individual atomic orbitals and considers the overlap of wavefunctions with the Hamiltonian component ΔU caused by the presence of neighbouring atoms. Linear combinations of atomic orbitals (LCAO) centered at each atom, the so called *Wannier functions*, account for the effect of ΔU, and combinations of those over all sites in the lattice are then chosen to satisfy the Bloch condition $\Psi(\mathbf{r} + \mathbf{R}) = e^{i\mathbf{k}\mathbf{R}} \Psi(\mathbf{r})$.

To find the valence states the *Orthogonalised Plane-wave* (OPW) *method* is often used, where waves in the form $\Psi_{\mathbf{k}} = e^{i\mathbf{k}\mathbf{r}} + \sum b_{core} \psi_{\mathbf{k}}^{core}(\mathbf{r})$ are used with coefficients b_{core} chosen so that $\Psi_{\mathbf{k}}$ is orthogonal to all core wavefunctions $\psi_{\mathbf{k}}^{core}(\mathbf{r})$, while $\psi_{\mathbf{k}}^{core}(\mathbf{r})$

are found by tight-binding approach. Because the core functions are localised about lattice points, the waves $\Psi_{\mathbf{k}}$ are very close to single plane waves $e^{i\mathbf{kr}}$ in the interstitial regions.

In the *Pseudopotential method* the smooth part $\sum_k e^{ikr}$ of the combination of orthogonalised plane waves $\sum_k \Psi_{\mathbf{k}}$ (see above) is found as a solution of the Schrodinger equation with Hamiltonian, which includes the *pseudopotential* formed as a sum of the crystal potential and the effects of rapidly oscillating $\sum_k \sum b_{core}\psi_{\mathbf{k}}^{core}(\mathbf{r})$ parts. The last mentioned contribution to the Hamiltonian depends on the energy corresponding to $\sum_k \Psi_{\mathbf{k}}$. That is why the Pseudopotential method is applicable in those cases, when the wavefunctions with particular energies are being sought. For a typical example, by using the known Fermi energy when defining the pseudopotential, electron states close to the Fermi level can be found.

Methods developed for quantum dots are reviewed below.

Variational calculations. This approach was successfully used to calculate ground and first excited exciton states and energies for quantum dots with finite barriers, including Coulomb interaction [108]. For example, a test function

$$\psi(\mathbf{r}_e, \mathbf{r}_h) = e^{-\lambda_s|\mathbf{r}_e - \mathbf{r}_h|}\phi_e(r_e)\,\phi_h(r_h) \tag{2.35}$$

with one-particle ground s-states $\phi_e(r_e)$ and $\phi_h(r_h)$ found from (2.31) was used for the ground exciton state calculation. The ground state energy E_s of interacting electron-hole pair is computed from the expectation value of the Hamiltonian

$$\hat{H} = -\frac{\hbar^2\Delta_e}{2m_e} - \frac{\hbar^2\Delta_h}{2m_h} - \frac{e^2}{\varepsilon|\mathbf{r}_e - \mathbf{r}_h|} + U_e(r_e) + U_h(r_h)$$

which includes the Coulomb interaction term, by minimising the expression

$$E_s = \int d\mathbf{r}_e \int d\mathbf{r}_h \psi(\mathbf{r}_e, \mathbf{r}_h)\,\hat{H}\psi(\mathbf{r}_e, \mathbf{r}_h)$$

with respect to the variational parameter λ_s. Different particle masses inside and outside the dot are also taken into account when choosing $\phi_e(r_e)$ and $\phi_h(r_h)$. The first excited state is calculated by similar minimisation of a more complex test function, with two variational parameters, one of which is fixed by the requirement of orthogonality with the ground-state wavefunction.

Matrix Diagonalisation Technique. On the contrary to variational calculations, where the choice of test functions is arbitrary, and there is no systematic way to

check the accuracy of the result, the matrix diagonalisation technique allows one to improve the accuracy by increasing the number of basis functions used for calculation. The convergence of the result with the increase of the number of basis functions (the dimension of function subspace) confirms the validity of the technique. The energy is minimised on a linear subspace of a finite subspace of kinetic energy eigenfunctions, which is equivalent to the diagonalisation of the finite Hamiltonian matrix taken on the considered orthogonalised set of eigenfunctions. The Hamiltonian

$$\hat{H} = -\frac{\hbar^2 \Delta_e}{2m_e} - \frac{\hbar^2 \Delta_h}{2m_h} - W(\mathbf{r}_e, \mathbf{r}_h)$$

includes not only electron-to-hole Coulomb interaction, but also surface polarisation effects. This approach is demonstrated in [109], for example, where energies of the lowest one-pair and two-pair states are reported for dot radii comparable to the exciton Bohr radius a_B ($0.25 < R/a_B < 5$). A good agreement with perturbation theory results is shown for R values in the region of validity of perturbation approach.

Lattice model. The effective mass approximation fails for dot sizes comparable to the interatomic distance. Besides, the lowest allowed value of wavevector k may be beyond the domain of $E(\mathbf{k})$ parabolicity anyway. To overcome these problems a theory was developed [110] for very small crystallites considered as huge molecules with N ions placed on a perfect crystal lattice by connecting the successive shells of nearest neighbours. Unfortunately, a theoretical Coulomb correction should be applied to the results, as the approach is purely one-particle. Extra care is devoted to the surface (passivation, relaxation of dangling bonds, etc.). The results reported show narrower band gaps than those predicted by the effective-mass approximation, whereas experimental results are mostly reported in-between the values obtained using these two approaches.

2.6.2 Review of computational results for silicon nanoclusters

To describe the motion of a single particle in a potential well the Schrodinger equation (2.28) is always used. By requiring that the wavefunction vanishes outside the well, single particle states are quantised. Eigenenergies are then found from (2.32). To make use of this result the question should be considered of what value for effective mass m to use. As it is introduced in the physics of crystals (see derivation of (2.7)),

the effective mass is the inverse of the band curvature:

$$m = \left(\frac{1}{\hbar^2} \frac{d^2 E}{dk^2} \right)^{-1}$$

which depends both on the direction and the absolute value of the wave-vector k. The theory was developed for plane waves, and the results are naturally applicable for bulk crystals. However, for particles confined in small crystallites, the use of the effective mass concept is not so well justified. When the size of a quantum dot is comparable with the lattice constant of the material, which is where the main interest is for visible light-emission from silicon nanoclusters, this approach becomes invalid.

The other problem is that whatever the value of effective mass m in the middle of k-space, the $E(k)$ dependence is not parabolic even for direct-gap semiconductors. For small crystallites, even the first eigenvalue of k may be well beyond the domain of parabolicity of $E(k)$, making the Schrödinger equation invalid. Moreover, in silicon, the conduction band minimum is situated near the X-point in k-space[9], which corresponds to a plane particle wave propagating in the (001) or similar crystallographic direction. This case is not, obviously, realised in nano-crystallites.

Therefore, this thesis reports no personal numerical estimations of the band-gap width or of the optical transition energies in porous silicon or in silicon nanocrystals (for example, when discussing PL maximum position for photo-etched porous silicon or a double-Gaussian shape of polarised PL from silicon nanowires in Chapter 3). Such estimations are sensitive to the effective mass value used, and the conclusions would hardly be authentic.

Besides providing information on the recognised published computational results, the aim of the following review of selected theoretical papers is to demonstrate the ways for overcoming the difficulty formulated above either by some qualitative arguments or by modifying (if not avoiding) the effective mass approximation.

Porous silicon and quantum wires. Soon after the quantum confinement model of visible luminescence from porous silicon was put forward [8], the results of first-principles calculations for silicon nanowires were reported. In work [111] pseudopotential calculations for wires of 4×5, 6×7 and 8×9 atoms cross-section are discussed.

[9] The conduction band minima of bulk silicon are situated at $\pm (0, 0, 0.85)\, 2\pi/a$ and four other symmetrical points in k-space, where a is the lattice constant.

Due to the nature of the problem, sufficiently different from that for a bulk crystal, several specific approximations are used to make the problem suitable for the pseudopotential technique. 3D periodicity is artificially achieved by considering an array of parallel equidistant wires. Surface bonds of silicon are assumed to be saturated by bare H^+ ions. A truncated set of plane waves is used with energies of up to $6Ry$, which does not allow an accurate description of states with large weight on H atoms. The one-dimensional band structure of silicon wires was found to be direct, as expected due to the confinement induced up-shift of all six conduction band minima. The calculated value of the band gap upshift for 8×9 wires is in full agreement with the effective mass predictions for the corresponding wire diameter, whereas values for thinner wires are lower than those predicted. On the other hand the calculated positions of photoluminescence maxima and radiative lifetimes are in good agreement with the experimental values.

In their later work [112], the same authors present further study of the validity of effective mass approximation for silicon nanowires. Their first principle calculations show that in rectangular wires the states in the maximum of the valence band are composed of p-orbitals: the p_z-orbital pointing along the wire and p_{long} and p_{short} orbitals pointing along the long and short sides of the rectangular cross section of the wire respectively, with energy of p_z state being situated between the other two states. On the other hand, effective mass theory predicts the largest effective mass for p_z states. As in the previous work, the calculated confinement induced energy shifts are sufficiently lower than those predicted by effective mass theory.

The electronic band structure for silicon wires oriented in other than (001) directions were calculated in [113] using LCAO. It was found that for nanowires oriented along (110) and (111) directions, the one-dimensional band structure is essentially indirect. Another interesting remark in this work is that for (001) wires the corner silicon atoms accumulate a sufficient positive electric charge ($0.21e$), which makes the structure unstable and causes lattice relaxation to form a rounded structure. It was also found that the conduction band is formed mostly by the surface atoms, which differ sufficiently from bulk silicon atoms in their electronic configuration. This means therefore additional complications in the use of effective mass theory for such structures.

Another approach for the calculation of properties of silicon wires is demonstrated in [114]. The densities of states are evaluated for 4×5 and 3×4 wires, and optical

properties are computed by evaluating the imaginary part of the dielectric function. The main conclusions are:

- quantum confinement is the origin of the opening of gap in the density of states,
- the opening is asymmetric: 2/3 of the opening is in the conduction band and 1/3 is in the valence band,
- the near band gap states originate from Si atoms located at the centre of the wire[10],
- the confinement is enhanced in the case of free (not passivated) surface,
- the imaginary part of the dielectric function is strongly anisotropic to the low energy side, which could explain some polarisation effects of photoluminescence,
- the presence of dangling bonds destroys the luminescent properties.

Silicon quantum dots. One of the earliest works on 3D quantum confinement effects in indirect-gap materials is [115]. A variational approach (2.35) was used with the electron kinetic energy term of the Hamiltonian approximated using longitudinal and transverse effective masses in the vicinity of $k_0 = (0, 0, 0.85)$ and five other symmetrical conduction band minima:

$$K_c = \frac{\hbar^2}{2m_{\parallel}} (k_{\parallel} - k_0)^2 + \frac{\hbar^2}{2m_{\perp}} k_{\perp}^2 \tag{2.36}$$

The reported results for exciton energies are in good agreement with experimentally measured positions of photoluminescence maxima for different quantum dot sizes, although the validity of (2.36) is not discussed and the effective masses used are not reported. A strong dot size dependence of the radiative lifetime of excitons is noted: it varies from nanoseconds to milliseconds corresponding to dot diameters from 1 to 3 nm. This is due to the fact that in the calculation, the dipole matrix element of the transition is proportional to the Fourier component of the envelope functions at the k-value corresponding to the conduction band minimum: smaller crystallites have broadened $\Psi(k)$ envelopes.

Highly efficient luminescence due to structural disorder was also measured in amorphous silicon [116]. An interesting question therefore arises of the compound ef-

[10] This point is in contradiction to the results of the previous reviewed work [113].

fects in confined structurally disordered systems. The electronic structure of amorphous silicon nanoclusters was studied in [117]. The confinement-induced energy band shifts, densities of states and recombination rates are calculated for amorphous Si and amorphous Si:H nanoclusters using the tight-binding method. Defect states are classified into those which are strongly localised, and show no confinement induced blue shift, and those delocalised or weakly localised, giving rise to the size-dependent properties of nanoclusters. The characteristics are found to be similar to those of crystalline silicon nanostructures, except for the recombination rates for crystallites larger than 2.2 nm, where the result is two orders of magnitude higher due to disorder induced effects. The last observation is, probably, related to the fact, that disordered silicon structures produce blue rather than red luminescence: only the fraction of nanocrystals with smaller sizes contributes to luminescence. Nonradiative disorder effects on the other hand prevail in larger crystallites. The subject is also interesting in the context of silicon nanoclusters produced by ion-implantation or by chemical vapor deposition, where the amorphous fraction in silicon structures may be essential.

Extensive work on nanometer silicon quantum dots is reported in [118]. The authors use the pseudopotential method to approximate the Hamiltonian and a plane wave basis to expand the wavefunctions. The study includes: band gap versus sizes and shape, analysis of band edge states in terms of bulk Bloch functions, total electronic density of state and optical absorption spectra, lifetime versus luminescence peak energy. Agreement is found with tight-binding and other calculations, as well as with experimental results.

Concluding speculations. The above list of computational works on silicon nanostructures is far from complete, but it allows some generalising conclusions:

- In-spite of the number of specifically developed computational techniques for calculation of electron states in semiconductor quantum dots (introduced above), these are not popular with researchers working with silicon. This suggests that the indirect band structure of the bulk silicon presents an essential difficulty for analytical and computational physics.
- There is no consensus between the theoreticians on which computational technique is better (or more correct) for silicon nanocrystals, which gives the

suspicion that there was no satisfactory computational result produced so far. Further experiments might help to decide on the better computational approach.

- Whereas all reported results "are in good agreement with experimental data", the controversy as to the origin (or mechanisms) of luminescence from differently produced nanocrystalline silicon still exists, showing the disappointing fact that agreeable computational results do not bring us much closer to the answer.
- I have failed to find a theoretical paper on the subject of possibility of negative absorption (positive optical gain) in silicon nanostructures, which is not an encouraging observation concerning the future of nanocrystalline silicon as a lasing material.

An interesting observation is that, in the widely used envelope function approximation, the Bloch component of the wavefunction is taken as the bulk wavefunction with $k = 0$. In this approach the indirect nature of the silicon band structure is lost, which means that either the analytical results would be the same for quantum dots formed from indirect gap semiconductors, or that the whole model is not suitable for these dots. There is presently no consensus on this matter. Some papers state that porous silicon is clearly an indirect gap material, but direct transitions are possible due to the break-down of k-conservation rule. Others argue that due to the quantum confinement, the conduction band minima at (0, 0, 0.85) and other symmetrical points are up-shifted and folded on-to the centre of the k-space, thus making the effective energy gap direct. Some say that conduction band minimum wavefunctions have sufficient Fourier components in $k = 0$ or that confined Bloch waves centered at $k = 0$ have sufficient components at (0, 0, 0.85) minima, when explaining the possibility of no-phonon transitions within an indirect gap scheme. The references are not quoted here to emphasise that this is not a contradiction between the individual researchers, but the consequence of the physical question still being open. So far we do not have the answer whether it is possible to make direct transitions dominant in silicon nanocrystals. Therefore, it is still possible that nanosilicon could play the major role in optoelectronics of the future, and even the possibility of nanosilicon laser can not be ruled out based on the present knowledge. More focused experimental, analytic and computational research is needed before the final answer is found.

Chapter 3
Personal research results

I would rather be a good experimentalist
than a bad theoretician...

In this chapter:

3.1 Characterisation Techniques

Here a short introduction is given to experimental techniques which are referred to in this chapter. These include spectroscopy (photoluminescence and Raman scattering studies) and microscopy (morphology studies).

3.1.1 Spectroscopy

Photoluminescence Spectroscopy. This technique looks at the relaxation optical transitions between electron states. Contrary to electroluminescence studies, where radiatively recombining carriers are supplied by electric current, photoluminescence presents a more flexible approach, as there is no need to think about electrically contacting the material or about its conductivity. A typical set-up for photoluminescence measurement is shown in Figure 35.

A Kimmon IK series helium-cadmium laser was used for both UV (325nm, 20mW) and visible (442nm, 80mW) excitations. The re-emitted light from the sample was focussed onto a $100\mu m$ entry slit of a single-grating ISA SPEX 270M spectrograph with both computer-controlled grating and slits. For detection, a Hamamatsu R2949 photomultiplier tube was used with 68mA/W (at maximum) cathode sensitivity, air-cooled down to -30°C with an Edinburgh Instruments cooler controller. 300-500V anode to cathode voltage was used. 1200 grooves/mm grating provides 1nm resolution, which was good enough for the photoluminescence measurement purposes. The wavelength range was limited by the response of the photomultiplier tube to 200-850nm. The short-wavelength end of the range was somewhat damped due to the absorption of UV light by the focussing lens. Motor controls and data recording were performed via Autoscan software. The data was output in ASCI format for further processing.

Raman Spectroscopy. The technique allows a study of the vibrational spectrum of the sample. Besides, and contrary to Infrared Spectroscopy (measuring the absorption of infrared radiation due to the vibrational resonances of molecular and lattice structures), Raman spectroscopy has the capability to detect vibrations with zero dipole momentum. When visible light is scattered from a solid sample at some non-zero angle, a phonon is produced or absorbed in a crystal to compensate for a change in photon momentum. When an acoustic phonon is participating in the scattering, the

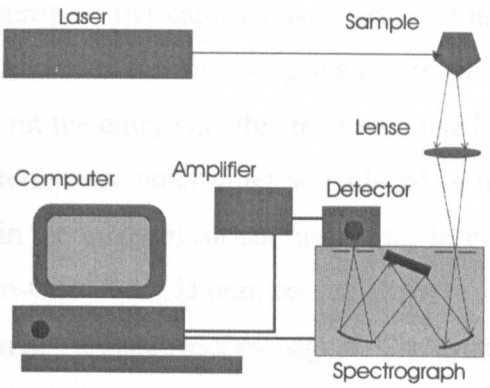

Figure 35. A set-up scheme for measurements of photoluminescence. The sample is optically excited with a cw-laser, re-emitted radiation is analysed by a computer controlled spectrograph.

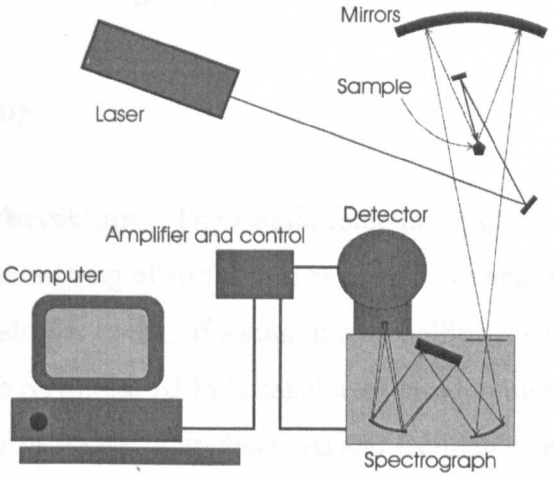

Figure 36. The scheme of the Raman set-up with back-scattering geometry, used in the current study.

process is called Brillouin scattering. Processes involving optical phonons [107], are referred to as Raman scattering. Along with momentum, phonons also carry some portion of energy away, or add some energy to the photon. When a laser source is used for illumination of the sample with a precisely known wavelength, it is possible to detect the change of the photon energy by means of spectroscopy. Thus, the information on the energy spectrum of phonons in the sample is provided.

In the Raman experiments reported below, an Innova 90 argon-ion laser was used, tuned to the 514 nm line. The beam was focussed on the sample, the beam spot being about 200μm in size. The scattered radiation was collected and focussed onto the entry slit of Jobin Yvon HR460 single grating spectrograph by means of a spherical mirror

(400mm radius of curvature). In our case it was important that the incident beam was not parallel to the optical axis of the focussing system as shown in Figure 36 so that the pump beam does not hit the entry slit: this reduces noise light near the entrance of the spectrograph. An interference notch-filter was placed immediately in-front of the entrance slit (not shown in the scheme) for cutting out the laser line. A spectraview 2D 500X320 pixels Spectrum-One^{TM} CCD unit, cooled down to 140K by liquid nitrogen, was used for the detection of the spectroscopic signal. The system is specially designed for Raman applications: it is not suitable for wide-range spectrum acquisitions (the grating has to be moved a lot of times to cover the whole range, with the final spectrum being "glued" from short 44nm intervals corresponding to the 25mm width of the CCD detector), but 1200 grooves/mm grating allows the resolution of 1.5 cm^{-1}.

3.1.2 Microscopy

Atomic Force Microscopy. The atomic force microscope (AFM) is a relatively new tool for nano-scale imaging of surfaces. The mechanics and the set-up of the image taking process is very similar to that of a scanning tunnelling microscope (STM). However, on the contrary to STM, the AFM is capable of measurements on non-conductive surfaces, which widens the range of applications and facilitates the use of the device. A schematic diagram of the microscope is shown in Figure 37.

The sample is placed on a stage, which moves in both horizontal directions allowing a scan over a square area. A very thin golden tip with a tungsten needle at its end is brought into contact with the surface of the sample (see the right insert in Figure 37). The force on the tip can be as small as 10^{-9} Newtons, when the repulsive mechanical force balances the attractive Van der Waals forces. The tip is scanned across the surface in a raster pattern. The deflection of the tip is monitored as the tip is scanned. In the device used in the current work the tip is stationary in its horizontal position, but deflects vertically following the roughness of the sample surface, when the piezo-mount is scanned. To monitor the deflection of the tip, a laser beam is used, which hits the top face of the tip and reflects onto the detector. For the detector to be specifically sensitive to the deflection of the beam, it is divided into two separate parts, one above the other (see the left insert in Figure 37). The electronics of the device measures the

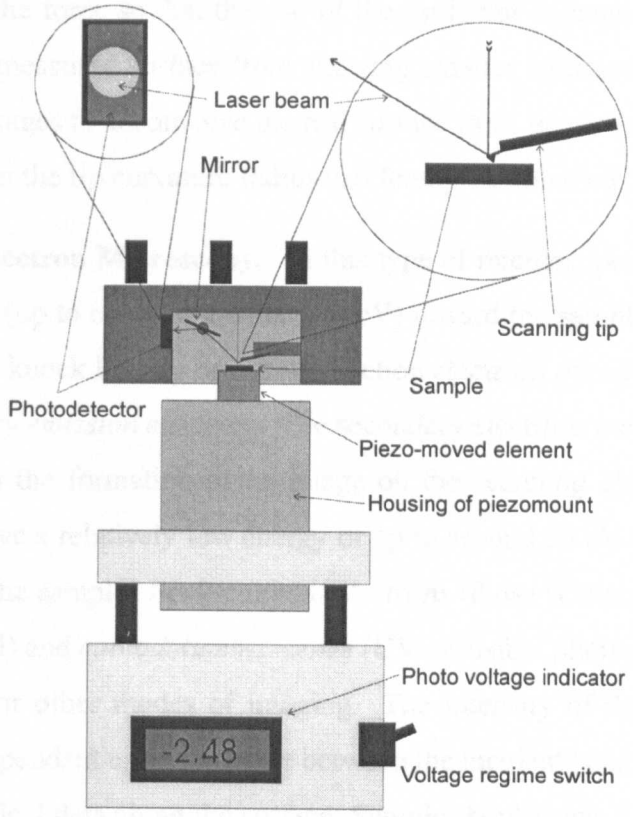

Figure 37. A schematic diagram of the atomic force microscope operation. The sample is scanned horisontally by the high-frequency voltage applied to the piezo-mount. The tip bends vertically following the roughness of the sample surface. The bending of the tip is detected via the deflection of the laser beam reflected from the top face of the tip.

difference in photocurrents in both parts of the detector, so that a zero reading of this difference corresponds to the exact positioning of the beam with equal intensities on both detectors. The deflection of the beam corresponding to each of the 400×400 horizontal scanning pixels is recorded by the software, and the surface of the scanned area is recreated on the screen of the computer. There are different sizes of piezo-mounts (called *Heads*), for different scan sizes and resolution requirements. The largest possible scan size available in our system was 150μm, while for atomic resolution imaging the smallest head was used, but the scan size is limited to 600nm in this case. The microscope is mounted on a vibration isolation support (not shown in the figure).

The end of the tip (the tungsten needle) has a shape of a pyramid with 90^0 angle. This makes it impossible to view the deep structures: all the vertical walls are shown with a 45^0 slope. Additionally, the very tip of the needle is never atomically sharp. The average radius of curvature is 5nm (unless a very good tip is in hand and special care

is taken to adjust the force so that the end of the tip is not damaged during the scan). This prevents the measured surface from showing smaller structures. However, there exist software packages to deconvolve the real surface from the measured result, so that structures finer than the tip curvature radius can finally be obtained on the image.

Scanning Electron Microscopy. In this type of microscope, a high voltage accelerates electrons (up to energies around 30KeV) toward the sample in vacuum. Incident electrons may knock loosely bound conduction electrons out of the sample. These are called *secondary emission electrons.* The secondary electrons are the electrons most commonly used in the formation of an image on the scanning electron microscope. These electrons have a relatively low energy of up to around 50 eV and originate from the first 10 nm of the sample. *Backscattered electrons* (those scattered by the nuclei of the sample material) and *cathodoluminescence* (UV or visible photons) are also present and can be used for other modes of imaging. The intensity of the secondary emission electrons is dependent upon the angle between the incident beam and the specimen yielding topographical data about the surface. Sample should have a good conductivity to drain the electric charge from the surface. Samples with no natural conductivity are usually covered with a thin (about 10nm) layer of gold, and the surface of the sample is contacted to the metal stage with a special conductive glue.

The detector fitted to the instrument is a phosphor screen coupled via a light guide to a photomultiplier tube. Electrons emerging from the surface of the sample are accelerated by an applied bias of up to 400 Volts towards the detector. As the accelerated electrons hit the phosphor screen, photons are emitted which subsequently undergo amplification by the photomultiplier. These photons are then mapped to the location of the electron beam as it is scanned by the software.

The scanning procedure and all the parameters are fully computer controlled. By relating the photocurrent to the instant position of the focus of the incident electron beam, the image of the scanned surface is reconstructed. A resolution of about 5-10 nm is achievable for good samples (those with sufficient conductivity and sharp features). This limit is imposed by the finite depth from which the backscattered secondary electrons originate, the depth uncertainty leading to the lateral smearing of the image.

3.2 Mechanism of Porous silicon formation

3.2.1 Anodisation mechanism

To give an idea of the complexity of the problem raised by porous silicon formation, Table 4 (page 86) summarises the major proposed models for both pore initiation and propagation mechanisms. None of the listed factors can account for all observations. This confirms that a combination of several effects such as the electrochemical mechanism (chemistry, kinetics, front instability, hole transport, potential distribution) as well as mechanical effects, are at the roots of porous silicon formation.

For the following discussion of electroless (chemical) etching of silicon the ideas of hole diffusion [119] and quantum confinement [120] are important. Initially, and during the reaction, the silicon surface is passivated by hydrogen. For our purposes, the process of detachment of one Si atom can be expressed by the following simplified equation:

$$\begin{aligned} \mathrm{Si}_n\, H_2 + 4F^- + 2H^+ + 2\,(hole)^+ \;&\rightarrow \\ &\rightarrow\; \mathrm{Si}_{n-1} + \mathrm{Si}\,F_4 + H^2\uparrow \end{aligned} \tag{3.37}$$

Only those surface hydrogen atoms participating in the reaction are shown. Detachment of a Si atom becomes possible after the passivating hydrogen ions on silicon surface are substituted with fluoride ions, as shown in Figure 38. After such a substitution the electron density around the attacked Si atom is shifted toward the solution, which makes a complete detachment possible. Free dangling silicon bonds on the fresh surface are readily caught by protons taken from the solution, and the surface is hydrogen-passivated again.

The first stage of the reaction, which is the substitution of fluoride ions for protons, requires two holes supplied to the surface for each silicon atom detached. In the anodisation process, holes are supplied by the electric current through the wafer. That is why only one side of the wafer is etched, depending on the direction of electric current (Figure 38, top). Thus, supply of holes from the bulk of the crystal to the interface with the solution plays a crucial role in the etching process. Furthermore, it was noted, that a porous structure only forms for anodisation currents below a certain value, while for higher currents electropolishing takes place [121]. This observation is consistent with

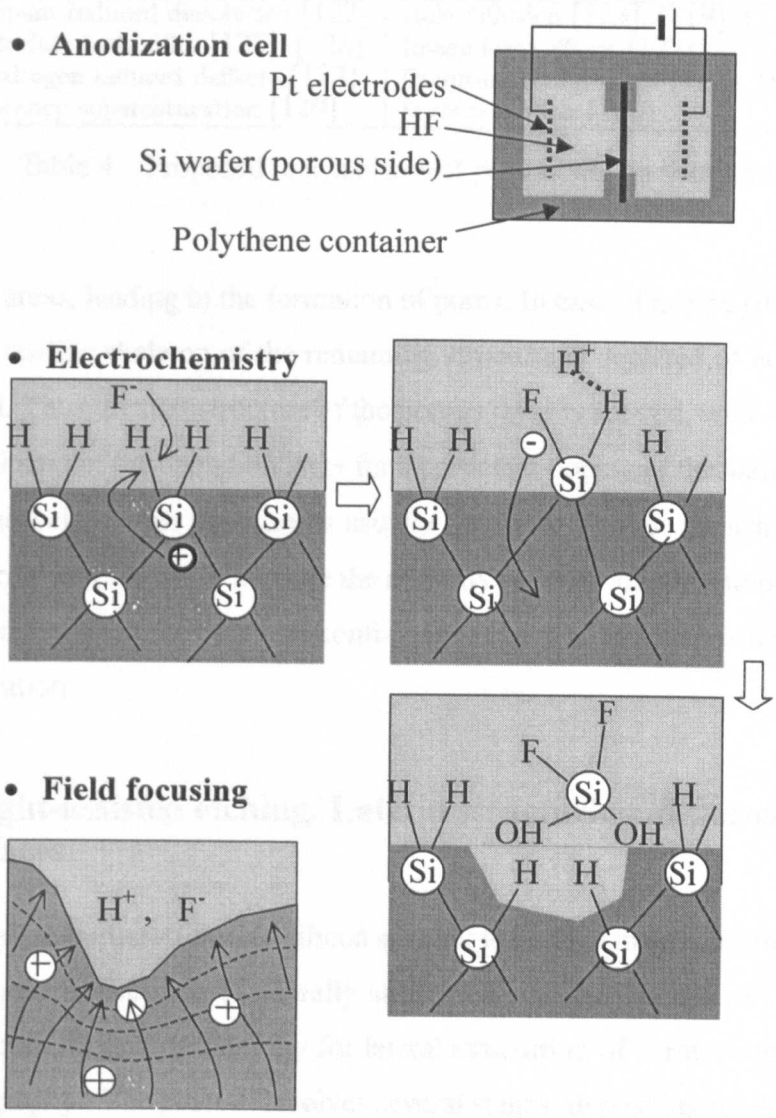

Figure 38. Porous silicon preparation by anodisation: process technique and the mechanism of pore formation. See text for details.

the proposed explanation, that for low current, the reaction rate is limited by hole supply from the bulk, rather than by fluoride ion (F^-) supply from the solution. The top layer of silicon near the interface with the solution is depleted of majority carriers, that is why the layer may be considered as a dielectric, while the solution is conductive. The equipotentials follow the roughness of the surface and the electric field is focused toward the convex areas of the solution volume. The holes are supplied more effectively to the pits on the interface due to the focusing of electric field inside the depletion region (Figure 38, bottom-left). This increases the rate of etching near pits and decreases

Pore initiation	Pore propagation
Dopant induced dissolution [122]	Hole diffusion [123], [119], [124]
Interface instability [125], [126]	Image force effects [127]
Hydrogen induced deffects [128]	Quantum confinement [120], [8]
Vacancy supersaturation [129]	Surface tention [130]

Table 4. Proposed mechanisms of porous silicon formation

it in all other areas, leading to the formation of pores. In case of n-type silicon, as pores grow, the crystalline skeleton of the remaining structure is depleted of holes and is no longer etched. Thus, a microstructure of the porous layer is created, with wall thickness twice the thickness of the depletion layer for a particular doping of the wafer. For p-type silicon, a nanoscale porous structure is usually reported. The mechanism of etch-stop effect is different here: holes, which are the majority carriers, are only stopped from acting in the reaction when the quantum confinement effect of bandgap widening reduces hole concentration.

3.2.2 Light-assisted etching. Lateral structuring of porous silicon surfaces

If optical properties of porous silicon are ever to be used in optoelectronics, a technique of one-step preparation of laterally structured porous silicon layers would be of great use. A conventional technology for lateral structuring of surfaces and thin layers is mask lithography . The process involves several stages: depositing masking material, depositing photoresist, UV exposure through the optical mask, developing photoresist (removing exposed areas), structuring the masking material, and finally, structuring of the layer itself through the prepared mask. In the anodisation process, however, it is very difficult to define areas of preferential etching by masking, as there is no masking material available which is well resistant to HF. Experiments with anodisation through masks have been reported in [131], where submicron resolution has been demonstrated. The mask's life-time, however, was shown to be just seconds for the silicon oxide mask and minutes for silicon nitride. Undercutting effect presents another difficulty, limiting further the possible achievable depth of the porous islands. Besides, anodisation itself is a process difficult to incorporate into conventional CMOS technology. Because etching only occurs when holes are supplied to the silicon-to-solution interface, some way to supply holes other than by electric current should be used for electroless etch-

3.3 Structured illumination for preparation of laterally structured porous silicon layers

3.3.1 Physics of the process

Considering the electolyte as a perfect conductor, the interface of the wafer may be treated as a contact of metal with semiconductor. The corresponding bending of the energy bands in semiconductor near the interface, known as *Schottky barrier* [21], is shown in Figure 39.

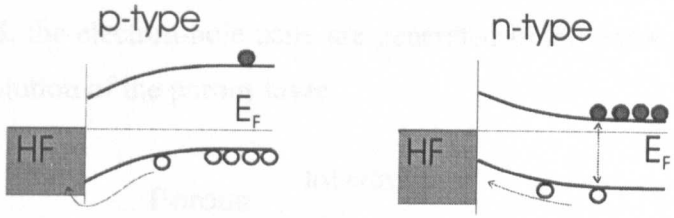

Figure 39. Schottky barriers at the interface between a semiconductor and Hydrofluoric acid solution for different types of doping. Schematic energy bands in real space are shown.

In the case of p-type silicon, there are plenty of holes available, but the of the interface creates a hole-depleted region on the surface (see Figure 39, left), so that the only mechanism of hole supply to the interface is tunnelling through the barrier. That is why p-type silicon is not normally etched in a HF:water solution without electric current even under illumination. With n-type silicon, on the contrary (Figure 39, right), the Schottky barrier arising at the interface has a slope making it preferable for holes to diffuse to the surface, while there are not a lot of holes (minority carriers) available in the bulk. This makes the presence of illumination very effective in stimulating the etching process. An attempt is reported here of the use of this property of n-type silicon etching for developing a technique of one-step preparation of 2D laterally structured porous layers on silicon.

The effect of illumination on the process of stain etching was originally discussed in [133], where 633nm laser light was focused to submillimeter area on the surface of the wafer in the HF-based etching solution to produce porous regions exactly where illumination was present. Besides, it was noticed, that only red light (633nm light from

He-Ne laser was used) stimulated the growth of the porous layer. When green or blue light was used for illumination, no porous layer was formed. The authors found the results to be in agreement with quantum confinement, based on the following argument. Considering the blue shift of the absorption edge in the porous layer, its energy gap will be larger than that of the single-crystalline silicon as schematically shown in Figure 40. When the photon energy of the incident light is smaller than the energy gap of the porous layer, the porous layer is transparent and the electron-hole pairs are generated in the single-crystalline silicon near the interface of the porous layer. This will give the efficient transfer of the generated holes to the interface for the pore formation. When the photon energy of the incident light is larger than the energy gap of the porous layer, on the other hand, the electron-hole pairs are generated in the porous layer. This will result in the dissolution of the porous layer.

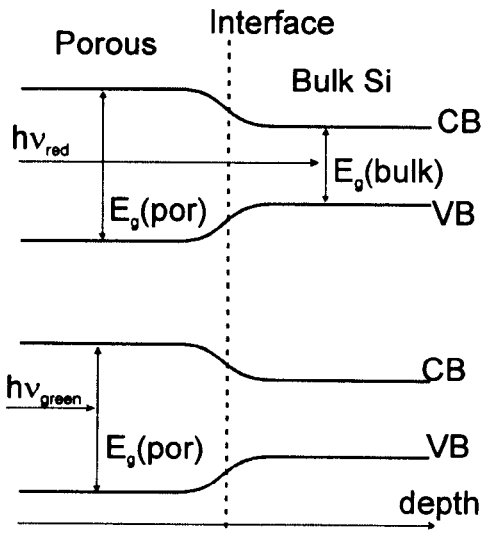

Figure 40. Schematic quantum confinement model of red-light-assisted porous Si layer formation (top) and of porous layer dissolution with green light (bottom), taken from the original work (reference in text).

Although correct, this explanation misses out an important point. According to this model, based solely on the quantum-confinement-induced broadening of the bandgap $E_b\,(bulk) \rightarrow E_b\,(por)$ as shown in Figure 40, the full dissolution of the porous layer would not happen when higher energy light quanta are used to generate the required carriers (holes). If green light is used, the etching of nanostructures would go further to produce smaller structures. Then, the bandgap $E_b\,(por)$ would become even

wider, and the formed porous layer would become transparent for green light as well, which would stop further dissolution. We would, thus, end up with a layer of finer nanostructures (with, probably, further blue-shifted photoluminescence!). The experimental result is that this does not happen. It can, therefore, be concluded that another etch-stop mechanism is involved, which works for the red light, but fails for more energetic light quanta. One of the possibilities is that when the structure gets sufficiently thin, the electrons (the "leftovers" of the photogenerated pairs after the holes were used in the etching process) are trapped inside nanostructures charging the top layer negatively, and this can prevent further dissolution. The effect could be due to the repulsive force on the negative fluoride ions, or due to the fast *Auger recombination* of new photogenerated pairs (when the energy is consumed by the electron escaping the nanocluster). The green (or blue) light, when used for photogeneration of new electron-hole pairs, could possibly provide the extra energy for the "old" electrons to escape from the nanoparticle, thus unblocking the nanoparticle. The final answer to this question requires further studies of the mechanisms of stain (chemical or electroless) preparation of porous silicon.

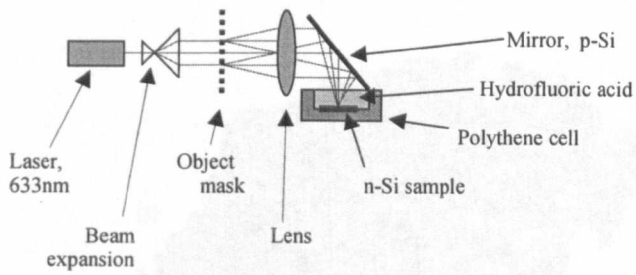

Figure 41. Set-up scheme of preparation of structured porous silicon layers.

The scheme of the experiment set-up is shown in Figure 41. An image of the copper mask with the desired structure is focused onto the silicon wafer in HF solution. The light enters the solution through the open liquid-to-air interface. Only the illuminated areas are etched to produce a porous structure corresponding to the image projected. 10 Ωcm n-type Si(111) wafers were used in our work. Experiments with (100) wafers

showed no difference from the (111) wafers in the morphology of the mesoporous structure.

3.3.2 Properties of light assisted HF etching of silicon

A typical AFM (atomic force microscope) image of the porous surface produced with red light assisted etching is shown in Figure 42. The resulting porous layer is mesoporous, with fine structure (<50nm) superimposed on the submicron roughness of the surface. The AFM tip has a blunt angle shape, which is why the image does not show the depth of the pores or any smaller structures inside. The smallest features on the image appear to be about 50nm in size, which could correspond to features less then 10nm, if one takes into consideration the shape of the end of the AFM tungsten tip (The deconvolution software referred to in the end of AFM operation description was not used in our version of a microscope). To explain the visible luminescence of porous silicon, quantum confinement models require a feature size on a scale of less then 10nm (usually 2-3 nm sizes are quoted, see the sections 2.2 and 2.6.1), which can not be seen on the presented image.

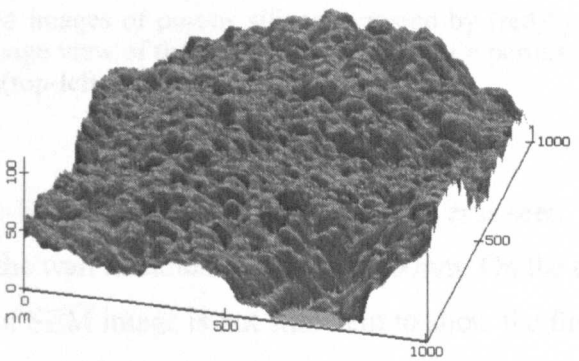

Figure 42. AFM image of the surface of porous silicon, prepared by light-assisted (633nm laser wavelength) chemical etching.

To give a better idea of the large-scale roughness of the porous layers prepared by this technique, an SEM (scanning electron microscope) image is shown in Figure 43. The top and edge views of the same sample are presented. Contrary to the AFM

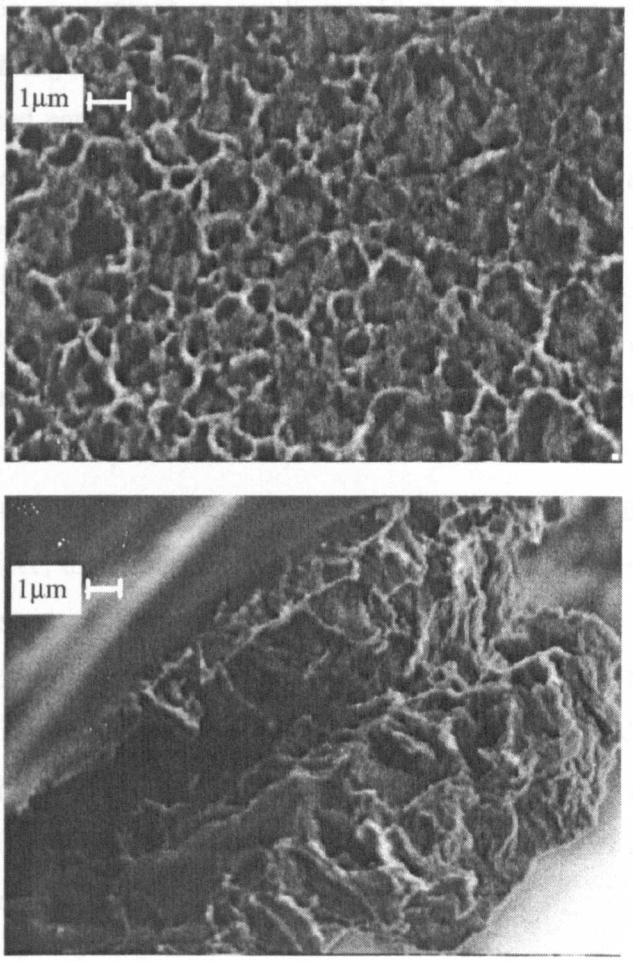

Figure 43. SEM images of porous silicon prepared by (red)light-assisted etching. Lower picture shows an edge view of the same sample, the brittle porous layer is seen detached from the bulk substrate (top-left area).

images, a sponge-like morphology of the porous layer is seen, with the pore diameter of about 1μm, and the wall thickness below 100-200nm. On the other hand, the resolution (magnification) of SEM image is not sufficient to show the fine nano-scale structure of the porous layer, seen in Fig. 42. The porous layer is clearly defined from the bulk substrate and its thickness is comparable to the photon absorption length (3-5μm for the He-Ne laser light). It is worth noting that there is no variation of the morphology with depth, usual for anodised n-type samples, when a thin nanoporous top layer covers a thicker macroporous structure[11].

To estimate the thickness of the barrier at the interface of n-type silicon and the electrolyte, consider the contact between the wafer and the solution as a Schottky barrier

[11] Example of such a structure is shown later in Figure 61 in the the section 3.4.

in a simple depletion approximation (see Figure 14, page 33), when a layer of thickness x_0 fully depleted of majority carriers provides the potential barrier U_0. Using the equation (2.15) developed earlier, the thickness of the depleted region can be estimated[12]. For our samples with U_0~0.5eV and N_D~5*10^{20} m^{-3}, this gives a barrier thickness around 1μm. Consequently, the holes are less likely to enter the wall between pores when its thickness becomes less then 1μm and this decreases the etching of thin walls. This argument is always used to explain the macroporous structure of anodised n-type silicon, see for example [123] or [136]. The sponge-like microstructure seen in Figure 43 is, probably, explained by this hole-depletion effect in the walls of the structure. On the other hand, in our samples, the walls are porous with a fine sub-structure. It can be supposed, therefore, that another mechanism, related to the quantum confinement of carriers [120], is also involved.

The first stage of this research was to study the properties of light assisted HF etching of silicon. The dependence of photoluminescence, the morphological structure and the rate of etching on parameters such as HF concentration, intensity and wavelength of the illumination and the doping level of the silicon wafer have been studied. The results are summarised below.

Illumination wavelength. In the experiments reported here, 1mW Helium-Neon laser (633nm) was used for red illumination, whereas more intense (5-20mW) Ar-ion laser was used for green (514nm) and blue (488nm) illumination.

In accordance with the original work [133] only illumination with red light during etching of n-type silicon produced a porous structure, whereas blue and green light causes the porous structure to dissolve. It is demonstrated by Figure 44, showing the AFM image of a HF treated wafer, when green light from an Ar-ion laser was used for illumination. The absence of the porous phase is clearly seen, the wafer being flat with only pits etched out where the illumination was present (dark areas). The effect is not completely understood. More research is required to explain the physical nature of the different etching regimes for different wavelengths. Some speculations were offered in the beginning of this section (p.89).

[12] In reference [135] this formula is expressed for Gauss system of units: 2π in denominator there corresponds to $2\varepsilon_0$ in the nominator of (2.15). Additionally the dielectric constant ε of silicon was not accounted for, which was author's mistake. Consequently, the following speculations in [135] are not quite correct.

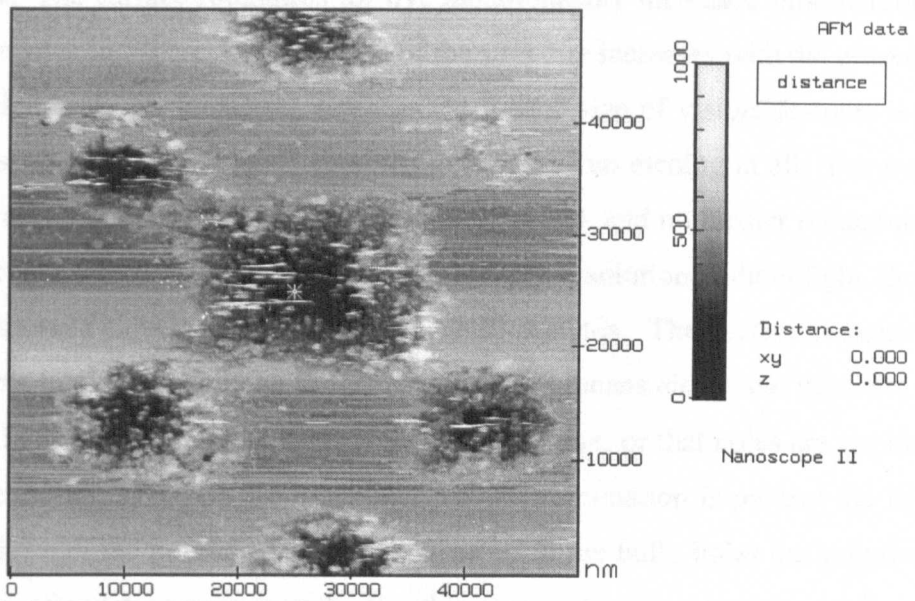

Figure 44. AFM image of the surface of silicon, processed in HF with structured green (514nm) illumination. Empty pits rather than porous structures were formed. (Thin horizontal lines on the image are noise rather than surface roughness.)

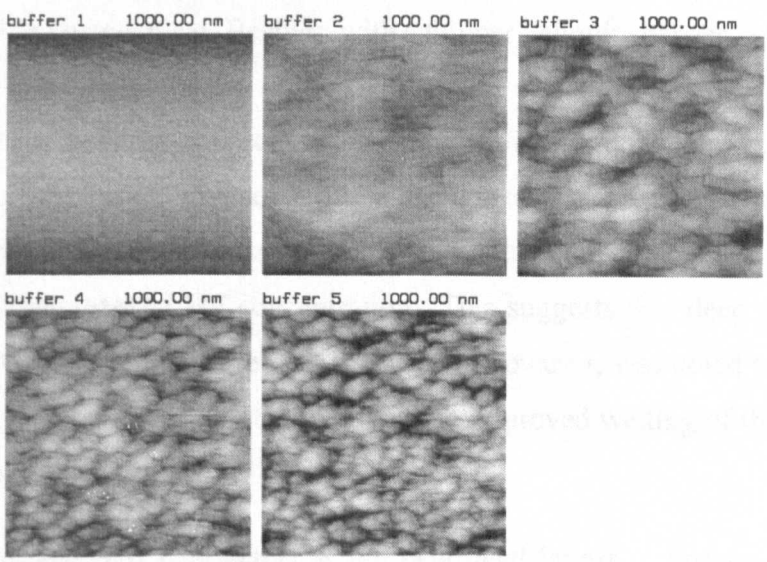

Figure 45. Surface roughness for monotonically increased illumination densities from 0.1 mW/mm^2 (top left) to 10 mW/mm^2 (bottom middle).

Illumination power effects. The illumination power seems to be of crucial importance. The surface roughness for five monotonically increased illumination densities are shown in Figure 45. The depth of the structure increases with the power density (controlled by beam focusing), whereas the typical size of visible features is similar. With less then 0.1 $mW*mm^{-2}$ (first image) there is no etching at all. For more then $10mW*mm^{-2}$ intensity, the resulting image saturates, and no further reduction of feature size is detected. When etched samples are left in solution without light, the porous layer dissolves slowly, over a period of 10-20 minutes. The surface remains microrough, but luminescence is no longer present. This means either that there are enough carriers in porous skeleton to destroy the nanostructure, or that holes are not needed to slowly etch the layer. On the other hand, when illumination is present the light penetrates through the porous layer and is absorbed in the bulk, holes are supplied to the pore tips, stimulating pore growth. For this process to compete successfully with the dissolution of the porous layer, the power density has to exceed a certain limit, in good agreement with the above result.

Ethanol content and wafer resistivity. Samples with less resistivity (more doping) give just a rough surface rather than nanoporous layer. Excessive concentration of free electrons (majority carriers) makes it difficult for the holes to play their assumed role in the etching mechanism. Besides, with a thinner Schottky barrier, holes are driven to the surface less efficiently.

Ethanol content does not seem to have much influence on the process. In contrast to anodisation, where the presence of 50% ethanol is essential to reduce surface tension and let the etchant into deep pores, in our experiment it only slows down the process because of the decrease in HF concentration. This suggests that deep thin pores are not formed. A small fraction of ethanol (10-25%), however, was noted to improve the reproducibility of the results, probably due to the improved wetting of the wafer when put into the etching solution.

Photoluminescent properties of the produced layers. Porous silicon layers prepared by red-light-assisted chemical (electoless) etching have visible orange photoluminescence. Results of measurements with UV (325nm) and blue (442nm) excitation wavelengths are shown in Figure 46. The PL has a wide Gaussian shape which is conventionally explained by the size-distribution of quantum-size features. The curves ob-

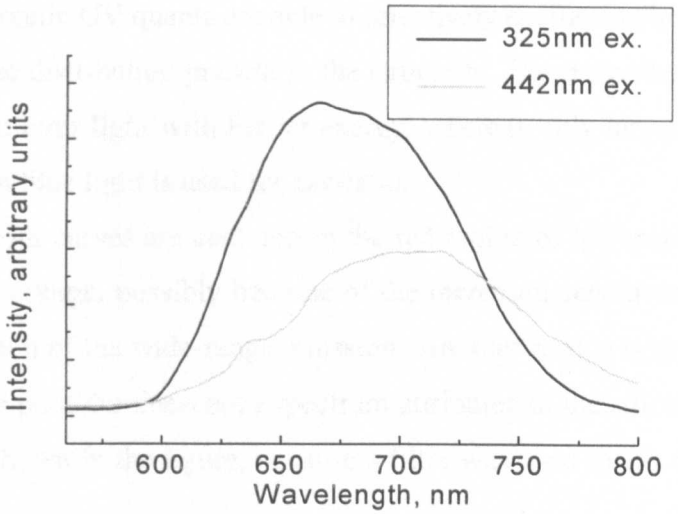

Figure 46. Photoluminescence of porous silicon prepared by red-laser-assisted chemical etching. Results are shown for two different excitation wavelengths.

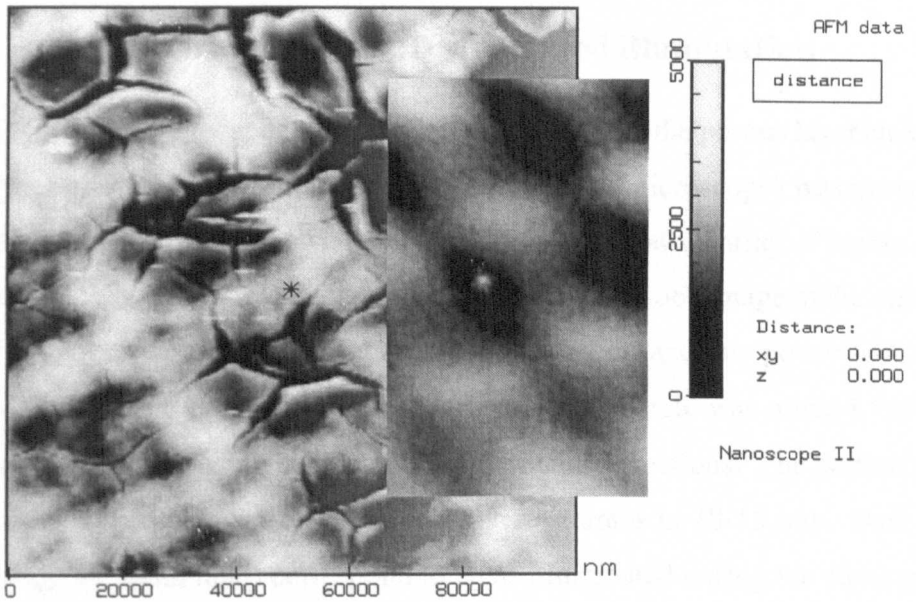

Figure 47. AFM image of a 2D structured porous silicon layer. Dark areas correspond to deeper porous regions. The insert shows the underlying bulk silcon surface, revealed after the porous layer was removed by KOH solution.

ing to be possible. This may be achieved either chemically, by introducing other strong oxidants in-to the HF:water solution [132], or by means of photogeneration of electron-hole pairs [133]. The idea of the experiment described below was to use a structured illumination to specifically produce porous areas only in regions illuminated during the etching in HF. The results presented in the next section have been published in [134] and [135].

tained for these two excitation wavelengths are 30-40 nm shifted from each other. The explanation of this difference in the central wavelengths of the PL curves is probably that the more energetic UV quanta are able to selectively excite smaller nanocrystallites from the wide size distribution present in the structure. These smaller nanocrystallites are more likely to emit light with higher energy, whereas only larger nanocrystallites are involved when blue light is used for excitation.

Although both curves are centered in the red region of the spectrum, the visible light seems to be orange, possibly because of the increased sensitivity of human eyes to the green fraction of the wide-range emission. Another reason is that there is a blue component on the photoluminescence spectrum attributed to the silicon-oxide layer on the surface (not shown in the figure, because a filter was used to cut off the excitation light).

The graphs in Figure 46 are not normalised, the laser power was five times higher for blue (442nm) than for UV (325nm) excitation. That is why the right-hand wing of the graph corresponding to blue excitation is not within the envelope of the UV excitation graph. All other conditions (filters, slit widths, pixel integration times) were the same in both cases.

3.3.3 First experiment with 2D structured illumination

For the first attempt at defining the lateral structure of the porous layer an image of a 2D copper grid (the sort used in transmission electron microscopy) was projected on the wafer during etching, as shown in Figure 41. A 20μm spaced array of porous regions was produced. Fig. 47 shows a typical atomic force microscope image of the sample. 50 wt% HF solution, with a small amount of added ethanol, and low power 633nm laser light were used. The estimated power density on the sample was around 5mW/mm^2 taking into account focusing geometry and interfacial reflections. The pattern appears in 2-5 min and the thickness of the porous layer saturates in 10-15 min. Dark porous regions (Fig. 47, main field) correspond to areas illuminated during the etching. Large scale cracks could be avoided by using a proper drying technique ([137], [138], [139]). The cracks do not appear with shorter etching time but the thickness of the porous layer decreases. To study the interface profile between porous and bulk phases the porous layer was removed with weak KOH solution. This revealed the underlying surface of

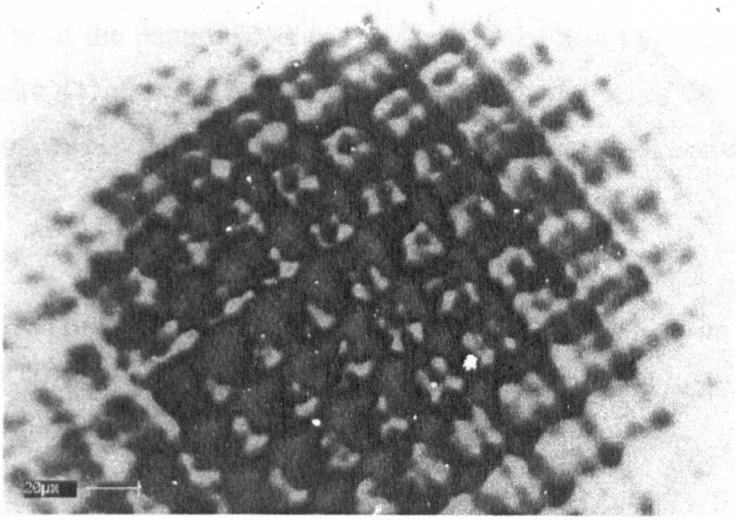

Figure 48. SEM image of the 2D rectangular array of porous areas on silicon, produced by structured-light-assisted etching.

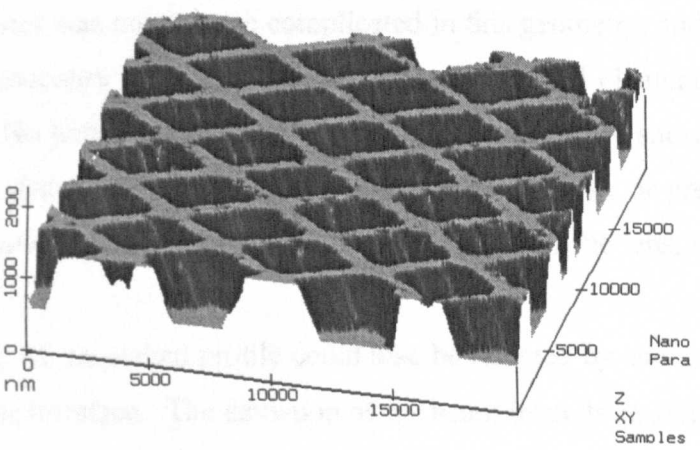

Figure 49. Image of 100μm copper grid, recorded in negative photoresist with 20-times reduction in sized (viewed with AFM).

bulk silicon with the same 2D periodicity and sinusoidal depth profile (Fig. 47, insert). For comparison, the SEM image of a similar sample is shown in Figure 48. The quality of image is low due to the low conductivity of the porous layer.

The quality of the pattern produced is close to the best possible for the present set-up (see Figure 41) if one considers the spherical aberration of the lens used. The longitudinal misfocus Δl of the light entering a plano-convex lens at a distance h from the axis can be expressed as:

$$\Delta l = -\frac{(n-1)\,h^2}{2R}$$

where R is the radius of curvature and n is the refractive index of the lens. To get a rectangular rather then sinusoidal pattern, higher order spatial Fourier harmonics are required to act in image formation. For the lens used, a 5mm aperture h was needed to use one central and four side components of the Fourier grating image, which gave 5μm aberrational feature broadening on the image. Calcium fluoride (CaF_2) components introduced into optical scheme would allow a short-focus objective to be positioned close to the wafer, which would improve the quality of the image.

The experiment with CaF_2 side window has actually been tried as the next stage of this research, with illumination entering the etching cell horizontally and the wafer positioned vertically. CaF_2 has proven to be a suitable material for optical elements in an HF environment. It was possible to place an objective lens from the optical microscope immediately near the CaF_2 window for the image projection. Unfortunately, the process of focus adjustment was much more complicated in this geometry, and the duration of the alignment procedure was increased, so that other optical elements were affected with HF vapor. No better results have been produced than those shown in Figures 47 and 48. A short-focus optical objective lens made from CaF_2 , or precise mechanics for the exact positioning of the sample in the focus plane of the lens, would solve this problem.

The quality of the etched profile could also be affected by acoustic vibrations of the solution-to-air interface . The deviation of the beam from its equilibrium position γ due to an angular perturbation of the surface α is:

$$\gamma = \alpha\frac{n-1}{n}$$

where n is the refractivity of the solution. For the 5mm distance to the sample in the solution, this gives 5μm loss in the accuracy of the image for $3*10^{-3}$ radian angular am-

plitude of surface perturbation. This is easily avoided if a CaF_2 side window discussed above, rather than the air-to-liquid interface, is used for beam entry.

The distortion of the image projected to the bulk silicon caused by the light scattering in the porous layer is unlikely to be comparable with the other effects mentioned. For a rough estimation we can refer to the Mie formulae [140]. With a typical wall thickness 100nm used for calculation of the size parameter, more than a half of all light is scattered for angles less than 20 degrees. Although our structure can hardly be considered as round spheres, this suggests a negligible distortion of the image when the depth of the porous layer is less than the lateral feature size.

To demonstrate that optical limitations of the technique allow further reduction of sizes, the image of the same grid with four times smaller features recorded in negative photoresist is shown in Figure 49. The period of the image is around 4-5μm, and the thickness of the walls is just 1μm. The empty square areas of this structure are those where illumination was present.

3.3.4 Interference techniques for structured illumination patterns with submicron resolution

An alternative way of providing 2D structured illumination for preparation of laterally structured porous silicon is possible with the use of interference. This approach was successfully demonstrated in [141], where an optical interference pattern was used to selectively dissolve parallel lined areas on the previously prepared porous silicon layer. Diffraction gratings on silicon have been made by this technique. 2D arrays have also been demonstrated, when the process of photo-dissolution was interrupted half-way through, and the sample was rotated 90 degrees. The same technique of illumination with an interference pattern can be used for light-assisted etching of bulk n-type silicon, with the difference that, for a 2D array to be produced, the whole structured illumination pattern should be present simultaneously. This is because of the competition of porous layer growth in illuminated areas with its dissolution in dark areas, as discussed above. A 2D interference pattern can be created either by using two independent pairs of interfering beams, or by using multiple reflections of parts of the same beam. The schemes of both geometries are discussed below. To study the opti-

cal limitations of the interferential approach for one-step 2D-structured porous silicon preparation, photoreccording in negative photoresists was used.

To compare the results obtained with theoretical expectations, and to model the optical field in more complex cases (which are difficult to realise experimentally), a computer simulation program was created. Given all the wavevectors and polarisations of incoming beams, the electric field amplitudes are calculated in every point of the image plane of a given size as a vector sum of all the component fields. A 3D graph of the intensity distribution is then plotted as an output. Formulas and the algorithm used in the program are outlined in Appendix B.

Interference pattern of two perpendicular pairs of beams. To produce a 2D rectangular array of illuminated areas with submicron resolution, the pattern created by two perpendicular standing laser waves can be used. The optical scheme used for this purpose is shown in Figure 50. The laser beam is spatially filtered on a pinhole to a Gaussian single mode and expanded to 1cm diameter (the corresponding optical elements are not shown). Perpendicular beams were produced with a prism beam splitter, with 60:40 intensity ratio. The beams are then directed into a mirror cube, where each beam is sent back to create the interfering counter-waves. Each beam is polarised horizontally, so that the polarisations of pairs are perpendicular to each-other, which allows both 1D interference patterns to form independently, the total intensity being recorded. After passing through polarisers, the relative intensities of the beams could be equalised by means of neutral density filters. The sample (a glass plate with a layer of high resolution photoresist) is placed immediately near the mirrors of the cube. Using 442nm wavelength laser light used, the distance between the intensity maxima of a standing wave formed by counter-propagating beams would be exactly 221nm. The calculated distribution of intensity in the plane of beams is shown in Figure 51. The cube is slightly tilted (for about 25 degrees) so that the counter-beams are not strictly opposite to the incoming beams, which creates a wavevector component perpendicular to the photographic film as it is necessary for photoreccording, see Figure 52.

An AFM image of the actually recorded 2D interference pattern with the set-up discussed is shown in Figure 53. The structure has approximately 250nm feature-size, which is slightly larger than a half-wavelength size due to the tilt of the mirror cube required for a sufficient normal component of the light propagation vector.

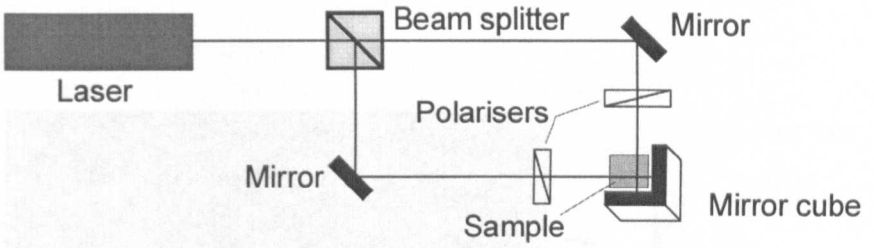

Figure 50. Schematic set-up for photorecording of the 2D optical interference pattern.

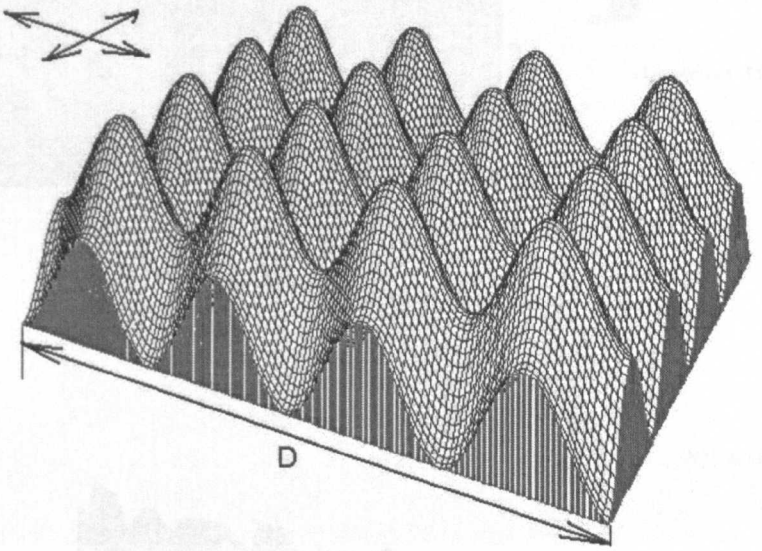

Figure 51. Intensity pattern expected from interference of two perpendicular pairs of counterpropagating coherent beams. Directions of light beams are shown in the top-left corner. Polarisations of both pairs are horizontal and perpendicular to each-other. Distance D corresponds to two wavelengths.

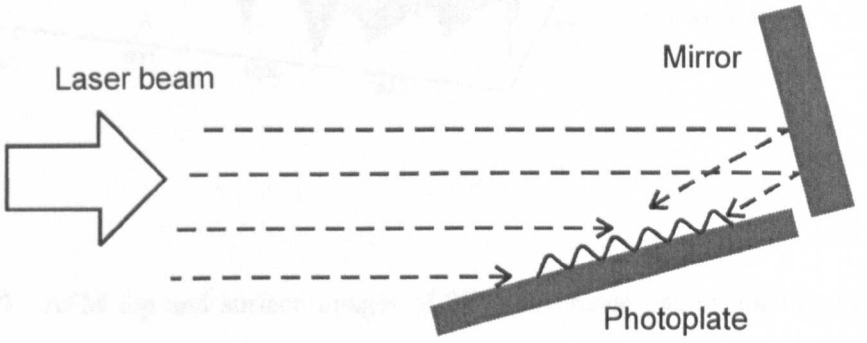

Figure 52. Sample and mirror-cube tilt used in the experiment with photorecording of interference pattern.

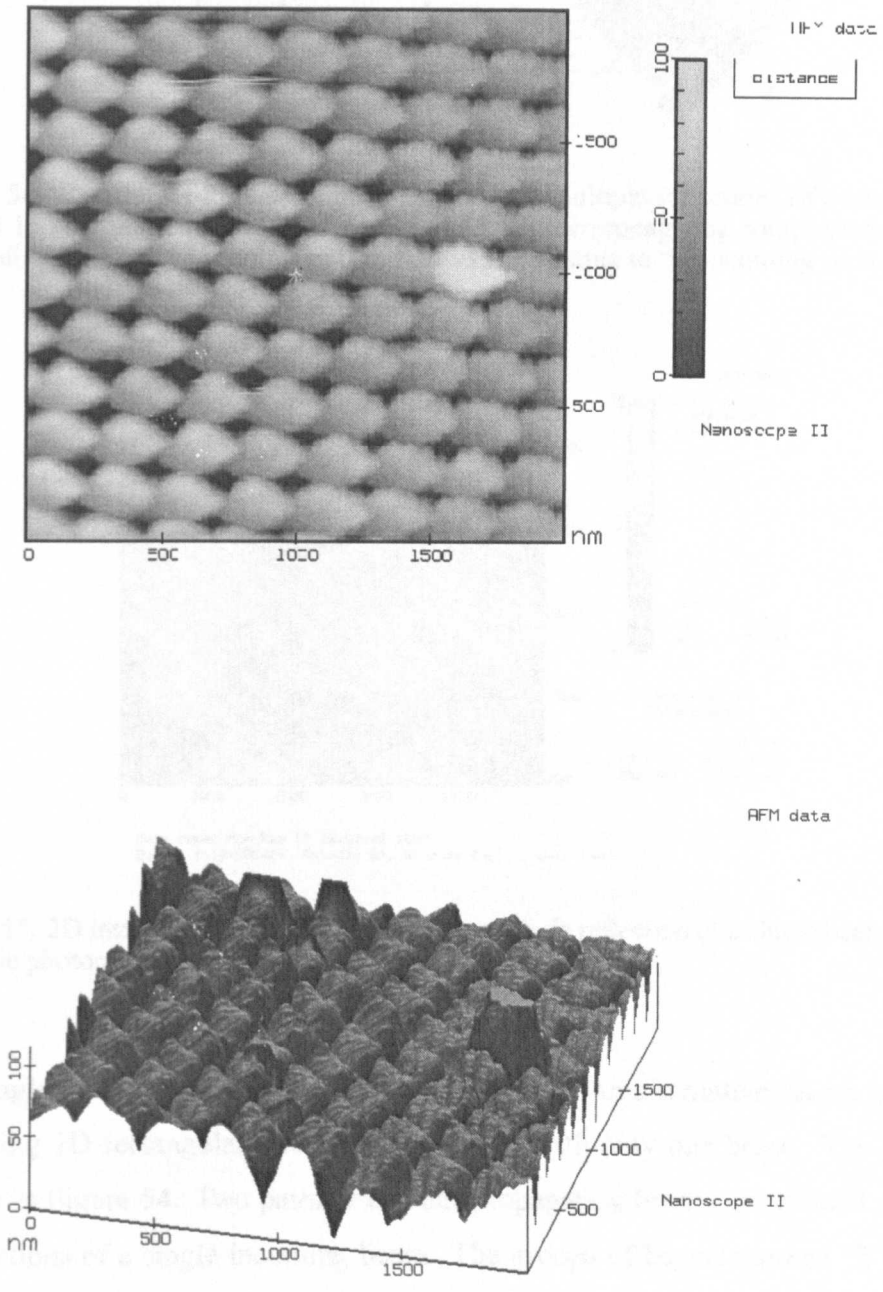

Figure 53. AFM top and surface images of 2D interference pattern recorded in negative photoresist.

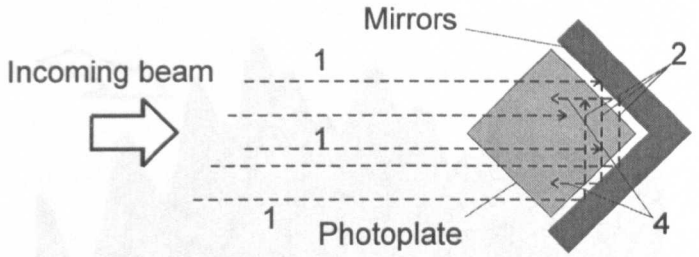

Figure 54. Creation of 2D interference pattern with multiple reflections of a single incoming beam 1. The first reflection produces mutually counterpropagating components 2, and the second reflection produces components 4, counterpropagating to the incoming wave 1.

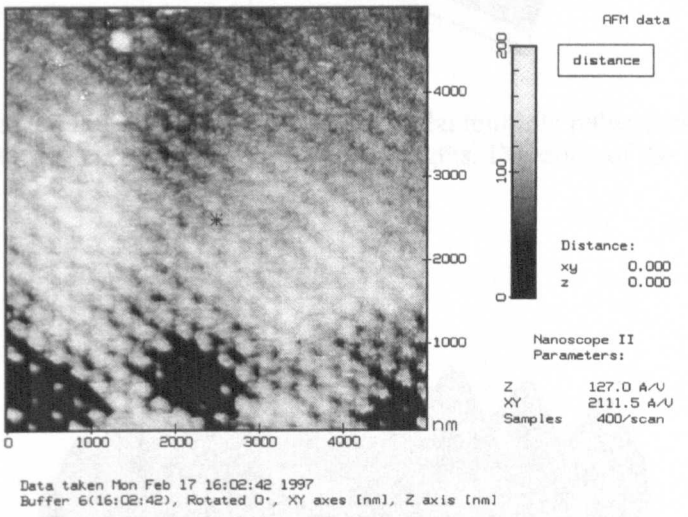

Figure 55. 2D interference pattern produced by multiple reflection of a single beam, recorded in negative photoresist (AFM image).

Single-beam geometry for 2D interference. An alternative set-up is possible for creating 2D rectangular interference patterns with only one beam. The geometry is shown in Figure 54. Two pairs of counter-propagating beams are created via multiple reflections of a single incoming beam. The groups of beams marked "2" (and not marked group "3" counter-propagating to "2") is produced after the first reflection, and the group "4", counter-propagating to the initial beam "1" is produced after the second reflection. An example of an interference pattern created by this technique and recorded in photoresist is shown in Figure 55. The optical scheme and the alignment procedure is easier in this case than with two perpendicular beams (scheme in Figure 50 and image in Figure 53), but the quality of the recorded image is much worse, due to the partial

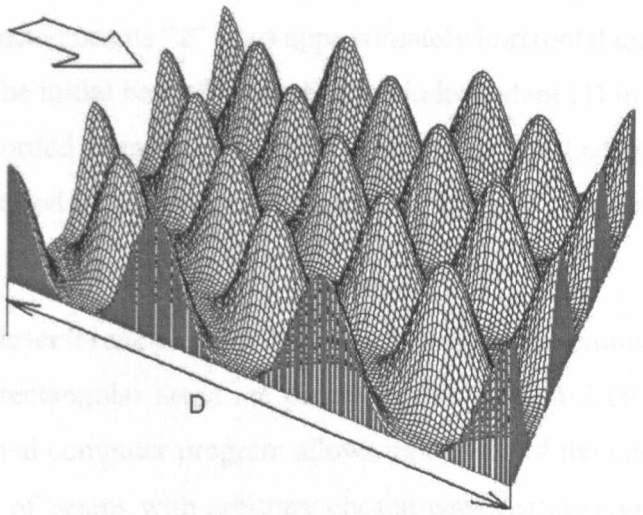

Figure 56. Calculated interference pattern produced bu multiple reflections of vertically polarised beam. Distance D corresponds to three wavelengths. Direction of the incoming beam is shown.

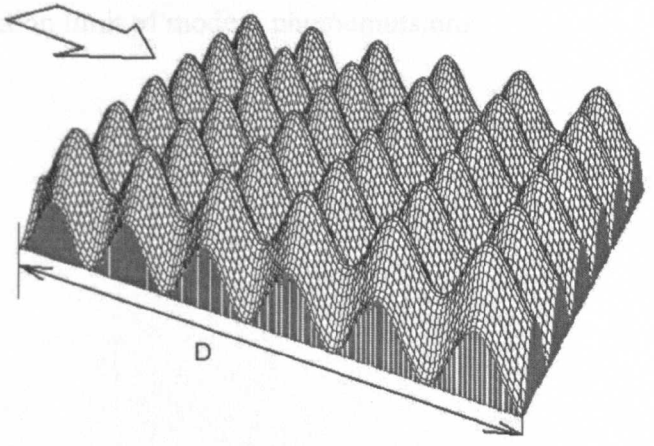

Figure 57. Calculated interference pattern produced bu multiple reflections of horizontally polarised beam. Distance D corresponds to three wavelengths.

loss of plane polarisation of the field components after the reflections (The polarisations would remain plane if the mirror cube was not tilted).

The created patterns are different for vertical and horizontal polarizations of the incoming beam. Disregarding the effect of mirror tilt (the polarisation actually changes to elliptical after the reflection), for a beam polarised vertically (perpendicularly to the plane of Figure 54), all the reflections have the same polarisation: the field amplitudes of all the reflections rather than intensities are added. The calculated pattern is shown in

Figure 56. In the case of a beam polarised horizontally (in the plane of the figure), the polarisation of reflected beams "2" stays approximately horizontal and perpendicular to the polarisaton of the initial beam "1", so that two independent 1D interference patterns are formed, the recorded intensity being the sum of two perpendicular 1D gratings. This allows a smaller period of the structure, shown in Figure 57, compared to the case of vertical polarisation.

Multibeam interference. 2D patterns with sharper than sinusoidal features and with nearly plain rectangular areas are possible if more then four interfering beams are used. The created computer program allows modelling of the intensity distribution for higher number of beams with arbitrary chosen wavevectors and polarisations and with equal or different intensities and wavelengths. Some examples of such modeling are presented in Figures 58 and 59. There was no experiment set up for such a large number of beams only because of the technical difficulties. It is worth noting that the size of the possible features is well below the wavelength of the light used and comes close to the resolution limit of modern photoemulsions.

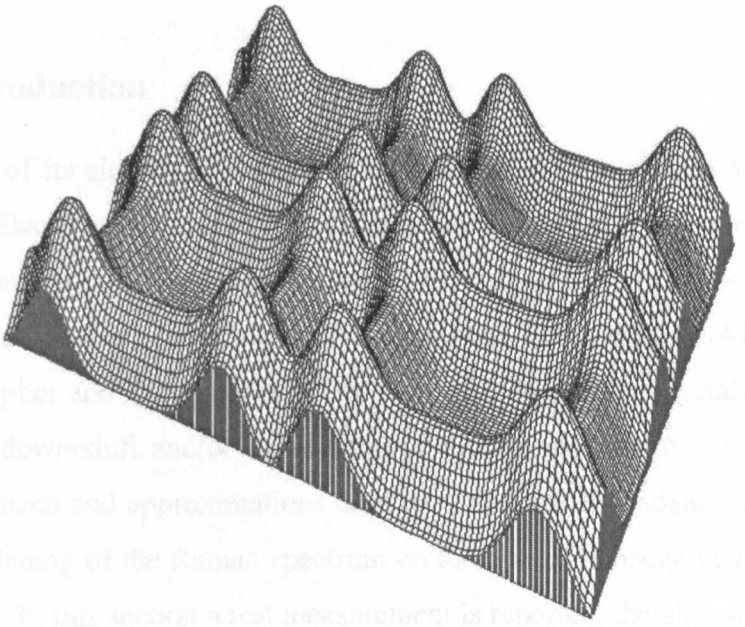

Figure 58. Calculated intensity pattern for eight interfering beams (two perpendicular pairs of counterpropagating beams plus similarly directed beams with twice shorter wavelengths and twice lower amplitudes).

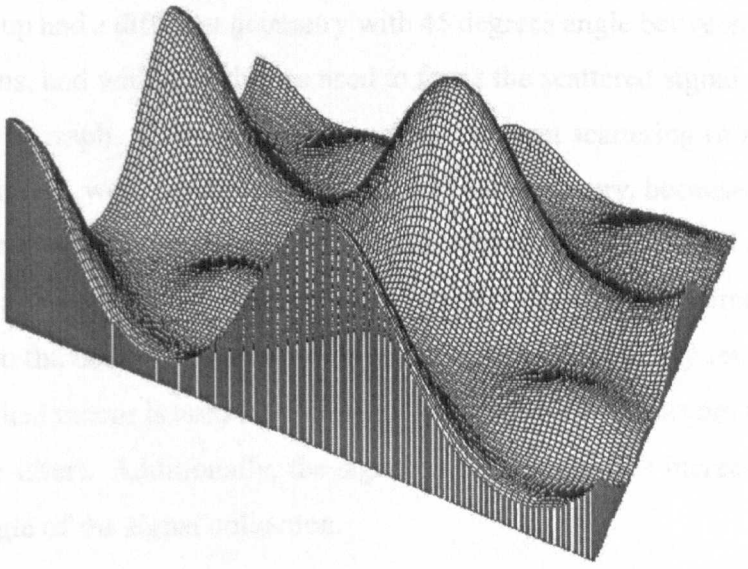

Figure 59. Calculated intensity pattern for five interfering beams corresponding to one central and four side optical field harmonics of diffraction on the rectangular 2D grid.

3.4 Raman Spectroscopy of free-standing porous silicon

3.4.1 Introduction

Because of its simplicity compared with X-ray diffraction and high resolution Transmission Electron Microscopy, Raman scattering become a popular technique for the determination of the Si-crystallite size and its distribution in porous silicon [142], [143] and of the fraction of nc-Si in nc-Si/amorphous Si thin films [144], [145]. The model of Campbel and Fauchet [146][13] is used to evaluate the crystalline size from the frequency down-shift and/or broadening of the Raman line at 520 Rcm^{-1}. The analytical approach and approximations used to model the dependencies of the down-shift and broadening of the Raman spectrum on the size of nanocrystals are discussed in Appendix C. In this section a test measurement is reported, the aim of which was to measure the crystallite sizes in porous silicon samples. The measured down-shifts were related to the sizes of nanocrystallites using the graphs presented in [146] or [147].

3.4.2 Experiment set-up

The Raman set-up shown in Figure 36 was used for this experiment. The previously used set-up had a different geometry with 45 degrees angle between the pump and the signal beams, and with glass lenses used to focus the scattered signal onto the entry slit of the spectrograph. First attempts to measure Raman scattering of solid samples, especially of silicon, were not successful with that old geometry, because of the low ratio between the intensities of the shifted and not-shifted scattered signals, and because of the noise contribution of the focusing lens material. The new set-up reduced the first problem (due to the nearly back-scattering geometry) and completely removed the second one (spherical mirror is used for focussing and no glass elements are involved apart from the notch-filter). Additionally, the signal-to-noise ratio was increased due to the larger solid angle of the signal collection.

[13] In this model a phonon wavefunction is chosen as a product of a Bloch wave and the Gaussian envelope weigting function with the boundary value of $\exp\left(-4\pi^2\right)$.

3.4.3 Samples

A sample of nearly free standing porous silicon prepared by anodisation in the Defence Research Agency (UK) laboratory was used with L. Canham's kind permission (sample 1). Its porous layer consists of parallel columns (or wires). Figure 60 shows an SEM side view of the porous layer. The resolution of the image is not sufficient to define the thickness of individual nanowires. The size of features seen in the image is well below 50nm. The thickness of the porous layer was measured to be about 400 μm with the bulk substrate residual of only about 20 μm thick. Photoluminescence measurements of this sample have shown weak red luminescence, which suggests the mean feature-size larger than 5-10 nm.

For the case of nanoporous silicon with visible luminescence, implying feature-size below 5nm, a sample with the morphology shown in Figure 61 was used (sample2). As Raman scattering probes only the top $1\mu m$ layer of the sample when 514 nm excitation is used, it can be assumed that only the top highly porous layer of the sample was acting in the signal formation.

3.4.4 Analysis of the results

Raman results are presented in Figure 62. Two graphs are shown for different types of porous silicon and two graphs for bulk silicon for comparison. The down-shift of the Raman peak of porous silicon compared to that of the bulk crystal from 520 to 519 or 518 Rcm^{-1} is evident from the results in Figure 62, in agreement with the results normally reported for porous silicon [142], [143]. According to the phonon confinement model [146] a down-shift of -1 Rcm^{-1} (solid circles) corresponds to approximately 10 nm crystallite sizes, which is in agreement with the feature-size visible in Figure 60. A further shift of $-(0.5 - 1.0)$ Rcm^{-1} (empty circles) can be associated with feature-size of 5 nm, which is reasonable for the top nanoporous layer of the sample shown in Figure 61. However, as it was pointed out recently in [147], it is impossible to obtain accurate and unambiguous results from Raman scattering measurements only, as the down-shift can be strongly influenced by the mechanical stress in the film [148]. The compressive stress-induced up-shift is suggested to be sufficient in some cases to

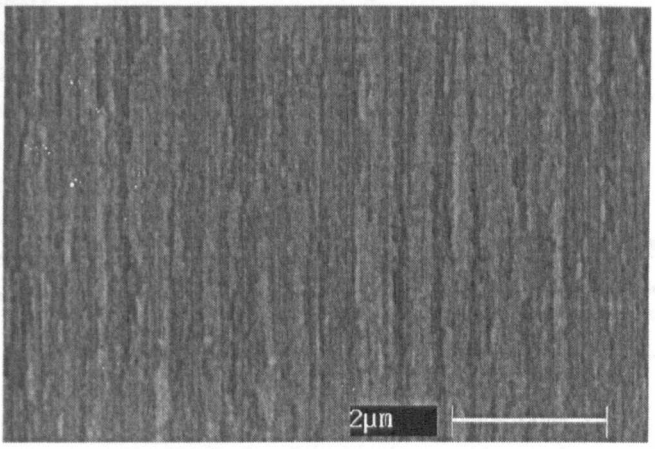

Figure 60. SEM image of porous silicon with perfect nanocolumns used for Raman spectroscopy measurements (sample1).

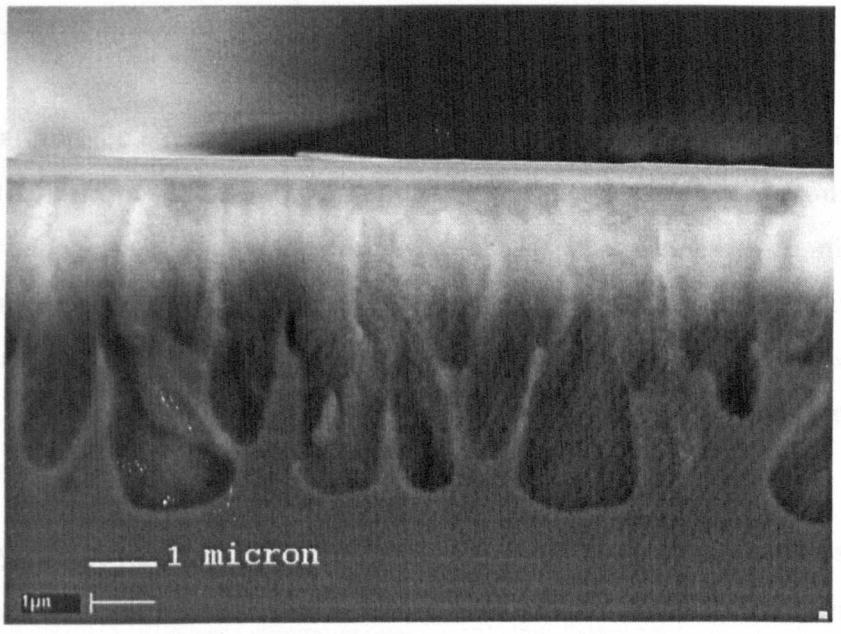

Figure 61. SEM image of anodically prepared nanoporous silicon (sample2), showing the differences in the morphology of the top (nanocrystalline) and bottom (macroporous) layers.

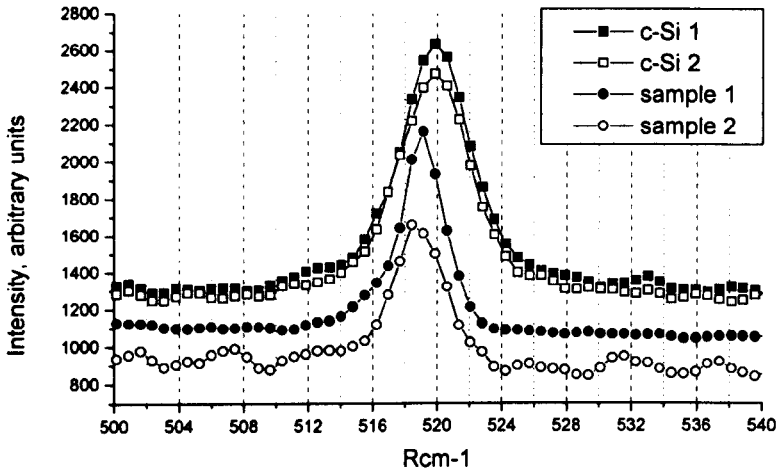

Figure 62. Raman results for bulk and porous silicon samples. Two spectra for bulk silicon and two for porous silicon with different porosities are shown. At least 1-2 Rcm^{-1} downshift for porous silicon is seen, increasing with nanoporosity.

completely compensate the confinement induced down-shift, whereas the tensile stress, if present in the nanoparticles, shifts the Raman peak down.

Thus, the conclusions are that

1. Disregarding the stress-induced effects, the measured nanocrystalline sizes are around 10 nm for the free-standing porous silicon (sample 1), and around 5nm for the nanoporous silicon (sample 2). Results are in agreement with microscopy data and with quantum confinement predictions from photoluminescence data for these samples: sample 1 has a weak red luminescence, while sample 2 has a bright orange luminescence (spectra for sample 2 are presented in the next section in Figures 64 and 65).

2. The crystallites in the samples studied could have considerably smaller sizes than reported above. Results of additional measurements by other techniques (XRD for stress and TEM for size distribution) are required to be considered along with Raman results to evaluate crystalline sizes.

It is worth noting that the results of similar measurements have recently been reported [149], with a much larger down-shift of the Raman peak. The broadening of the peak was approximately equal to the shift, whereas it should be 2-3 times higher than the shift according to the model referred to above. The difference is explained by the presence of a tensile stress with value up to 2 GPa as measured by X-ray diffraction. A correction of the original model [146] is proposed in [149], where the modelled peak is fitted to the experimental data by varying not just the size of nanocrystals, but also the central optical phonon frequency $\omega_0\,(q = 0)$ as a measure of stress, taken from complementary X-ray diffraction results. An excellent fit to the experimental data is produced.

3.5 Polarisation Dependance of Photoluminescence

3.5.1 Previous studies of polarisation effects

The polarisation dependence of porous silicon photoluminescence has been intensively studied by other groups. The main observation usually reported is that the polarisation of the emitted light in photoluminescence experiments is preferentially the same as that of the excitation light [53], [54]. The effect is understood as follows. The electron-hole pairs are preferentially generated in those nanocrystals which have their longer ellipsoid axis parallel to the electric field of the excitation light. This is due to the increased damping of the electric field component perpendicular to the nano-wires [150]. In light emission, again the polarisation has a preferential direction corresponding to the longer ellipsoid axis of the emitting nanoparticle, for the same reason [151]. Additionally, the information on the symmetry of excitonic states in silicon nanocrystals and on different heavy and light hole subband warping was obtained from analysis of polarisation ratios along different crystal directions at different temperatures [55].

Polarisation studies also provided insight into the mechanism of anodisation. In works [56] and [57] the observation of polarisation memory effect is reported, where the preferential orientation of long ellipsoid axes of nanocrystals was defined not only by wafer orientation and by direction of electric current, but also by the polarisation of illumination during the etching[14].

3.5.2 The subject of the present study, the model and the set-up

In the works quoted above, attention was focused on the photoluminescence intensities and the polarisation ratio of luminescent light. Silicon nanocrystals were considered as elongated ellipsoids, and all the analysis of polarisation effects always involved the discussion of the relative direction of electric field with respect to the direction of the longer axis of silicon ellipsoids. The idea of the experiment reported here was to study the PL peak position dependence on the polarisation of both the excitation and the emitted light.

---

[14] Mechanisms involved in preparation of porous silicon by anodisation process are discussed in section 3.2.

In the study reported here, silicon nanocrystals are treated as quantum wires. This approach can be justified by the notion that the polarisation effects reported before were always explained by non-sphericity of nanocrystals. The limiting case of an elongated nano-ellipsoid is, obviously, a nanowire. On the other hand, for *mesoporous* samples (those with characteristic sizes of the order of 20-300nm) the wired structure is normally reported (especially for anodically produced porous layers on (100)-oriented wafers) [152], [153]. Thus, the structure of parallel (interconnected) wires is, probably, a more realistic model (at least for some forms of porous silicon) than that of a random array of quantum dots. It should be also noted here, that the transition between the elongated ellipsoid and a wire may be understood not just via increasing the length of the larger ellipsoid axis, but also by considering a nanowire of a variable thickness (diameter) as a chain of roughly spherical nanocrystals, as in Figure 9 (a), p.23. For an exciton (or a single free carrier) such a chain may "feel" as a nanowire, if the wavelength of the Bloch component of its Ψ-function is much longer than a typical length of the wire diameter fluctuation (although the local maxima of $|\Psi|^2$ would be expected near the thicker regions of the wire). The term *wire* will, therefore, be used in the following as "a straight chain of nanocrystals" or as "a very long ellipsoid".

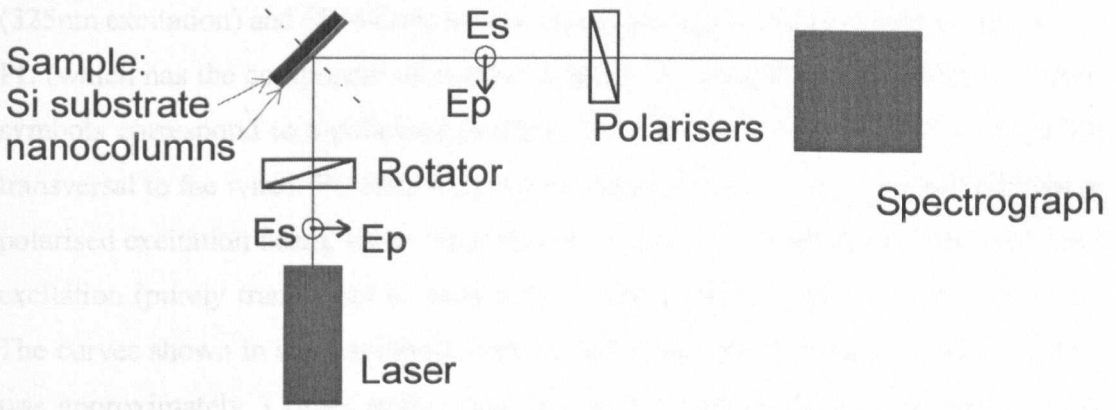

Figure 63. Scheme of experiment for studying polarisation effects of photoluminescence (the direction of nanowires is assumed perpendicular to the sample plane - shown with dot-dashed line).

The experimental set-up is shown in Figure 63. PL was measured in the direction perpendicular to the excitation beam, with the sample oriented at approximately

45 degrees to both directions[15]. The nano-wires were thus aligned at about 45° to both beams in the plane of incidence. S-polarisation, which is perpendicular to the plane of incidence (and to the picture plane) has no E-field component along the wires, whereas p-polarisation for both exciting beam and PL signal have non-zero electric field components parallel to nano-wires.

He-Cd laser was used for excitation at 325 and 442 nm wavelengths. When required, the polarisation of the exciting light was rotated 90° with a $\lambda/2$ plate, while the polarisation of the PL was controlled with a polariser.

The sample of PS was prepared by anodising (100) p-type silicon wafer of 7-10 Ωcm resistivity in 25% HF solution with an anodisation current density of 15mA/cm^2. An SEM image of the sample is shown in Figure 61. The total thickness of the porous layer is 5μm with only top 2μm layer being nanoporous. Crystalline wires are perpendicular to the surface and have a diameter below the resolution of the image: only bunches of nano-wires can be seen.

3.5.3 Experimental results

The measured spectra for two excitation wavelengths are presented in Figures 64 (325nm excitation) and 65 (442nm excitation). Solid symbols correspond to p-polarised PL (which has the component of electric field vector along the wires), whereas empty symbols correspond to s-polarised (normal to the picture plane) PL, which is purely transversal to the wires. PL results shown in square symbols were obtained with the p-polarised excitation beam, while those shown in circles were obtained with s-polarised excitation (purely transversal to nano-wires). The positions of PL maxima are given. The curves shown in solid symbols were scaled down: the intensity of p-polarised PL was approximately 3 times higher than that of the s-polarised PL. The graphs were smoothed using a 5-point adjacent-average algorithm. The longer wavelength limit of the detector used on the spectrograph was around 820 nm, therefore the right-hand regions of all spectra (above 800 nm) are depressed.

Three groups of observations can be drawn from the presented graphs:

---

[15] The angle should not be too close to 45°, otherwise specular reflection is directed into spectrograph.

1. S-polarised PL (empty markers) is less intense and is blue-shifted by approximately 10nm, compared to corresponding result for the other polarisation for each of the four different excitations: 325nm and 442nm wavelengths, s- and p-polarised.

2. P-polarised PL has a double-Gaussian shape for 325nm excitation, however the effect is not observed for 442nm excitation.

3. PL excited with s-polarised UV(325nm) light is red-shifted by approximately 10nm, while there is no difference in PL intensity for both UV and blue excitation depending on the polarisation of excitation light.

3.5.4 Qualitative agreement with Quantum Confinement Model

The above results can be understood within the framework of the quantum confinement model. It is assumed that S-band PL from PS is due to the up-shift of energies of excitons in crystalline Si nano-wires of quantum-size diameters (below 5nm).

First of all, the polarisation dependence of the PL intensity (compare solid (scaled down) and empty markers in Figures 64 and 65) is usually discussed in terms of the increased volume polarisability perpendicular to nano-wires [150]. However this does not explain the blue-shift of PL for the polarisation transversal to wires. On the other hand, in the experiment reported here the intensity of PL was not effected by the polarisation of the excitation light. The other observations to be explained are the red shift of the PL excited with s-polarised light, and the double Gaussian shape of the s-polarised PL signal. A qualitative model is proposed below to explain all the observed phenomena.

Consider the exciton energy E_{ex} in 1D nano-wires. Due to confinement in two directions perpendicular to the wire axis, E_{ex} has the following components [107]:

$$E_{ex} = E_g + E_Q - E_B + K_z \tag{3.38}$$

where E_g is the band-gap of the bulk Si, E_Q is the quantisation energy of electron and hole, E_B is the exciton hydrogen-atom-like bonding energy, and K_z is the kinetic energy of exciton as a whole in the only free dimension along the wire. E_Q is the energy component responsible for the up-shift, which brings the PL into the visible region. For simplicity we will refer to E_Q as electron confinement energy. In the cylindrical symmetry of nanowire, solutions for electronic wavefunction envelopes are

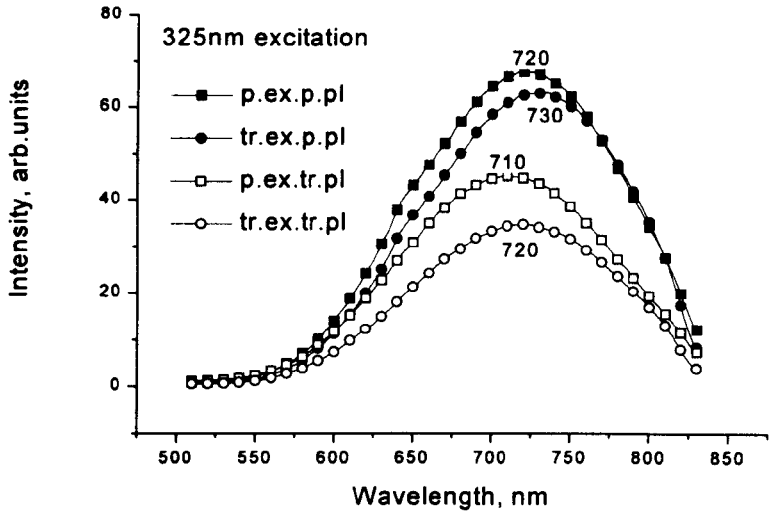

Figure 64. PL results for different polarisations of both excitation and signal beams, measured with UV (325nm) excitation. Legend: for example solid circles "tr.ex.p.pl", means "transversal excitation - parallel PL". The positions of PL maxima are given. The curves shown in solid were scaled down 1:2.

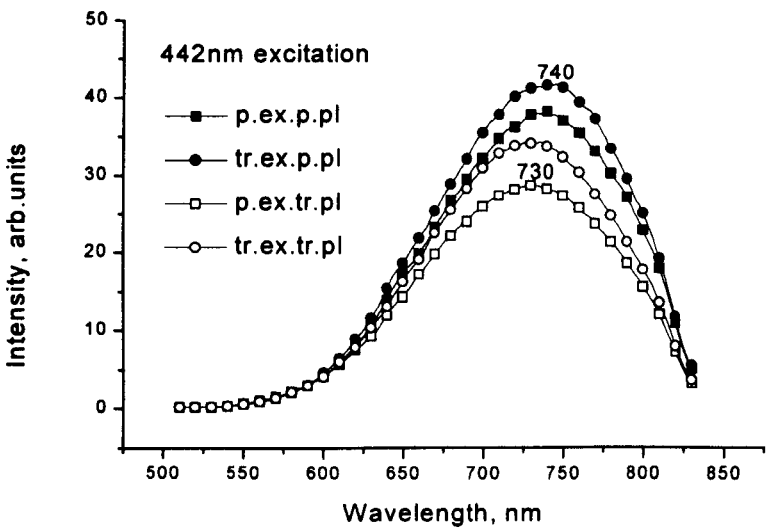

Figure 65. PL results for different polarisations of both excitation and signal beams, measured with blue (442nm) excitation. Notations same as on the previous figure.

found in the form of the product of Bessel functions and $\exp(il\varphi)$ harmonics[16]. E_Q is characterised with two quantum numbers: radial number $n = 1, 2...$ and angular number $l = 0, 1, 2...$ It is convenient to denote $E_Q(n, l) = E_{nl}$. The lowest quantised states, which are more likely to participate in light emission, have energies E_{10} and E_{11}. For the state with $l = 1$, the coupling of electric field polarised transversely to Si nano-wire with the dipole momentum of the exciton will be stronger than for the state with $l = 0$. This is because of the additional anti-symmetry of the electronic wave-function in the direction of the electric field (perpendicular to the axis of the wire). Therefore, these excitons will play the major role in the emission polarised transversely to nano-wires. The energy of these excitons is higher due to the difference in E_Q components ($E_{11} > E_{10}$) of the total exciton energy 3.38. This gives rise to the blue shift in PL for such polarisation. PL polarised along the wires, on the contrary, is composed mostly of emission from excitons with $l = 0$. The double-Gaussian shape of PL polarised along the wires for 325nm excitation can now be explained by the presence of emission from excitons with $l = 1$ and $l = 0$ in the spectrum. The "hint" of the second Gaussian seen in Figure 64 at 650nm is not present in Figure 65 for 442nm excitation. This is probably because the energy of 442nm photons is not enough for creation of excitons with $l = 1$, taking into account scattering by phonons and other losses of the absorption-emission process.

To understand the red shift of PL excited with s-polarised UV(325nm) light (transversely to nano-wires), consider the balance of energy for the excitation process:

$$\hbar\omega = E_e + E_h + E_{phon} = E_g + E_{Qe} + E_{Qh} + K_{ze} + K_{zh} + E_{phon} \qquad (3.39)$$

Here the continuum exciton states are considered, where the energies of electrons and holes can be treated separately and the exciton bound energy is disregarded.

In case of excitation with electric field transversal to 1D wires, confined electrons are created in the conduction band with the excess population of the $l = 1$ level ($N_{11} > N_{10}$). This is due to the same enhanced coupling of this state with the electric field transversal to wires, compared with that of the $l = 0$ state. The electrons with $l = 1$ have higher E_Q component and, consequently, lower K_z (equation 3.39), than those with $l = 0$. Due to the indirect bandgap in silicon, the lifetime of these excited states is long (milliseconds [52]). During this time the relaxation of the confined elec-

[16] Wave equation in cylindrical symmetry case is solved in, for example, [154].

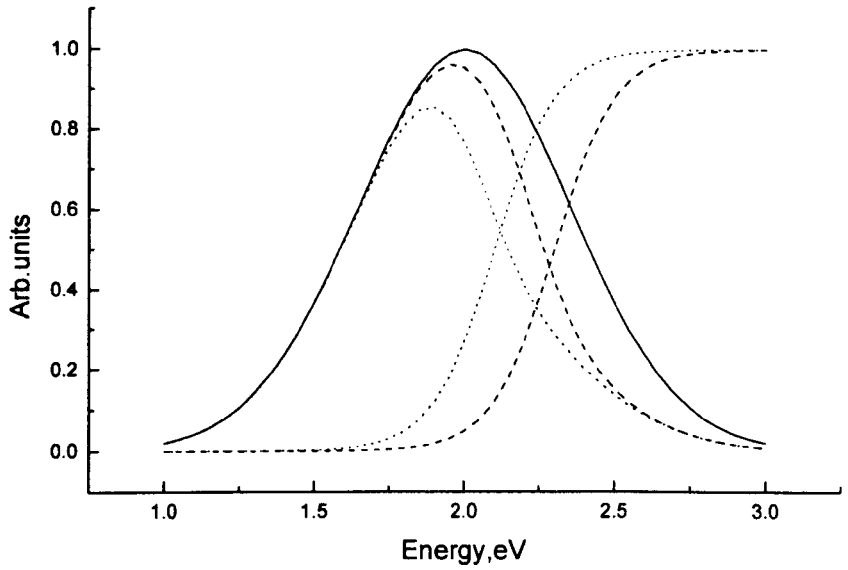

Figure 66. The original Gaussian spectrum centred at 2eV (solid line) is differently red-shifted by the threshold-like absorption near 2.3 eV (dashed lines) and 2.1 eV (dotted lines).

tron states occurs, the populations of $l = 0$ and $l = 1$ quantum levels come to equilibrium (Boltzmann) distribution with $N_{11} < N_{10}$. Meanwhile, the lack of K_z of electrons generated with such s-polarised excitation results in the decrease of the final exciton energy (equation 3.38). For the excitation with electric field along the wires, confined electron states with $l = 0$ are generated preferentially, with lower E_Q and higher K_z, consequently, the PL peak is not red-shifted (Fig.64, square markers). When 442nm light is used for excitation, the state with $l = 1$ are not created efficiently, that is why there is no dependence of PL peak position for different polarisations of blue excitation (Fig.65, square markers versus circles). This concludes the explanation of all the observed effects in the polarisation dependence of PL from porous silicon.

It is worth noting, that there is another approach for understanding of the red shift of the PL polarised along the wires. As the first principles modelling calculations of dielectric function in Si wires show [114], [155], the absorption near the energy threshold is increased for the light polarised along the wires. Consequently, the absorption threshold for the polarisation transversal to the wires is in the shorter wavelengths, compared with that of the other polarisation. This means that the blue component of the PL is

selectively damped in the light polarised along the wires, causing the red shift for this polarisation. The effect is illustrated in Figure 66, where the dashed lines correspond to the polarisation transversal to the wires, and the dotted lines to the parallel one. Taking into account the overall damping of the light polarised transversely to nano-wires, the quoted calculation result is in a good agreement with our observations.

3.6 Computer modeling of electrical conductivity of two-component media (embedded nanocrystallites)

3.6.1 Model

If optical properties caused by quantum confinement in nanocrystallites are ever to be used in integrated optoelectronics (Figure 2), the pumping of quantised electronic energy levels should be electrical (not optical, as in Figure 27). This makes the question of conductivity of embedded nanocrystallites extremely important.

Consider semiconductor nanocrystals embedded in a matrix. For free electrons (or holes) to be effectively delivered to nanocrystals, the matrix should have a wider energy gap. For modeling of conductivity of such a media, the nanoclusters can be considered as a conductive fraction, while the matrix is treated as insulator. In a simple computer simulation presented below, conductivity along a sample column is studied in an orthogonal 3D net, with the cross-section of the column being 120×80 cells. Zero or unity conductivity is assigned to each cell with a chosen probability ρ. In this simplified model the cells are cubic, that is why three types of contact of the nearest cells are possible: with cube faces, with edges and with corners. The probabilities of electrical contact for these types of contact were assigned as 1, α and 0 respectively, where α is a variable input parameter, characterising the "edge connectivity", i.e. the rate at which charge transfer occurs between cells touching with their edges. In physical terms, the charge transfer through faces always occurs (the cells touching with their faces can be considered as a single enlarged cell), the transfer through edge contact occurs with a variable rate (which allows one to model effects like *tunnelling* or *hopping*), and charge transfer through corners is disregarded. The calculation propagates along the column from layer to layer, marking the contacted cells out of the number of conducting cells, with only the two last calculated layers and a current layer being kept in memory at each moment. The number of contacted cells is monitored. Propagation stops when there is no contacted cell found in the current layer. The block-scheme of the simulation process is presented in Appendix D.

The conductivity of the media is characterised by N - the number of the last calculated (reached) layer. Although the cross-section of the column is only 120×80 cells, so that the width may be shorter than the length (the number of layers N)

processed by the program, the random distribution of conductive cells across the layers provides statistical averaging in directions transversal to the current. This makes the results applicable for conductivity of wide layers, when the distance between electrodes is much shorter than the width.

3.6.2 Remarks on the validity of the model

The first remark is that this modeling is looking at not similar but complementary effects to those usually studied for porous silicon conductivity (see subsection 2.3.2 and references therein). For example, the results for hopping conductivity obtained by means of quantum-mechanical treatment of adjacent nanocrystals could be extended using the results presented here to describe the macroscopic conductivity of the nanocrystalline layer.

Secondly, the model is very simplified and, strictly speaking, does not give an answer as to the *conductivity* of the media. What is actually studied is the *connectivity* of a set of items (or a connectivity from the first layer to the last layer through the net of randomly interconnected items). The full treatment would bring us to the separate class of problems dealing with Graph Algorithms [156]. Additionally, the connectivity of physical quantum-size particles is even more complex a question, because the connectivity between two adjacent clusters depends exponentially on the separation:

$$D_{tunneling} \sim \exp\left[-2\int (U(x) - E) * dx\right]$$

for a particle of energy E passing through a potential barrier $U(x) > E$ [19]. In terms of algorithm problem, this means very different *weights* for connections between *knots* depending on the microscopic separation. Another complication is that for *conductivity* simulation, what matters is not just a single found connection, but the number of different *paths*. There are algorithms developed both for finding a better path through a network of *weighted connections* and for *bi-connectivity* (when the connectivity is preserved if any single *connection* is broken or any single *knot* is removed) [156]. Unfortunately, those known algorithms could not be used for the problem studied here due to the vast number of cells (or *knots*). It was impossible to keep all the 3D array in the computer memory, which prevented systematic checking of all the possible roots, finding the number of different paths, etc. Connectivity *from layer to layer* rather than *from*

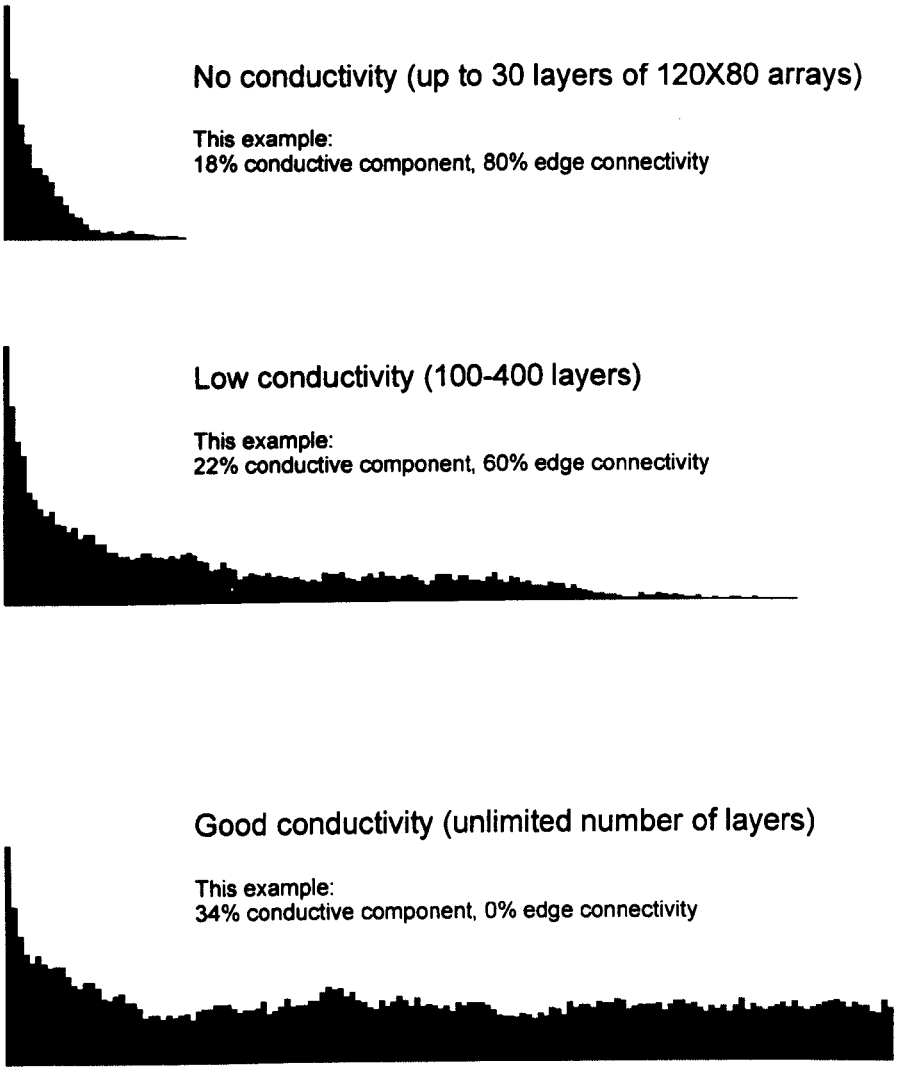

Figure 67. Examples of different types of modeled conductivity of two-component media. Vertical counts illustrate the dependence of the fraction of contacted elements (of the total number of conductive elements in the layer) on the number of the layer (counting from the left).

cell to cell was simulated, with the $(j-1)$-layer being removed from the memory before the $(j+1)$ layer was randomly defined (see Appendix D). On the other hand, the presented approach allows a study of the connectivity of a random, almost unlimited ((120 or more)×(80 or more)×(any N)), statistically averaged 3D array of a given spatial density ρ and a given average connectivity between cells α, rather than just a check of the connectivity of a given fully defined but limited set of knots.

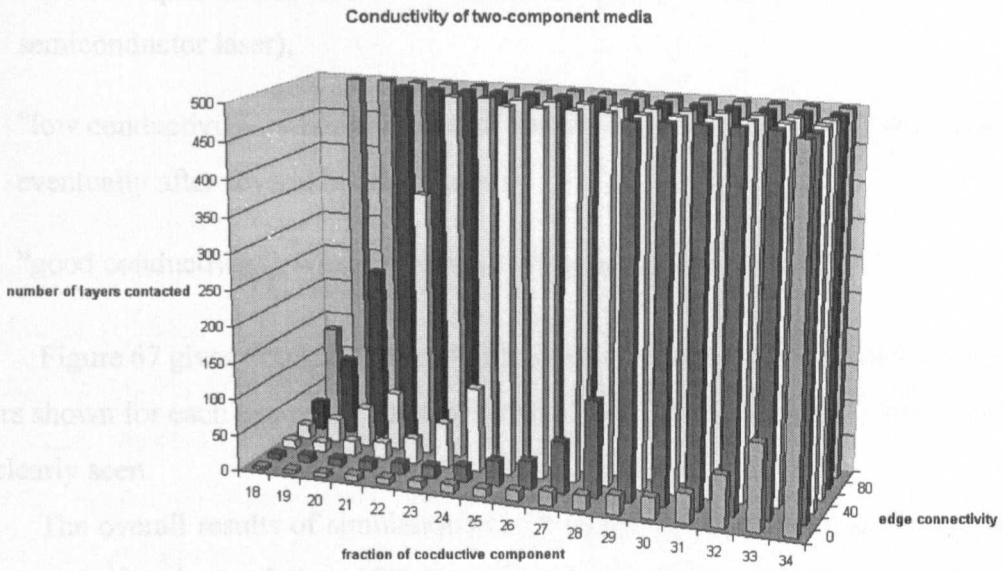

Figure 68. Results for conductivity of two-component media with variable fraction of conductive component (%) and edge-touch contact probability (%).

3.6.3 Results

By varying two input parameters, ρ - the fraction of the conductive component (corresponding physically to the volume density of nanocrystallites in the matrix) and α - the edge connectivity (corresponding physically to the charge tunnelling probability between touching nanocrystals), the longitudinal conductivity of the column was studied. For a 120 $\times$ 80 array of cells, the statistical result is that the propagation can be assumed unlimited if it does not stop after 400-500 layers. On the other hand, for α and ρ chosen below certain threshold values, the propagation stops within the first several tens of layers. Thus, depending on the number of the layer where the contact is lost, it is convenient to define three main types of media conductivity:

1. "no conductivity", when the contact does not reach more than 30 layers (in nanocrystalline film this would correspond to 50-100nm thickness of the layer,

which is equal or less than the thickness of the active optical layer in a typical semiconductor laser),

2. "low conductivity", when the contact reaches much more than 30 layers but stops eventually after several hundred layers,

3. "good conductivity", when the contact propagation is unlimited.

Figure 67 gives examples of modeling results, with the values of two input parameters shown for each example. The qualitative difference of three types of conductivity is clearly seen.

The overall results of simulation can be summarised as follows. For conductive component fractions ρ below 18% there is no conductivity (propagation is limited to several layers) for any value of connectivity α. For ρ values of 34% or higher the media is fully conductive for any α. In the transition region between these two thresholds for ρ, the second variable α plays an important role. Qualitatively speaking, the lack of the conductive component density can be somewhat compensated by the higher probability of edge connectivity between cells. The 3D graph $N(\rho, \alpha)$ in this transition area of interest is shown in Figure 68. By looking at the threshold dependance $\rho(\alpha)$ in the imaginary horizontal cross-section of the graph $N = const$, it can be seen that the result is in agreement with intuitive assumption, that the product $\alpha^x \rho^y$ (with positive exponents x and y) is a characteristic variable for the threshold equation[17].

[17] We don't spend time here on finding x and y to fit the modeling results because 1) the value of α itself has an exponential form (quantum mechanical tunnelling), and 2) x and y values may be quite different for the more real case of spherical rather than cubic nanocrystals.

3.7 Computer modeling of laser focused atom deposition

3.7.1 Introduction

This section informs on an interesting approach to synthetic fabrication of nanostructures with controlled lateral positioning. It is not necessarily linked to silicon: periodically arranged nanostructures of any material may be created in such a way. Although this study was "purely theoretical", and the obtained results give not much optimism as to the real application of the technique in the nearest future, it should be noted, that an impressive experimental demonstration of the effect has actually been carried out by the group from American National Institute of Standards [71]. The physics of the effect is based on the velocity dependence of the mean force experienced by an atom in a near-resonant optical field. The same effects are used in *laser cooling* [157], [158] or *laser confinement (manipulation)* [159], two other impressive applications of laser light for controlling speed and position of micro-particles. The force exerted on neutral atoms by optical radiation can be quite substantial in the neighborhood of an atomic resonance line. It provides the possibility of spatially controlled nanostructure fabrication using the effects of resonant radiation on atoms during deposition. The first proposal of nanometer-scale focusing was made by Balykin and Letokhov [160]. The absorption - spontaneous emission processes give rise to the so-called *scattering force*, which is velocity dependent because of the Doppler shift. This results in cooling or heating of atoms along the radiation wave vector for the light frequency tuned below or above the atomic resonance respectively. Induced emission, on the other hand, gives rise to a dipole or gradient force, attracting atoms toward lower or higher intensity regions for red or blue detuning respectively [161]. This force can be used for focusing atoms to nodes or antinodes of a standing optical wave with half-wave spacing between the resulting sites. With a short (UV) wavelength source this allows deposition of nanostructures.

Nanometer-scale periodical structure fabrication technology is an inevitable problem for the advance to more compact information storage, either magnetic or optical. Although a 100 nm feature size is already achieved with optical or electron beam lithography, the proposed use of near-resonant laser light for controlled atomic deposition

provides a long range accuracy of nanostructure spacing (limited only by the natural laser line width) and high fabrication speed since a vast number of nanostructures can be prepared simultaneously [162]. The first practical results were reported by McClelland et.al. [71], who created 34nm-height 60 nm FWHM chromium lines spaced 213nm apart (see Figure 69 for a similar structure with lower but narrower lines, produced in the same group[18]) and also a 2D array of 13nm height Cr dots, with total pattern size of about 200μm. A particle optics approach [163] was used to analyse atom focusing effects. The purpose of the computer simulation reported here was to provide detailed numerical results using quantum theory approach [161]. The results reported below were presented at the annual IOP CMMP (Condensed Matter and Material Physics) Conference in York, 1996 [164].

3.7.2 Set-up used in the original experiment and theoretical background

Figure 70 illustrates the effect of laser controlled atomic deposition. Two 200μm radius ($1/e^2$ intensity) 5 mW beams with +300 MHz detuning from atomic resonance were used to form a standing wave along the substrate, as shown in the scheme. Divergence of the atomic beam was decreased down to 0.4mrad using *transversal laser cooling* (cooling laser, top mirror and $\lambda/4$ retarder, as shown in the figure). The mechanism of cooling effect is explained below.

Mechanism of laser cooling of atomic vapors. Only a simplified qualitative picture is described here. Details may be found in [157] or [158].

Consider an atomic vapor in the optical field of two counter-propagating beams with frequencies ω tuned slightly below the atomic resonance ω_0. The rate of photon absorption (see [19]) is proportional to $g(\omega) = g_L(|\omega - \omega_0|)$ - the lineshape factor of the atomic resonance ω_0, which has the Lorenzian shape shown in Figure 71. For an atom moving toward the light source with the v_k velocity component along the k-vector of the optical field[19], the optical frequency seen by the atom is $\omega_+ = \omega\left(1 + \frac{v_k}{c}\right)$, and similarly for an atom moving away from the light source, $\omega_- = \omega\left(1 - \frac{v_k}{c}\right)$: the effect is

[18] Spacial thanks to J.J.McClelland and all his group for providing the complete information on their work.

[19] Nonrelativistic case of $v_k \ll c$ is considered here for simplicity.

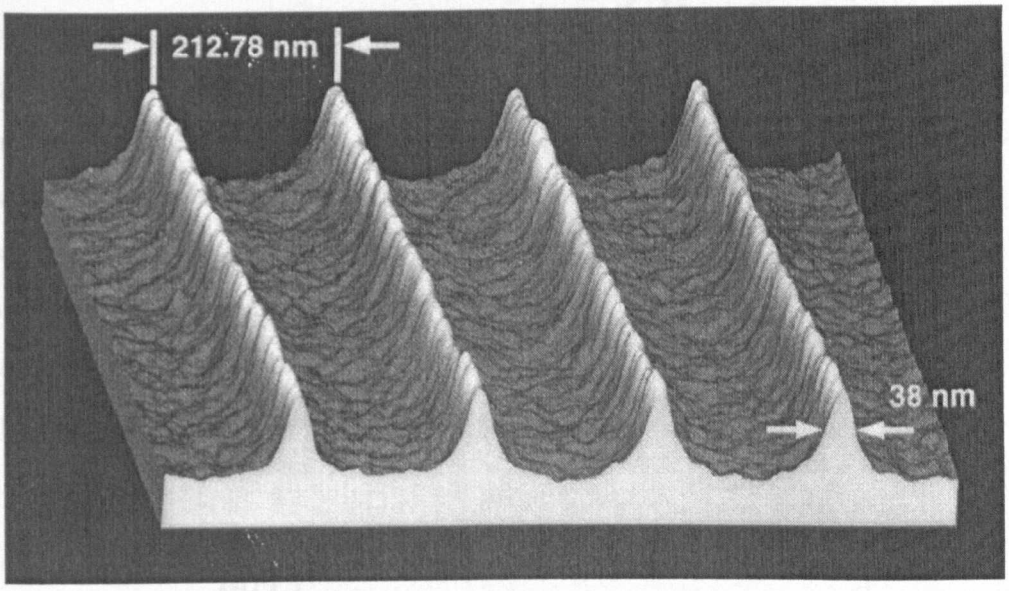

Figure 69. AFM image of Cr lines formed by laser-focused atomic deposition (ref. in text). The height of lines is around 8nm (vertical scale has been expanded).

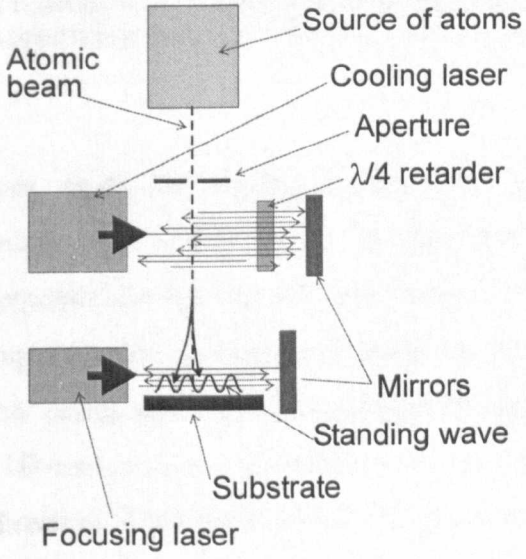

Figure 70. Scheme of the set-up for laser-focussed atomic deposition.

known as *Doppler shift*. If the detuning $\omega - \omega_0$ is adjusted so that $\omega_- < \omega < \omega_+ < \omega_0$, and all frequencies are well within the peak of $g(\omega)$, as shown in Figure 71, the rate of photon absorption will be higher in case of an atom and a photon moving toward each other (ω_+ is closer to atomic resonance ω_0), than in the other case, when the movements are in the same direction: $g(\omega_+) > g(\omega_-)$. On the other hand, the process of photon re-emission has no preferential direction. This causes the mean atomic momenta along the beams to reduce: the photon momenta are passed to absorbing atoms, and the number of the absorbed photon momenta opposite to the atom momentum is higher than that for photon momenta in the direction of atom momentum. Thus, *cooling of atomic velocities* along the k-vector of the optical field occurs.

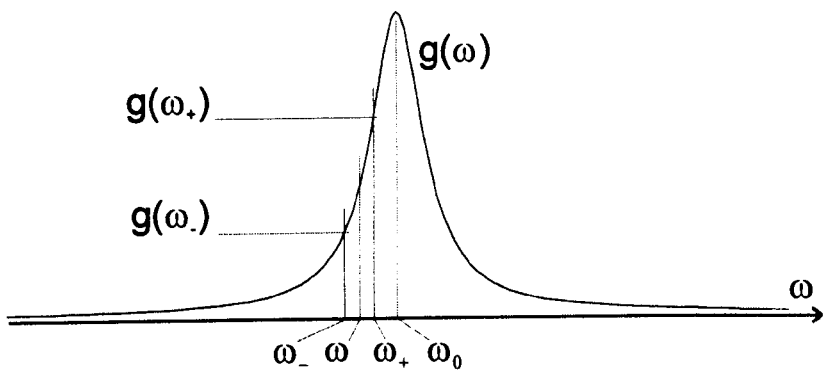

Figure 71. Illustration of the mechanism of laser cooling: the laser frequency ω is tuned slightly below the atomic resonance ω_0. Doppler-shifted frequencies are ω_- and ω_+ for atoms with velocities along and opposite to the photon flux, (see text for further detail).

Total force of atom. In the case of a standing wave, the same cooling (or heating, depending on the detuning) effect is present, plus the focussing effect of the intensity gradient. The general equation for the velocity dependent force is rather complicated, that is why only the simplified case of interest (the standing wave field, created by two counter-propagating laser beams with equal polarizations) is considered. Consideration is also restricted to the 1D-case, where v represents the atom velocity component along wavevector k in the x direction. The force and velocity are said to be *positive* if directed in the positive x-direction. For the standing wave $I = 4I_0 \cos^2(kx)$, the force can be written as follows (Appendix E):

$$f = \frac{2\hbar p_0 \Omega k}{1+p}\left(\sin(2kx) + \frac{\Gamma^2(1-p) - 2p^2\gamma^2}{\Gamma|\gamma|^2(1+p)^2}(1-\cos(2kx))\,kv\right) \qquad (3.40)$$

where v is the atom velocity component in the direction of the wave vector, k is wave-vector magnitude, Ω is laser detuning, $\gamma = \Gamma/2 - i\Omega$, where Γ is the radiative decay rate of the atom, $p = 2|g|^2 / |\gamma|^2$ is the saturation parameter and $g = i\boldsymbol{\mu}\mathbf{E}/\hbar$, where $\boldsymbol{\mu}$ is the electric dipole moment of the atom. Equation (3.40) was derived with the assumption that

$$kv\Omega \ll |\gamma|^2 \tag{3.41}$$

For practical applications, such as laser cooling or gradient focusing, $kv > \Gamma$ is required, and together with (3.41) this implies $\Omega \gg \Gamma$. When solving the problem of optimisation of Ω, one should note that p has $|\Omega|^2$ in its denominator for $\Omega > \Gamma$. This means that the smaller Ω should be chosen, with restriction (3.41) still valid.

In equation (3.40), the $\sin(2kx)$ term presents a gradient force, attracting atoms to intensity nodes or antinodes for positive or negative Ω respectively. The velocity dependent component (that is cooling or heating) vanishes in the intensity maxima, where $\cos(2kx) = 1$. Furthermore the effect reverses when $p^2/(1-p) > \Gamma^2/|\gamma|^2$, which means that there is heating for $\Omega < 0$. This occurs for $p > 10^{-2}$. In reality the mean p value is about 10^{-1}, thus this force component gives heating rather than cooling. Under usual experimental conditions, however, the coefficient of atom velocity v in (3.40) is of the order of 0.4 $(\text{m/s})^{-1}$. For a collimated beam, with transversal velocity component decreased to approximately 0.5m/s (which corresponds to 1/2 mrad divergence of a 1500K atomic beam), the maximum possible heating term contribution to $\sin(2kx)$ is only 0.2. Thus negative detuning can be used for focusing too, with atoms assembling in intensity maxima, where the heating is zero because of the $(1 - \cos(2kx))$ factor. On the contrary, heating can be of use to involve "dead" zones (close to $\sin(2kx) = 0$) in the focusing process. With positive Ω, the velocity dependent term gives rise to heating in the neighborhood of intensity nodes, just where atoms are accumulated, and this time the $(1 - \cos(2kx))$ multiplier is close to 2. Perhaps this is the reason that the experimentally deposited lines had width much greater than expected [163].

3.7.3 Computer simulation of atomic trajectories

Equation (3.40) was used to simulate the deposition process. C-program was developed to calculate the trajectories of atoms depending on the starting longitudi-

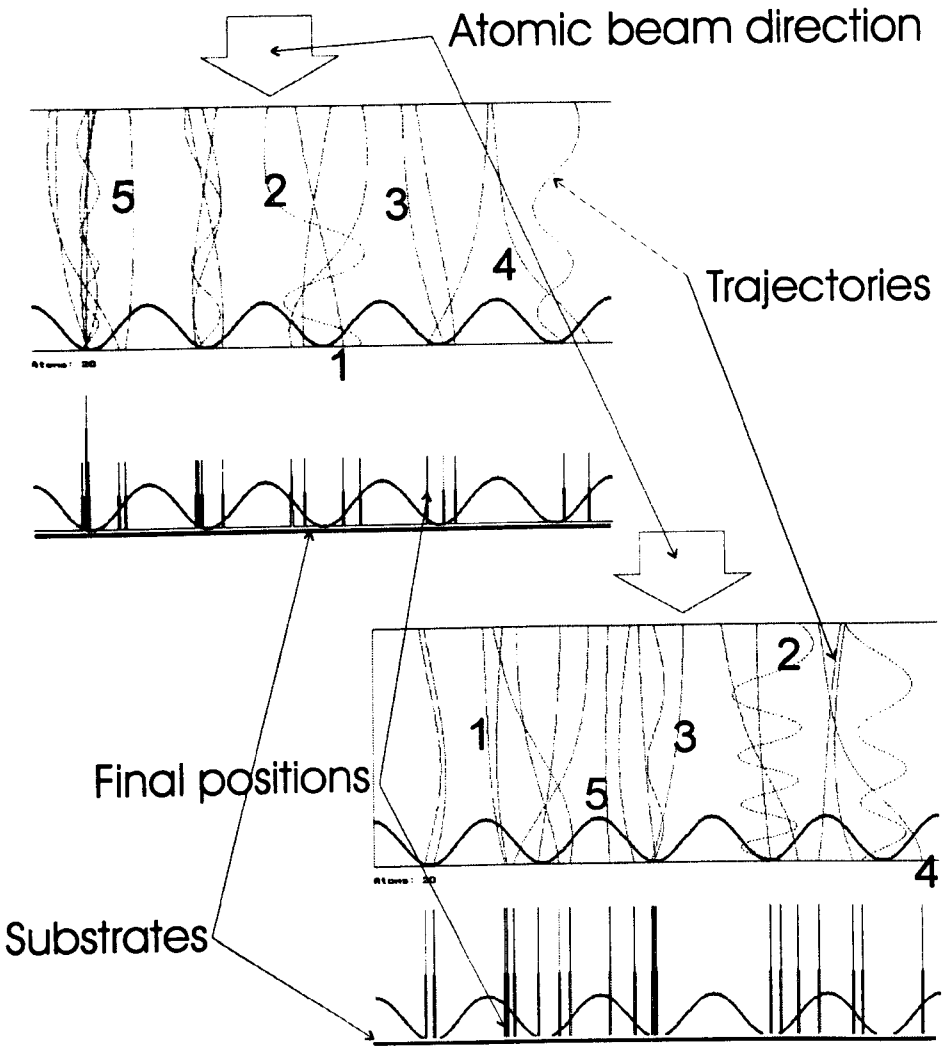

Figure 72. Computer screen snap-shots with calculation results (2 examples of 20 atoms each) showing the possible trajectories of atoms. See text for details.

nal (toward the substrate) and transversal starting velocities as well as on the starting transversal position relative to the standing wave. The discussion of the computer simulation procedure including the study of the stability of calculation results is presented in Appendix F.

Figure 72 gives an idea of possible trajectories of atoms in the field of a standing wave. Two examples are shown each with 20 calculated trajectories. Atoms were sent from the top with thermo-distributed vertical (transversal to the substrate) velocities and statistically random transversal velocities within a given beam divergence value. Final positions of atoms on the substrate are shown in the bottom of each example.

Bold sinusoidal lines on both top and bottom parts show the standing wave intensity. Examples of different types of trajectories are marked with figures:

1. these atoms were too fast to be focused by weak radiation scattering forces,
2. trajectories of slow atoms, oscillations in standing wave potential are seen,
3. these are the examples of ideal situations, when the flight-time was just enough to bend the trajectory into potential minimum,
4. these trajectories had crossed the equilibrium point, but had no time to come back,
5. atoms not necessarily too fast, but are in the areas with no gradient force.

These examples show the importance of longitudinal velocities of atoms. On the other hand, even with the filtered atomic beam (with longitudinal velocity distribution narrowed by some technique) it is not possible to focus all the atoms due to the "dead" areas in the vicinity of potential maxima, as no intensity gradient and, consequently, no focusing force is present there (trajectories of the type 5). These atoms will give an unwanted background even in the ideal situation of the same longitudinal velocity for all atoms and no divergence of the beam (no transverse velocities).

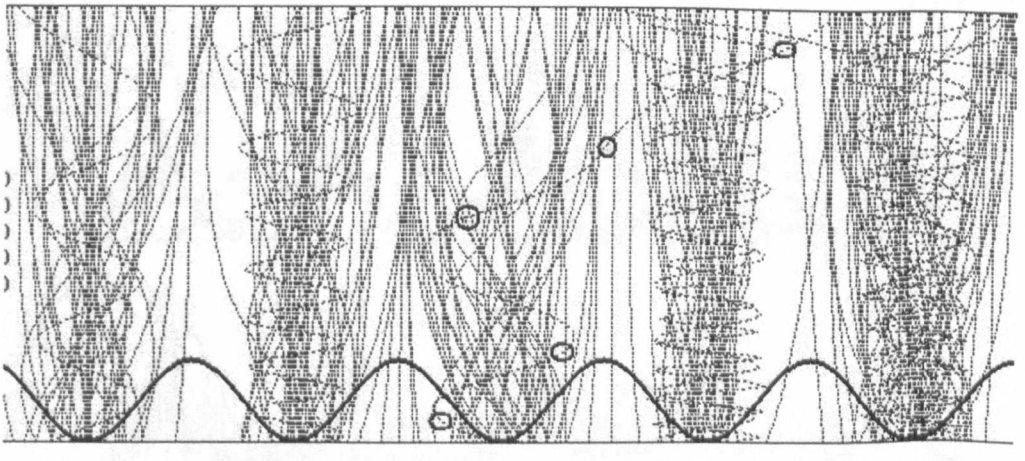

Figure 73. Screen-shot of calculated trajectories for 200 atoms.

An example of a screen-shot of trajectories for 200 atoms is shown in Figure 73. Two unusual trajectories are seen, one is highlighted with circles, when an atom has

crossed a potential barrier before being forced into oscillation. Such trajectories are possible when the standing wave intensity variation with the distance from the substrate is taken into consideration, corresponding to the Gaussian distribution of the laser beam intensity.

3.7.4 Simulation of dependencies of deposited shapes on experiment parameters

The dependencies of the deposited line width and shape on the laser power ($|g|^2$), detuning Ω and transversal velocity distribution δv (the divergence of atomic beam) were studied. One parameter only was varied, whilst the others were set to values known from the experiment reported.

Power dependance. Figure 74 demonstrates the beam power dependence of deposited features. The detuning value was set to 300 MHz, and the calculation was carried out for random initial atomic positions in the x direction with a thermal (1500K) velocity distribution and divergence of 0.4 mrad (which assumes atoms to be transversely cooled before entering the standing wave). Similar results were obtained for negative detuning ($\Omega = -300$ MHz), with atoms collected preferentially in positions of intensity maxima. No dependence of line shape on the sign of detuning was noticed.

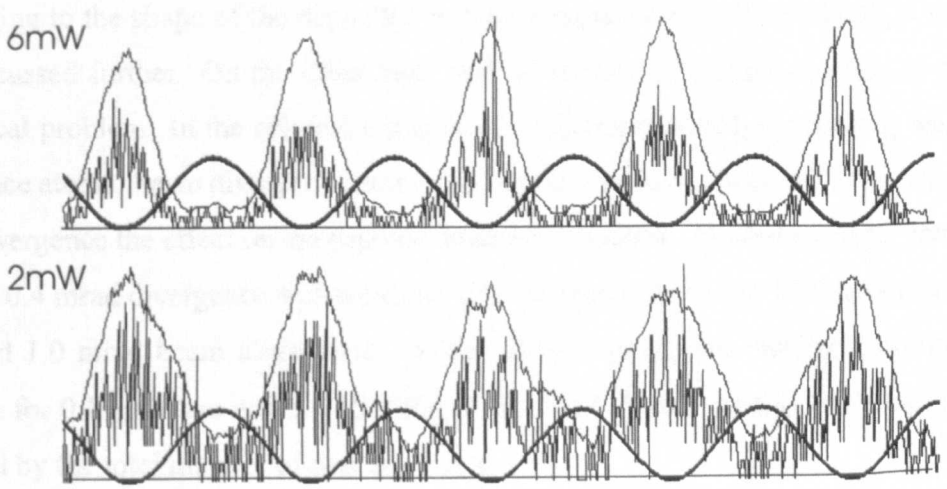

Figure 74. Power dependence of the shape deposited. Raw and 10-pixel-averaged data are shown for two different laser power values (vertical scales normalised). 2000 trajectories processed in each case.

Detuning effects. The dependence of line shape on detuning is demonstrated in Figure 75. Results for 100, 300 and 600 MHz are shown as marked, 10-point averaged in each case. Final curves are normalised vertically, which made height the same in all cases. Only the difference in shapes (the level of background between the maxima) actually matters: because equal numbers of trajectories (2000) were processed in each case, less background means higher maximum values (the area under the curve corresponds to the same total number of atoms). It can be seen that the background appears and line height decreases for large detuning (circle markers).

Velocity distribution effects. These were found to be the most important, as they play a major role in line broadening. Two distinct aspects can be discussed: collimation of an atomic beam and thermal distribution of longitudinal atom velocities. Firstly, a low degree of collimation means greater transversal kinetic energy of the atom, which allows it to overcome weak potential barriers created by the gradient force (the velocity independent term $\sin(2kx)$ of (3.40)). The second effect is physically similar to chromatic aberration: hot atoms (those with higher longitudinal velocities) cross the beam in a shorter time and the focusing is weak. Additionally, for very slow atoms oscillations occur in the gradient force potential of the standing wave, and their transversal position when they hit the surface is quite arbitrary. Because longitudinal velocities can be easily filtered mechanically, and, furthermore the effect was shown to be much less damaging to the shape of the deposited pattern compared with other effects, it will not be discussed further. On the other hand, the divergence of the beam presents a huge technical problem. In the original experiment [71], transversal laser cooling was used to reduce atomic beam divergence down to 0.4mrad. However, even with this extremely low divergence the effect on the deposited shape is essential. In all the results presented before 0.4 mrad divergence was assumed. For comparison, Figure 76 shows results for 0.1 and 1.0 mrad beam divergence. Again, all the curves are vertically normalised. Shapes for 0.1 mrad are much higher than those for 1.0 mrad, as the area under curves is fixed by the total number of deposited atoms.

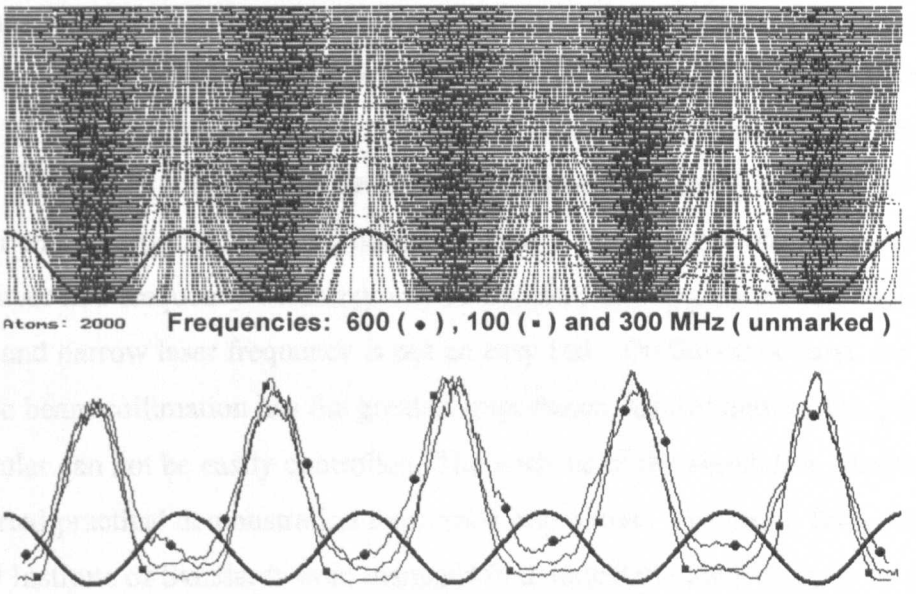

Figure 75. Dependence of the deposited shapes on the laser detuning Ω for three different values as marked (2000 atoms in each case, vertical scale normalised). Trajectories are shown on the top (not seen separately, but atom flux convergence to potential minima is evident).

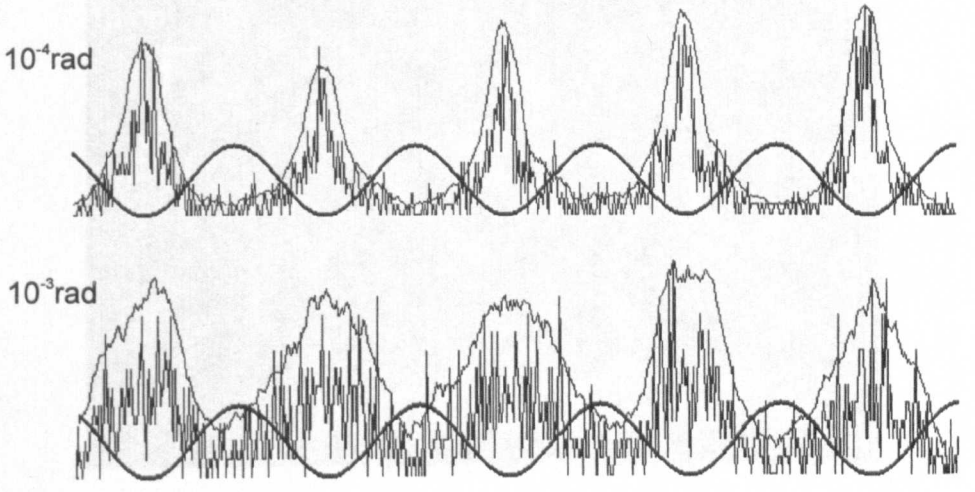

Figure 76. Dependence of deposited shape on the divergence of the beam. Results for two 10-times different divergencies are shown as marked (raw and 10-point averaged, same numbers of atoms, vertically normalised).

3.7.5 Conclusion

Summarising all of the above observations, the requirements for the accuracy of the experiment parameters were found to be very challenging, so that the technique is unlikely to be commercially used in the nearest future. Simulation results show that velocity homogeneity, mainly the divergence of the atomic beam, is of crucial importance for the quality of deposited nanostructures. The controllable parameters, like beam power and frequency detuning, can be adjusted and optimised, although an adjustable and narrow laser frequency is not an easy task. On the other hand, the degree of atomic beam collimation has the greatest importance. Unfortunately, this parameter in particular can not be easily controlled. The analysis of the simulation results makes the reported practical demonstration even more impressive. The group from American National Institute of Standards even managed to demonstrate the technique by producing a two-dimensional periodical pattern created by using two perpendicular standing laser waves (similar to the approach modelled in Figure 51 and recorded on photoresist in Figure 53). The reproduction of atomic microscope image is shown in Figure 77 [165].

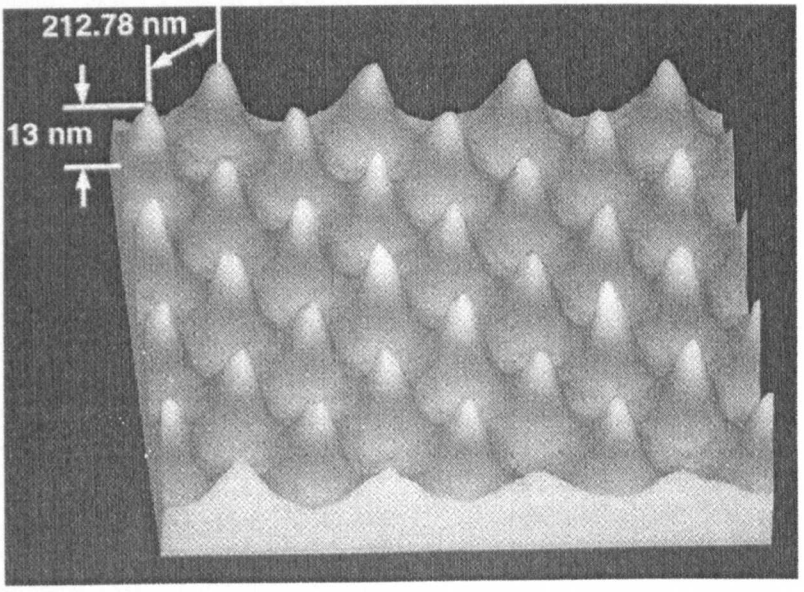

Figure 77. AFM image of 2D array formed by laser-focused deposition of Cr atoms (see ref. in text).

Chapter 4
Conclusions

"I have explained it so clearly, that now I understand it myself"

Unknown Lecturer

***

The subject of optoelectronic applications of nanocrystalline silicon has been discussed in this thesis. The properties of porous and other forms of nanocrystalline silicon have been studied both by reviewing the previously published material and by own practical experiments within the framework of the subject. Because all the fields of knowledge involved belong to relatively new and rapidly developing scientific areas, introductory information was also presented on:

- The terminology and requirements of modern microelectronics.
- The preparation and unusual properties of nanoclustered silicon.
- The theory and computational results of quantum dot physics.

Nanocrystalline silicon is a potential material for integrated optoelectronics. The study of its properties and of the mechanisms involved is a challenging task for modern solid state physics. The author's contribution to this field of study includes the following results:

- The physical limits on the lateral resolution of light-assisted electroless chemical preparation of the structured porous silicon films were determined. In the reported experiment a structure with 10 μm sizes was created. The technical limitations on the resolution of the process were defined. Changes to the present set-up including interferential techniques are proposed to overcome these limitations. Physical limitations are imposed by carrier diffusion effects, limiting the maximum possible resolution to about 2-5 μm.
- The polarisation effects on the photoluminescence spectra of porous silicon were studied. The results provide an indirect confirmation of the quantum confinement model for visible luminescence in porous silicon, based on the geometry of exciton states in silicon nanowires.
- The possibility of using Raman Spectroscopy for determining the nanocrystallite sizes in porous silicon was verified. 1-2 Rcm^{-1} shifts of Raman peak were detected. The results of complementary techniques are required to unambiguously relate the measured values to the sizes of nanocrystallites.

- An approach was developed for determining the threshold parameters for the electrical conductivity of two-component conductor/insulator systems. The results allow one to relate the threshold macroscopic value for the conductive component fraction to the microscopic characteristics of connectivity between conductive particles. The approach can be useful for analysis of conductivity of silicon nanocrystals embedded in insulating matrix.
- An alternative approach to nanostructure fabrication, namely laser focused atomic deposition, as an example of a synthetic approach to the problem, was also studied. This was carried out by quantum-mechanical treatment followed by computer simulation. This work led to the conclusion, that the technical requirements of the process are difficult to satisfy. For example the divergence of a cold atomic beam should not exceed 10^{-4} radian for the deposited feature size within 50 nm (FWHM).
- The recently published experimental and theoretical results related to optoelectronic applications of nanocrystalline silicon are summarised with the aim to define the strategic directions for further research.

Conclusions are summarised and generalised in Table 5, where positive and negative results are listed separately. The method of research is designated by "Rev", "Exp" or "Mod" for a review, experimental or computer modeling research respectively. Numerical quotations are avoided in the table for ease of reading. On the other hand, what is included is the new knowledge which contributes to an improvement of the understanding of the subject.

As to the theoretical part of this thesis, the summarising conclusion is that, so far, we do not have answer as to whether the direct transitions can dominate in silicon nanocrystals. Therefore, it is still possible that nanosilicon could play a major role in the optoelectronics of the future, and even the possibility of nanosilicon laser can not be ruled out based on the present knowledge.

The current situation of the field has overgrown the initial stage of the enthusiastic rapid rise, and has entered an extensive and troublesome phase of detailed and focused research. Further experiments, interlinked with the development of a theoretical understanding of the subject, will give the answer as to whether nanocrystalline silicon can provide long-term solutions for the microelectronics of the next century.

Research subject	Method	Positive results	Negative results
Evaluation of capabilities of nano-silicon as opto-electronic material of the future	Rev	Due to the low cost, CMOS compatibility and highly developed technology of its host material - bulk silicon, and due to own new optical properties, nano-crystalline silicon is found to be a promising candidate for modern opto-electronics.	Low efficiency and stability of luminescence from nano-crystalline silicon seem as the main problems for the development of silicon-based micro-opto-electronics.
Theoretical physics of quantum dots	Rev	This rapidly developing field of theoretical physics is on its way to bring understanding of gained experimental results	The theory of quantum dots formed from indirect gap material is in its very early stage yet
One-step preparation of 2D-structured luminescent porous silicon layers	Exp	A technological possibility of one-step preparation of 2D-structured luminescent porous silicon layers with resolution of ten of microns is demonstrated. Structured layers with stable orange photo-luminescence are prepared by electroless process with characteristics similar to those of anodically produced porous silicon.	Limitations of the technique on the lateral resolution and the depth of the produced layer are discovered. Lateral resolution could be improved by optimising the optical system, but is finally limited by carrier diffusion. Depth of the structure can not be increased.
Polarisation study of photo-luminescence from anodised porous silicon	Exp	Polarisation effects are detected in anodised porous silicon at room temperatures. Analysis improve our current understanding of photo-luminescence mechanism in silicon nanowires.	It is impossible to obtaine quantitative results based on the measured dependencies due to the lack of theoretical knowledge on exciton states, effective masses, etc.
Raman spectroscopy of nano-silicon	Exp	Confinement induced shift of Raman peak is detected in porous silicon using developed Raman system.	For useful quantitative results to be possible, information on internal stress from other techniques (like XRD) should be added.
Conductivity and connectivity of nano-silicon	Mod	Reasonable simulation results are produced for threshold values of conductive component fraction and cluster connectivity.	Time characteristics of charge transfer can not be modeled by means of simplified approach used.
Laser focused atomic deposition for nano-structure preparation	Mod	Simulation computer program is created based on quantum-mechanical analytical formulas. The results are in full agreement with the only known reported experiment.	The focusing effect is found to be too weak compare to thermal uncertainties for the technological application of the method in the near future.

Table 5. Table of conclusions for separate subsubjects of this thesis

Appendixes

Appendix A.
Electron states in crystals

The potential field experienced by electrons in crystals is periodic. To see how it determines the properties of electron states, consider the simplest case of one-dimensional periodic potential shown in picture below, where regions 1 denote barriers and regions 2 denote wells.

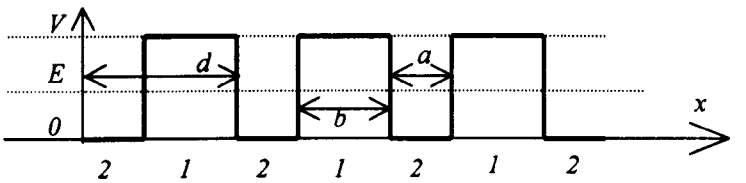

The potential $V(x)$ has a period $d = a + b$, where b is the thickness of barriers and a is the width of atomic wells. Schrodinger equation for an electron wave function $\Psi(x,t)$ in a potential $V(x)$ is:

$$i\hbar\frac{d\Psi}{dt} = -\frac{\hbar^2}{2m}\frac{d^2}{dx^2}\Psi + V(x)\Psi \tag{A.1}$$

To find a solution with a definite energy E, we separate the time-dependant part of Ψ from the spatial part:

$$\Psi(x,t) = e^{-iEt/\hbar}\phi(x)$$

After this substitution, equation (A.1) becomes:

$$-\frac{\hbar^2 d^2}{dx^2}\phi(x) = (E - V(x))\,\phi(x)$$

In both 1 and 2 regions $\phi(x)$ is a superposition of two linearly independent solutions (where natural n is the number of a considered unit cell):

$$\phi_1(x) = a_n e^{k_1(x-nd)} + b_n e^{-k_1(x-nd)} \tag{A.2}$$

$$\phi_2(x) = c_n e^{ik_2(x-nd)} + d_n e^{-ik_2(x-nd)} \tag{A.3}$$

$$k_1 = \sqrt{2m(V-E)}/\hbar \tag{A.4}$$

$$k_2 = \sqrt{2mE}/\hbar \tag{A.5}$$

For the energy E within the range between 0 and V, the solution is oscillating in wells and exponential in barriers.

By requiring that $\phi(x)$ and $d\phi(x)/dx$ are continuous in $x = nd$ and in $x = nd+a$ for all natural n, four equations can be written down for six coefficients a_n, b_n, a_{n+1},

b_{n+1}, c_{n+1} and d_{n+1}. This allows to relate a and b in two adjacent cells in the form:

$$\begin{pmatrix} a_n \\ b_n \end{pmatrix} = \begin{pmatrix} A & B \\ C & D \end{pmatrix} \begin{pmatrix} a_{n+1} \\ b_{n+1} \end{pmatrix} \tag{A.6}$$

where

$$AD - BC = 1 \tag{A.7}$$

On the other hand, due to the translational symmetry requirement together with periodic boundary condition, $\phi(x)$ should have the form of the product of the complex wave e^{iKx} and a real function $u(x)$ periodical in x with the same period as $V(x)$: $u(x+d) = u(x)$. This requires:

$$\begin{pmatrix} a_{n+1} \\ b_{n+1} \end{pmatrix} = \begin{pmatrix} a_n \\ b_n \end{pmatrix} e^{iKd}$$

Together with (A.6) this gives:

$$\begin{pmatrix} a_{n+1} \\ b_{n+1} \end{pmatrix} e^{-iKd} = \begin{pmatrix} A & B \\ C & D \end{pmatrix} \begin{pmatrix} a_{n+1} \\ b_{n+1} \end{pmatrix} \tag{A.8}$$

which has nontrivial solutions only for K satisfying characteristic equation

$$\cos(Kd) = \frac{1}{2}(A + D) \tag{A.9}$$

where (A.7) was used. The equation above is also a dispersion relationship for electron waves in a crystal.

Two linearly independent eigenvectors with $K_1 = -K_2 = K$ are:

$$\begin{pmatrix} a_0 \\ b_0 \end{pmatrix} = \begin{pmatrix} B \\ e^{-iK_{1,2}d} - A \end{pmatrix} N \tag{A.10}$$

where N is a normalisation constant.

Thus, the final electron wave-function in the n-th barrier is found in the form:

$$\Psi(x,t) = N\left[\left(a_0 e^{k_1(x-nd)} + b_0 e^{-k_1(x-nd)}\right) e^{-iK(x-nd)}\right] e^{i(Kx - Et/\hbar)} \tag{A.11}$$

where the portion within the square brackets is periodic in x with the period d.

Important conclusions can be drawn from this solution:

1. A wave function is of the form of a complex wave with a propagating constant K dependant on the energy E. Only for certain energy ranges E, for which the solution exists for (A.9), a non-evanescent solution is possible. The shape of the wave within a unit cell is described by the portion in the square brackets of (A.11). Other ranges of E are called forbidden gaps.

2. For $Kd = m\pi$, where m is integer, both eigenvectors (a_0, b_0) are the same. A standing wave is formed, which corresponds to the effect of Bragg reflection of electron waves from periodic potential barriers in the crystal. Standing waves with their nodes at the barriers correspond to the bottom of the forbidden gap, while those with their extrema at barriers correspond to the top of a forbidden gap.

3. As Kd is determined to within $2m\pi$ with any integer m, a reduced zone scheme is possible, where only K-range between $-\pi/d$ and $+\pi/d$ is considered, and a set of energies E_n corresponds to every propagation constant K (see the picture below).

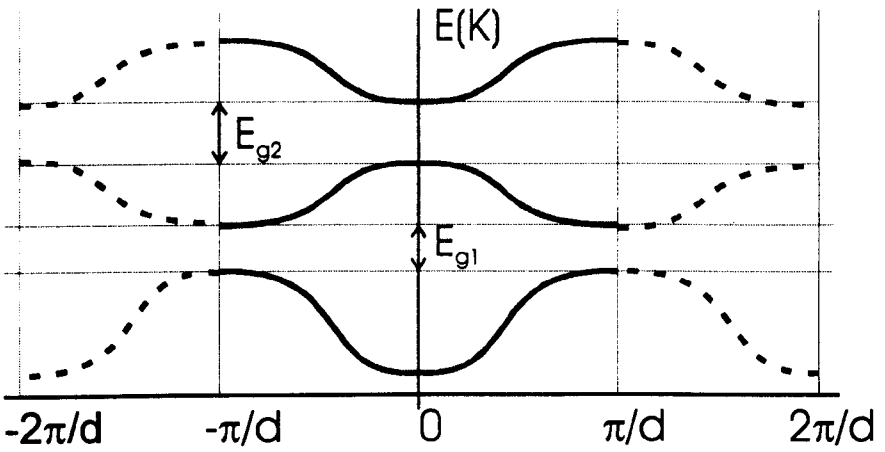

Appendix B.
Computer calculation of intensity distribution for a given set of monochromatic beams

The program used for calculation of 2D intensity distribution (Figures 51, 56, etc.) accepts the input data in the form of 8 parameters for each beam $i = 1, 2, ...$ These are: the wavelength λ_i, three components of the wavevector $\vec{\mathbf{k}}_i$ (only the ratio is used, the absolute value $\left|\vec{\mathbf{k}}_i\right|$ being normalised according to the wavelength λ_i), the relative amplitude of the optical field $\left|\vec{\mathbf{E}}_i\right|$, and three components of the electric field vector $\vec{\mathbf{E}}_i$ (again, only the ratio matters, the orthogonality of $\vec{\mathbf{E}}_i$ and $\vec{\mathbf{k}}_i$ is automatically checked). The image plane is always $z = 0$, which should be remembered as a reference basis for both vector parameters $\vec{\mathbf{E}}_i$ and $\vec{\mathbf{k}}_i$.

After the parameters of all the beams have been entered, the program asks for the size of the pattern D, which is then divided into a given number N of spatial steps δx and δy. Thus, the 2D rectangular net of $N \times N$ points is defined covering the physical surface ($x \in [0; D], y \in [0; D], z = 0$). N is chosen around 100 to allow separate appearance of pixels on the output picture, and, on the other hand, a sufficient spatial resolution to smoothly follow the intensity changes, which vary on a scale of λ. The optimal value of D depends on the values of the transversal components k_x and k_y of $\vec{\mathbf{k}}$.

The calculation part of the program consists in calculating $N \times N$ array of intensity values $I_{m,n} = I(m * \delta x, n * \delta y, 0)$ according to

$$I_{m,n} = E_{m,n,x} E^*_{m,n,x} + E_{m,n,y} E^*_{m,n,y} + E_{m,n,z} E^*_{m,n,z} \qquad \text{(B.1)}$$

where each electric field component $E_{m,n,j}$ is found,according to the superposition principle, as the sum of E_j-components over all the beams:

$$E_{m,n,j} = \sum_i E_{m,n,i,j} = \sum_i E_{i,j}(0,0,0) \exp\left[\mathrm{i}\left(m * \delta x * k_{i,x} + n * \delta y * k_{i,y}\right)\right] \qquad \text{(B.2)}$$

The vector summation of superimposing electric fields of several beams in each point is schematically demonstrated in the picture below. In the program, however, the x, y, and z-components are summed separately (B.2), this allows the easier calculation of I, as the sum of the three EE^* components (B.1).

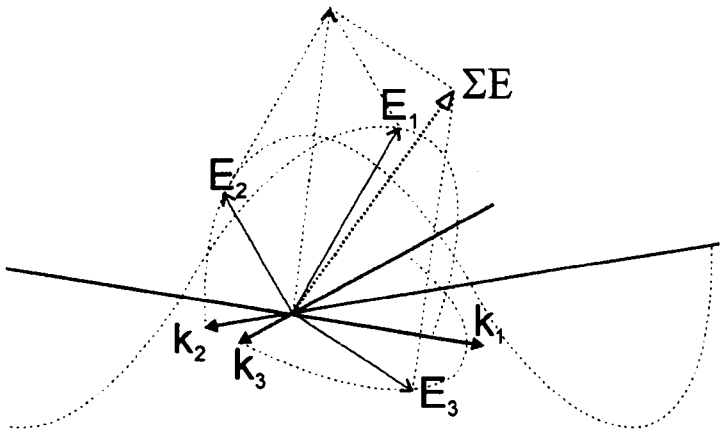

The graphical output of the calculated array $I_{m,n}$ presents a more difficult programming problem than the calculation itself. The surface plot is composed of non-transparent polygons

$$[(I_{m,n}; x_m; y_n); (I_{m+1,n}; x_{m+1}; y_n); (I_{m+1,n+1}; x_{m+1}; y_{n+1}); (I_{m,n+1}; x_m; y_{n+1})]$$

projected onto a view plane (computer screen) with correction for perspective effects. Given the user input parameters h, b/a and ϕ, defined in Figure 78, the program calculates $[hor_{m,n}; vert_{m,n}]$ representation of a 3D object defined with an array $[I_{m,n}; x_m; y_n]$. The drawing is executed back-to-front, which gives priority to visible surfaces. Semi-transparent edges of the 3D structure are drawn separately, those corresponding to the back edges are drawn prior to the surface, and those corresponding to the front edges after the surface was drawn.

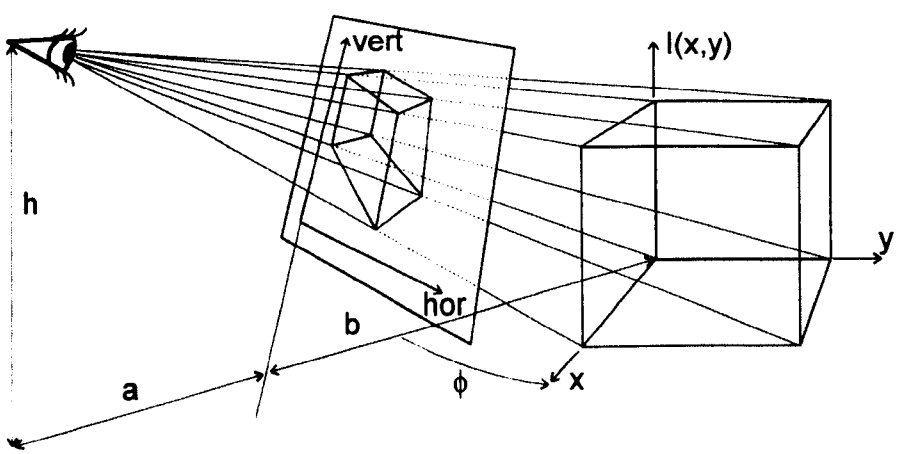

Figure 78. Geometrical scheme of projecting 3D objects onto a plane of view with perspective effects.

Appendix C.
The effect of nanoparticle size on the Raman spectrum

The information presented below is an outline of the approach used in [146] to simulate the dependencies of Raman spectrum on the size of nanocrystallites.

The wavefunction for a phonon of wavevector $\mathbf{q}_0$ in the bulk crystal may be expressed as

$$\Phi(\mathbf{q}_0, \mathbf{r}) = u(\mathbf{q}_0, \mathbf{r})\, e^{-i\mathbf{q}_0 \cdot \mathbf{r}}$$

where $u(\mathbf{q}_0, \mathbf{r})$ has the periodicity of the lattice. The phonon in a microcrystal becomes

$$\Psi(\mathbf{q}_0, \mathbf{r}) = W(\mathbf{r}, L)\, \Phi(\mathbf{q}_0, \mathbf{r}) = u(\mathbf{q}_0, \mathbf{r})\, \Psi'(\mathbf{q}_0, \mathbf{r})$$

where $W(\mathbf{r}, L)$ is the envelope weighting function taken as $\exp(-\alpha r^2/L^2)$, with L taken as the diameter of the microcrystal, and α is defined by some assumed boundary condition for W at an interface, to be defined later.

$\Psi'(\mathbf{q}_0, \mathbf{r})$ is then expanded in a Fourier series

$$\Psi'(\mathbf{q}_0, \mathbf{r}) = \int d^3q C(\mathbf{q}_0, \mathbf{q})\, e^{i\mathbf{q}\cdot\mathbf{r}}$$

with Fourier coefficients $C(\mathbf{q}_0, \mathbf{q})$ determined by

$$C(\mathbf{q}_0, \mathbf{q}) = \frac{1}{(2\pi)^3} \int d^3r \Psi'(\mathbf{q}_0, \mathbf{r})\, e^{-i\mathbf{q}\cdot\mathbf{r}}$$

The microcrystal phonon wavefunction is a superposition of eigenfunctions with $\mathbf{q}$ vectors centered at $\mathbf{q}_0$. Putting $\mathbf{q}_0 = 0$, the first order Raman spectrum is, then, calculated as

$$I(\omega) \sim \int \frac{d^3q\, |C(0, \mathbf{q})|^2}{(\omega - \omega(\mathbf{q}))^2 + (\Gamma_0/2)^2}$$

where $\omega(\mathbf{q})$ is the phonon dispersion curve and Γ_0 is the natural linewidth. Spherical Brillouin zone is used for simplicity and photon dispersion is assumed to be isotropic.

The calculated results were then fitted to the experimental data: the measured Raman spectra and the X-ray diffraction data on the crystal sizes. As for the condition for the α parameter, the authors of [146] found the boundary condition $W = \exp(-4\pi^2)$ to produce the best fit.

Appendix D.
Block-scheme for computer simulation of connectivity of random 3D net

Connectivity along a sample column is studied in an orthogonal 3D net, with the cross-section of the column being 120 × 80 cells. Zero or unity conductivity is assigned to each cell with a chosen probability ρ. In algorithmic terms, conductive cells are *the knots* randomly positioned in a 3D net, and the insulating cells are empty spaces in-between. Connections are only possible between the adjacent knots. In this simplified model the cells are cubic, that is why three types of contact of the nearest cells are possible: with cube faces, with edges and with corners. The probabilities of contact for these types of mutual positioning were assigned as 1, α and 0 respectively, where α is a variable *weight* for the edge connectivity. Charge transfer through corners is disregarded. The calculation propagates along the column from layer to layer as shown in a scheme below, marking the contacted cells out of the number of conducting cells, with only the two last calculated layers and a current layer being kept in memory at each moment. The number of contacted cells is monitored. Propagation stops when there is no contacted cell found in the current layer.

The block-scheme for the used process of computer simulation of connectivity through the 2-component layered media is shown in Figure 79. The part of the scheme shown in black corresponds to the description above, which includes only the *forward* (current-to-next-layer) and *in-layer* propagation. An additional loop was incorporated into the algorithm as shown in grey to account (in the first order) for the *back-propagation*. This covers for rare occasions, such as when after all the contacts have been traced within the current layer, new contacts may arise to the conductive cells belonging to the previous layer. If this is the case, the propagation of the new contacts within the previous layer are to be traced, and the *forward contacts* (from the previous to the current layer) should be checked again. This, possibly, adds new contacted cells to the current layer and, consequently new propagation within the current layer. The algorithm is organised in such a way that this two-layer propagation is simulated until no new contacts are found during such a cycle. Only when two-layer propagation has stopped, is the new layer defined, the current layer is kept and the previous layer is removed from memory. A question may arise here as to the back-propagation for

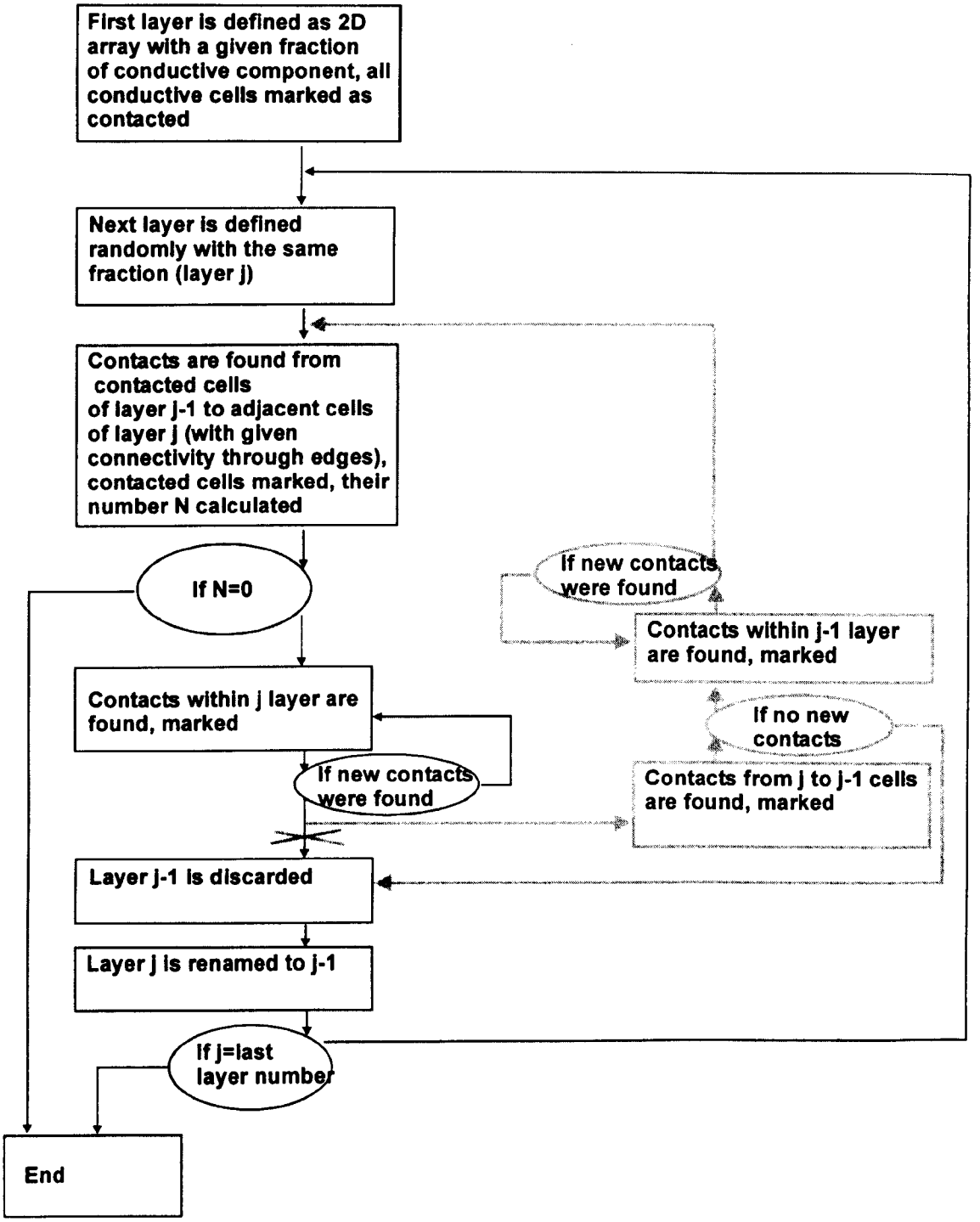

Figure 79. Block-scheme for the process of computer simulation of connectivity through the random layered two-component network.

more than one layer back. It is impossible to define the relative effect of such paths on the final result without a separate serious study. However, for the present needs, which is the modelling of electrical conductivity or tunneling through the random network, such backward paths can be simply disregarded on the following grounds: there exists a preferential direction for the carrier propagation, defined by the direction of applied electric field (or by the voltage difference applied to the first and the last layers), and the backward propagation of carriers is much less likely in this situation.

Appendix E.
Mean force on atom in electromagnetic field

Full derivation of (3.40) used in section 3.7 can be found in [161]. Here, for those interested, only an outline of the procedure is reproduced.

The Hamiltonian for a system of atom in an optical field is taken as:

$$H = H_{field} + \frac{\overrightarrow{P}^2}{2m} + \hbar\omega_0\sigma_{22} - \overrightarrow{\mu} \cdot \overrightarrow{E} \tag{E.1}$$

where σ_{22} is the population of the top atomic level, μ is the atomic dipole moment, and E is the electric field. Arrows above all vector values will be omitted in the following.

Quantum-mechanical notations $E = Ee^{-i\omega t} + E^+e^{i\omega t}$ and $\mu = \mu_{12}\sigma e^{-i\omega t} + \mu_{21}\sigma^+e^{i\omega t}$ are used to approximate the dipole interaction term for two-level atoms as:

$$\mu E = \left(\mu_{12} \cdot E^+\right)\sigma + \sigma^+\left(\mu_{21} \cdot E\right)$$

where σ is the lowering operator of the atomic state.

The equation for the force on the atom is written down as

$$f \equiv \frac{dP}{dt} = -\frac{i}{\hbar}[P, H] = -grad\,(H) = \sigma^+ grad\,(\mu_{21} \cdot E) + h.c. \tag{E.2}$$

The equations of motion for two more atomic operators are then written down:

$$\frac{d\sigma}{dt} = -\frac{i}{\hbar}[\sigma, H] = i\Omega\sigma + \frac{i}{\hbar}D\left(\mu_{21} \cdot E\right) \tag{E.3}$$

$$\frac{dD}{dt} = -\frac{i}{\hbar}[D, H] = \frac{2i}{\hbar}\left[\left(\mu_{12} \cdot E^+\right)\sigma - \sigma^+\left(\mu_{21} \cdot E\right)\right] \tag{E.4}$$

where $D = \sigma_{11} - \sigma_{22}$ is the population difference and $\Omega = \omega - \omega_0$ is the detuning of atomic resonance ω_0 from the field frequency ω. The above three equations are than solved together.

The next important point is the *reaction field approximation*: field E is separated into two parts, external incident field E_0 and the local reaction field of the atomic dipole oscillation:

$$E = E_0 + i\frac{2}{3}\left(\frac{\omega}{c}\right)^3 \mu_{12}\sigma \tag{E.5}$$

The reaction field has no gradient at the atom's position, that is why the force (E.2) can be described as

$$f = -i\hbar\sigma^+ gradG + h.c. \tag{E.6}$$

where $G \equiv i\mu_{21}E_0/\hbar$. Equations (E.3) and (E.4) are modified with the help of (E.5) to the form:

$$\frac{d\sigma}{dt} + \left(\frac{\Gamma}{2} - i\Omega\right)\sigma = DG \tag{E.7}$$

$$\frac{dD}{dt} + \Gamma D = \Gamma - 2\left(G^+\sigma + \sigma^+ G\right) \tag{E.8}$$

where $\Gamma = (4/3\hbar)(\omega/c)^3 |\mu_{12}|^2$ is the natural radiative decay rate of the atom.

The same equations are then shown to be valid for quantum expectation values $\langle f\rangle$, $\langle\sigma\rangle$ and $\langle D\rangle$ of f, σ and D. Brackets " $< .. >$ " will be omitted in the following, all three variables meaning the expectation values.

Notations $g = \langle G\rangle$ and $grad(g) = (\alpha + i\beta)g$ are than introduced. Equation (E.6) now looks as

$$f = \alpha\left[i\hbar\left(g^+\sigma - g\sigma^+\right)\right] + \hbar\beta\left(g^+\sigma + g\sigma^+\right) \tag{E.9}$$

The solution of (E.9), (E.7) and (E.8) (all written down for expectation values) for the case of a monochromatic field $Ee^{-i\omega t}$ and a motionless atom are then found as

$$f = \hbar\frac{p}{1-p}\left(-\Omega\alpha + \Gamma\beta/2\right) \tag{E.10}$$

$$\sigma = \frac{g}{\gamma(1+p)} \tag{E.11}$$

$$D = \frac{1}{1+p} \tag{E.12}$$

where $\gamma \equiv \Gamma/2 - i\Omega$ and $p \equiv 2|g|^2/|\gamma|^2$ (the saturation parameter).

As the next step, the first order velocity dependence of the force is examined. For this purpose, the first time derivatives of solutions (E.11) and (E.12) are taken with the use of

$$\frac{dg}{dt} = v\cdot(\alpha + i\beta)g$$

where v is the velocity vector. These velocity-dependant first derivatives are than substituted into (E.9), (E.7) and (E.8) (expectation values), which are than solved again to find the modified force.

Limiting this consideration to the case of a pure standing wave $g = 2g_0\cos(k\cdot x)$, where $\beta = 0$ and $\alpha = -k\tan(k\cdot x)$ the following result is obtained:

$$f = \frac{\hbar p}{1+p}\left[\Omega k\tan(k\cdot x)\right]\left(1 + \frac{\Gamma^2(1-p) - 2p^2|\gamma|^2}{\Gamma|\gamma|^2(1+p)^2}(v\cdot k)\tan(k\cdot x)\right) \tag{E.13}$$

where p represents the local value of the saturation parameter. Substitution of standing wave value $p = 4p_0\cos^2(k\cdot x)$, where p_0 is the saturation parameter corresponding to

one of the two oppositely directed travelling waves that compose the standing wave, modifies the solution (E.13) to the form (3.40) used in section 3.7.

Appendix F.
Computer simulation of atomic trajectories

The process of computer simulation of atomic trajectories in the velocity-dependent field can be described as follows. An array of intervals $[x_j, x_{j+1}]$ is defined along the substrate corresponding to the physical distance of 3 wavelengths λ. Then the following cycle is performed for each of the required number of atoms (some of the variables are shown in Figure 80, top-right insert):

1. An atom is placed above the substrate at a height h_0 equal to the radius of the laser beam R with the random transversal position x_0 along the optical beams (along the standing wave).

2. Vertical (towards the substrate, perpendicularly to the beams) velocity of atom v is randomly defined with Gaussian probability distribution $P \sim \exp\left[-\left(v - v_0\right)^2 / \left(\delta v\right)^2\right]$ of a controlled width δv centered at a thermal velocity $v_0 = \sqrt{2k_B T/m}$

3. Transversal (along the standing wave) velocity v_x is randomly defined between 0 and αv, where α is the given divergence of the atomic beam.

4. Time-step for the atom is calculated as $\delta t = R/\left(100 \times v\right)$ dependent on the vertical velocity v, allowing 100 steps within the beam radius (until the atom hits the substrate).

5. The trajectory of atom (x_i, h_i) where $i = 0, 1, 2, ...100$ is simulated with the stable numerical scheme $x_{i+1} = 2x_i - x_{i-1} + F\left(\delta t\right)^2 / m$, $h_{i+1} = h_i - v \times \delta t$, where the force $F = F\left(x, h\right)$ is calculated for each time step using equation (3.40) with the local value for $p\left(h, x\right)$ and the current value for v_x (denoted v in (3.40)).

6. The position where an atom hits the substrate $x_{100} = x\left(h = 0\right)$ is recorded. The counter N_j of the corresponding interval $[x_j, x_{j+1}]$ is increased by one.

7. Atom (or trajectory) counter is increased by 1.

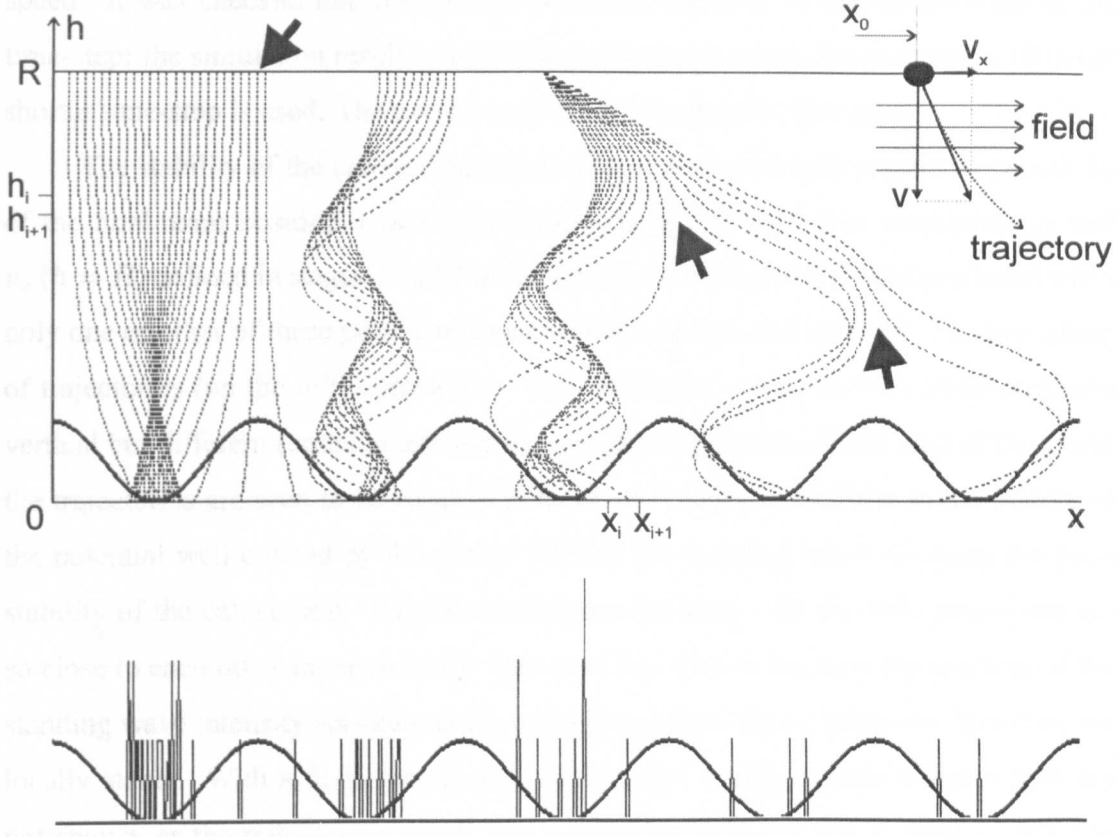

Figure 80. Illustration of the effect of starting position (trajectories on the left) and of starting transversal velocity (trajectories on the right) of the atom on the final simulated position on the surface.

The cycle is repeated until the atom counter reaches the given total number of trajectories. If at some point of the trajectory an atom goes out of the considered interval ($x_i < 0$ or $x_i > 3\lambda$) the program proceeds with the next atom and non of N_j is increased. The deposited shape $N_j(x_j)$ is plotted after each 100 atoms have been processed or/and after the given number of trajectories has been simulated. The graph is normalised so that the height does not depend on the number of atoms. The user is given an option to smooth the curve after the simulation is finished. This smoothing corresponds physically to the diffusion of atoms across the surface after the deposition, an effect which was mentioned in the original works [71] and [162]. The trajectories are not kept in computer memory but stay displayed on the screen.

As it is defined in stage 4 of each atom's cycle, the time-step δt is calculated so that there are 100 steps to the substrate from the starting position. This is done with the purpose to produce equally smooth trajectories for each atom no matter the vertical

speed. It was checked that the calculation is not sensitive to further decrease of the time-step: the simulation result is qualitatively the same when, for example, a 10-times shorter time-step is used. The overall process time, naturally, increases.

The stability of the calculation results was also studied with respect to sensitivity of the final atom position $x\,(h = 0)$ to small change of the initial conditions x_0 and $v_x\,(h = R)$ defined in stages 1 and 3 of the cycle. An example of results produced when only one or other of these parameters was varied is shown in Figure 80. The first group of trajectories (on the left) corresponds to equal initial velocities both transversal and vertical but different (equidistant) starting x-positions. In the middle part of the group the trajectories are seen to be roughly parallel with uniform focusing in the middle of the potential well created by the optical field of the standing wave, showing the good stability of the calculation. The side trajectories (marked with the bold arrow) are not so close to each other in terms of the final position. This is because the gradient of the standing wave intensity was zero at the starting position. The trajectories, however, are locally stable. With a finer spatial step between the starting points (these results are not shown, as the trajectories would merge together on the picture), there is only one *unusual* point (near the arrow mark) where the trajectory is extremely sensitive to the starting position: it bends toward the left or right potential minimum with negative or positive infinitesimal δx_0 perturbation. This is a classic effect of *unstable equilibrium*, when a ball may end up on any side of the hill if positioned on the top at rest. In all the other areas the trajectories close to each other in the starting point x_0 come to close final positions x_f separated by δx_f, which can always be made small enough by the choice of a sufficiently small δx_0. The same is true for the second group of trajectories which, again, correspond to the same starting velocities and different horizontal positions, but the vertical velocity is 5 times lower than that of the first group of trajectories. These atoms have more time to oscillate in the potential field before hitting the substrate, but the trajectories are still essentially parallel. All the trajectories initiated between any two shown in Figure 80 would finish between the same two trajectories.

The third group of trajectories corresponds to the initial conditions when the starting position is the same, but the transversal velocities $v_x\,(h = R)$ are assigned to a set of equidistant values. Similarly, there are seen two *unusual* values $v_x\,(R)$ of unstable equilibrium where the atom can be "trapped" to either left or right potential well depending on the infinitesimal negative or positive δv_x respectively. The trajectories corresponding

to these conditions are not shown implicitly (too fine a step of v_x is needed to visualise those), but the arrows designate the positions where these unstable trajectories would pass. It is interesting that the trajectory immediately to the left from the middle arrow is essentially apart from all the other trajectories of the group. It probably corresponds very closely to the critical value of v_x. For any pair of neighboring trajectories not involving those next to the arrows the same stability statement is true: the difference in a final atom position on the surface δx_f can be made infinitely small by the choice of small enough δv_x.

Thus, the conclusion is that the simulation algorithm is stable. There are some specific situations when the final result is unstable (infinitesimal changes to the starting parameters lead to finite differences in the final positions), but this instability has a physical nature, rather than computational.

References

1. E. by P. Malinverni, *Optoelectronic interconnects for integrated circuits*, Publications of the European Communities, Brussels, 1998.

2. A. L. Lentine and D. J. Reiley, Appl. Opt. 36, 1804 (1997).

3. N. Bar-Chaim and A. Yariv, Appl. Phys. Lett. 41, 126 (1982).

4. C. Pickering, V. Beale, D. Robbins, P. Pearson, and R. Greef, J. Phys. C, Solid State Phys. 17, 6535 (1984).

5. D. Gill, C. Conrad, G. Ford, B. Wessels, and S. Ho, Appl. Phys. Lett. 71, 1783 (1997).

6. C. Buchal and M. Loken, MRS Bulletin 23(4), 55 (1998).

7. A. Uhlir, Bell Systen Tech. J. 35, 333 (1956).

8. L. T. Canham, Appl. Phys. Lett. 57, 1046 (1990).

9. L. Tsybeskov and P. Fauchet, Appl. Phys. Lett. 68, 2058 (1996).

10. J. Glass, E. Wovchko, and J. Yates, Surf. Sci. 348, 325 (1996).

11. S. C. Bayliss and L. Buckberry, Materials world 7, 213 (1999).

12. J. Palm, F. Gun, B. Zheng, J. Mickel, and L. Kimerling, Phys. Rev. B 54, 17603 (1996).

13. S. Coffa and F. Priolo, MRS Bulletin 23(4), 24 (1998).

14. S. Lazarouk, P. Jaguiro, and V. Borisenko, Phys. Stat. Sol. A 165, 87 (1998).

15. N. Gaponenko et al., J. of Lumin. 80, 399 (1998).

16. L. Brus and P. Szajowsky, J. Am. Chem. Soc. 117, 2915 (1995).

17. L. Tsybeskov et al., Appl. Phys. Lett. 72(1), 43 (1998).

18. L. Banyai and S. W. Koch, *Semiconductor Quantum Dots*, World Scientific Pablisking Co. Pte. Ltd, Singapore, 1993.

19. A. Yariv, *Theory and Applications of Quantum Mechamics*, John Wiley and Sons, Inc., 1982.

20. A. S. Grove, *Physics and Technology of Semiconductor Devices*, John Willey and Sons, Inc., USA, 1967.

21. W. Schottky, Naturwissenchaften 26, 843 (1938).

22. E. H. Rhoderick, *Metal-semiconductor contacts*, Clarendon Press, Oxford, 1978.

23. L. Canham et al., Thin Solid Films 276, 112 (1996).

24. H. Koyama and N. Koshida, Solid State Commun. 103, 37 (1997).

25. A. G. Gullis, L. T. Canham, and P. D. J. Calcott, J. Appl. Phys. 82, 3, 909 (1997).

26. J. C. Vial et al., Phys. Rev. B 45, 14171 (1992).

27. F. Koch, V. Petrova-Koch, T. Muschik, A. Nikolov, and V. Gavrilenko, Mater. Res. Soc. Symp. Proc. 283, 197 (1993).

28. F. Koch, Microelectron. Eng. (Netherlands 28, 237 (1995).

29. C. Tsai et al., Appl. Phys. Lett. 59, 2814 (1991).

30. S. M. Prokes et al., Phys. Rev. B 45, 13788 (1992).

31. M. S. Brandt, H. D. Fuchs, M. Stutzmann, J. Weber, and M. Cardone, Solid State Commun. 81, 307 (1992).

32. Y. Kanemitsu et al., Appl. Phys. Lett. 61, 2446 (1992).

33. S. Hayashi, M. Kataoka, and K. Yamamoto, Jpn. J. Appl. Phys. 32, L224 (1993).

34. M. Sacilotti, P. Abraham, B. Champignon, Y. Montail, and J. Bouix, Electron. Lett. 29, 970 (1993).

35. C. Wang, J. Perz, F. Gaspari, M. Plumb, and S. Zukotinski, Appl. Phys. Lett. 62, 2676 (1993).

36. V. Petrova-Koch et al., Appl. Phys. Lett. 61, 943 (1992).

37. Y. Kanemitsu, Phys. Rev. B 48, 12357 (1993).

38. F. Koch, Silicon-Based Optoelectronic Materials Sypm. Proc., Pittsburg 298 (1993).

39. J. Rehm, G. McLendon, and P. Fauchet, *Advanced Luminescent Materials*, The Electrochem. Soc., Pennington, 1996.

40. F. Koch and V. Petrova-Koch, J. of Non-cryst. Solids 198-200, 840 (1996).

41. J. Gole, F. Dudel, D. Grantier, and D. Dixon, Phys. Rev. B 56, 2137 (1997).

42. J. L. Gole and D. A. Dixon, Phys. Rev. B 57, 12002 (1998).

43. D. Lockwood, Solid State Commun. 92, 101 (1994).

44. M. Enachescu, E. Hartmann, and F. Koch, Appl. Phys. Lett. 64, 1365 (1994).

45. S. Schuppler et al., Phys. Rew. Lett. 72, 2648 (1994).

46. Q. Zhang and S. C. Bayliss, J. Appl. Phys. 79(3), 1351 (1995).

47. K. J. Nash, P. D. J. Calcott, L. T. Canham, M. J. Kane, and D. Brumhead, J. of Lumin. 60, 297 (1994).

48. P. Calcott, K. Nash, L. Canham, M. Kane, and D. Brumhead, J. of Lumin. 57, 257 (1993).

49. D. Kovalev, G. Polisski, M. BenChorin, J. Diener, and F. Koch, J. of Appl. Phys. 80, 5978 (1996).

50. D. Kovalev et al., Phys. Rev. B 57, 3741 (1998).

51. D. Kovalev, H. Heckler, M. BenChorin, G. Polisski, and F. Koch, Phys. Rev. B 81, 2803 (1998).

52. J. Vial et al., Phys. Rev. B 45, 14171 (1992).

53. D. Kovalev et al., Phys. Rev. Lett. 77, 2089 (1996).

54. D. Kovalev et al., Thin Solid Films 276, 120 (1996).

55. D. Kovalev et al., Phys. Rev. Lett. 79, 119 (1997).

56. D. Kovalev, B. Averboukh, M. BenChorin, F. Koch, and G. Polisski, J. of Lumin. 70, 320 (1996).

57. D. Kovalev, B. Averboukh, F. Koch, and G. Polisski, Appl. Phys. Lett. 70, 1116 (1997).

58. M. Wolkin, J. Jorne, P. Fauchet, G. Allan, and C. Delerue, Phys. Rev. B 82, 197 (1998).

59. A. J. Kenyon, P. F. Twoga, C. W. Pitt, and G. Rehm, Appl. Phys. Lett. 73(4), 523 (1998).

60. E. Edelberg, S. Bergh, R. Naone, M. Hall, and E. Aydil, Appl. Phys. Lett. 68, 1415 (1996).

61. T. ShimizuIwayama, N. Kurumado, D. Hole, and P. Townsend, J. of Appl. Phys. 83, 6018 (1998).

62. S. Guha, M. Pace, D. Dunn, and I. Singer, Appl. Phys. Lett. 70, 1207 (1997).

63. T. ShimizuIwayama, D. Hole, and P. Townsend, J. of Lumin. 80, 235 (1999).

64. P. Knapek et al., E-MRS 1998 procedings to be published .

65. Q. Zhang, S. Bayliss, and D. Hutt, Appl. Phys. Lett. 66, 1977 (1995).

66. L. Patrone, D. Nelson, V. Safarov, M. Sentis, and W. Marine, J. of Lumin. 80, 217 (1998).

67. L. Patrone, D. Nelson, V. Safarov, M. Sentis, and W. Marine, J. of Lumin. 80, 217 (1999).

68. M. Ehbrecht, B. Kohn, F. Huisken, M. Laguna, and V. Paillard, Phys. Rev. B 56, 6958 (1997).

69. Y. Guyot et al., Thin Solid Films 297, 188 (1997).

70. L. Dinh, L. Chase, M. Balooch, W. Siekhaus, and F. Wooten, Phys. Rev. B 54, 5029 (1996).

71. R. E. Scholten, J. J. McClelland, E. C. Palm, A. Gavrin, and R. J. Celotta, J. Vac. Sci. Technol. B 12, 1847 (1994).

72. L. T. Canham, W. Y. Leong, M. I. J. Beale, T. I. Cox, and L. Taylor, Appl. Phys. Lett. 61, 2563 (1992).

73. E. Lebedev, E. Smorgonskaya, and G. Polisski, Phys. Rev. B 57, 14607 (1997).

74. L. T. Canham, M. R. Houlton, W. Y. Leong, C. Pickering, and Keen, J. Appl. Phys. 70, 422 (1991).

75. R. Schwarz et al., Thin Solid Films 255, 23 (1995).

76. M. Ben-Chorin, F. Moller, and F. Koch, Phys. Rev. B 49, 2981 (1994).

77. B. Hamilton et al., Nature 393, 443 (1998).

78. H. Koyama and N. Koshida, J. Lumin. 57, 293 (1993).

79. M. Ben-Chorin, F. Moller, and F. Koch, J. Lumin. 57, 159 (1993).

80. L. Canham, M. Houlton, W. Leong, C. Pickering, and J. Keen, J. of Appl. Phys. 70, 422 (1991).

81. F. Moller, M. BenChorin, and F. Koch, Thin Solid Films 255, 16 (1995).

82. L. Pavesi, M. Ceschini, and H. Roman, Thin Solid Films 255, 67 (1995).

83. T. Matsumoto, J. Qi, Y. Masumoto, H. Mimurf, and N. Koshida, J. of Lumin. 80, 203 (1999).

84. A. Kux and M. Ben-Chorin, Phys. Rev. B 51, 17535 (1995).

85. P. Fauchet, IEEE J. of Selected Topics in Q. El. 4, 1020 (1998).

86. R. Swisher, R. G.L., and P. Sercel, J. of Chem. Edu. 73, 738 (1996).

87. P. Fauchet et al., IEEE J. of Selected Topics in Q. El. 1, 1126 (1995).

88. A. Loni, A. Simons, C. T.I., P. Calcott, and L. T. Canham, El. Lett. 31, 1288 (1995).

89. L. Canham, T. Cox, A. Loni, and A. Simons, Appl. Surf. Sci. 102, 436 (1996).

90. A. J. Simons, T. I. Cox, A. Loni, L. Canham, and R. Blacker, Thin Solid Films 297, 281 (1997).

91. E. Squire et al., J. of Lumin. 80, 125 (1998).

92. A. Loni et al., Thin Solid Films 276, 143 (1995).

93. A. Loni, IEE Colloq. Microengineering Applications in Optielectronics (UK) 39, 8 (1996).

94. M. Araki, H. Koyama, and N. Koshida, Appl. Phys. Lett. 68, 2999 (1996).

95. C. Mazzoleni and L. Pavesi, Appl. Phys. Lett. 67, 2983 (1995).

96. M. Araki, H. Koyama, and N. Koshida, Japan. J. Appl. Phys. 35, 1041 (1996).

97. V. Pellergini, A. Tredicucci, C. Mazzoleni, and L. Pavesi, Phys. Rev. B 52, R14328 (1995).

98. L. Pavesi, R. Guardini, and C. Mazzoleni, Solid State Commun. 97, 1051 (1996).

99. J. Zheng, K. Jiao, W. Shen, W. Anderson, and H. Kwok, Appl. Phys. Lett. 61, 459 (1992).

100. M. Kruger et al., Thin Solid Films 297, 241 (1997).

101. A. Einstein, Phys. Lett. 18, 121 (1917).

102. P. Knapek et al., Phys. Stat. Solidi A 167, R5 (1998).

103. S. School, *Silicon based nanophotonics: from basics to applications*, Italian Physical Society, Varenna, Italy, 1998.

104. M. Abramowits and I. Stegun, *Handbook of Mathematical Functions*, Dover Publications Inc., New York, 1970.

105. N. Peyghambarian and S. W. Koch, *Nonlinear Photonics*, Springer Verlag, Berlin, 1990.

106. S. W. Koch, Phys. B1 46, 167 (1990).

107. S. F. Klingshirn, *Semiconductor Optics*, Springer-Verlag, Berlin Heidelberg, 1995.

108. D. B. Thoai, R. Zimmermann, M. Grundmann, and D. Bimberg, Phys. Rev B42, 5906 (1990).

109. Y. Z. Hu, M. Lindberg, and S. W. Koch, Phys. Rev. B42, 1713 (1990).

110. P. E. Lippens and M. Lannoo, Phys. Rev. B39, 10935 (1989).

111. A. J. Read et al., Phys. Rev. Lett. 69, 1232 (1992).

112. A. J. Read et al., Phys. Rev. B 50, 14223 (1994).

113. A. B. Filonov, G. V. Petrov, V. A. Novikov, and V. E. Borisenko, Appl. Phys. Lett. 67, 1090 (1995).

114. S. Ossicini, L. Dorigoni, and O. Bisi, Appl. Surf. Sci. 102, 395 (1996).

115. T. Takagahara and K. Takeda, Phys. Rev. B 46, 15578 (1992).

116. R. A. Street, Adv. Phys. 30, 593 (1981).

117. G. Allan, C. Delerue, and M. Lanoo, Phys. Rev. Lett. 78, 3161 (1997).

118. L. Wang and A. Zunger, Studies in Surf. Sci. and Catalysis 103, 161 (1997).

119. R. L. Smith and C. D. Collins, J. Appl. Phys. 71, R1 (1992).

120. V. Lehmann and U. Gosele, Adv. Mater. 4(2), 114 (1992).

121. J. Chazalviel, M. Etman, and F. Ozaman, J. Electroanal. Chem. 297, 533 (1991).

122. D. V, Surf. Sci. 274, 82 (1992).

123. V. Lehmann and U. Gosele, Appl. Phys. Lett. 58(10), 856 (1991).

124. X. G. Zhang, J. Electrochem. Soc. 138, 3750 (1991).

125. Y. Kang and J. Jorne, J. Electrochem. Soc. 140, 2258 (1993).

126. A. Valence, Phys. Rev. B 52, 8323 (1995).

127. M. Beale, J. Benjamin, J. Uren, N. Chew, and A. Gullis, J. Cryst. Growth 73, 622 (1985).

128. P. Allongue, C. H. de Vilaneuve, L. Pinsard, and M. Bernard, Appl. Phys. Lett. 67, 691 (1995).

129. C. Corbett, D. Shereshevsky, and I. Verner, Phys. Status Solidi A 147, 81 (1995).

130. M. E. Kompan, E. G. Kuz'minov, V. B. Kulik, and V. I. Beklemyshev, JETP Lett. 64, 748 (1996).

131. A. G. Nassiopolous et al., Thin Solid Films 255, 329 (1995).

132. S. C. Bayliss et al., Thin Solid Films 255, 128 (1995).

133. N. Noguchi and I. Suemune, Appl. Phys. Lett. 62, 1429 (1993).

134. A. Starovoitov and S. Bayliss, Appl. Organometal. Chem. 12, 337 (1998).

135. A. Starovoitov and S. Bayliss, Appl. Phys. Lett. 73, 1284 (1998).

136. V. Lehmann, Thin solid Films 255, 1 (1995).

137. L. T. Canham et al., Nature (UK) 368, 133 (1994).

138. U. Gruning and A. Yelon, Thin Solid Films 255, 135 (1995).

139. O. Belmont, D. Bellet, and Y. Brechet, J. Appl. Phys. 79, 7586 (1996).

140. H. Blumer, Z. f. Phys. 38, 304 (1926).

141. G. Lerondel, R. Romestain, and J. C. Vial, Appl. Phys. Lett. 71, 196 (1997).

142. H. Munder et al., Thin Solid Films 221, 27 (1992).

143. R. Tsu, H. Shen, and M. Dutta, Appl. Phys. Lett. 60, 112 (1992).

144. R. Tsu, J. Gonzales-Hernandez, S. Chao, S. Lee, and K. Tanaka, Appl. Phys. Lett. 40, 534 (1982).

145. E. Bustarret, M. Hachicha, and M. Brunel, Appl. Phys. Lett. 52, 1675 (1988).

146. I. H. Campbell and P. M. Fauchet, Solid State Commun. 58, 739 (1986).

147. C. Ossadnik, S. Veprek, and I. Gregora, Thin Solid Films 337, 148 (1999).

148. F. Sarott, Z. Iqbal, and S. Veprek, Solid State Commun. 42, 465 (1982).

149. A. Andrianov, G. Polisski, J. Morgan, and F. Koch, J. of Lumin. 80, 193 (1999).

150. L. D. Landau, E. M. Lifshiz, and L. P. Pitaevskii, *Electrodynamic of Continuous Media*, Pergamon, Oxford, 1984.

151. D. Kovalev et al., Appl. Phys. Lett. 67, 1585 (1995).

152. V. Karavenskii et al., JETP Lett. 57, 239 (1993).

153. A. G. Cullis and C. L. T., Nature (London) 353, 335 (1991).

154. A. Yariv, *Optical Electronics*, Saunders College Publishing, a division of Holt Rinehart and Winston, Inc., USA, 1991.

155. S. Ossicini, Phys. Stat. Solidi, A 170, 377 (1998).

156. R. Sedgewick, *Algorithms*, Addison-Wesley Publishing Company, Inc., USA, 1988.

157. T. W. Hansch and A. L. Schawlow, Opt. Commun. 13, 68 (1975).

158. V. S. Letokhov, V. G. Minogin, and B. D. Pavlik, Opt. Commun. 19, 72 (1976).

159. A. Chiou, W. Wang, G. Sonek, J. Hong, and M. Berns, Opt. Commun. 133, 7 (1997).

160. V. I. Balykin and V. S. Letokhov, Opt. Commun. 64, 151 (1987).

161. J. Gordon and A. Ashkin, Phys. Rev. A 21, 1606 (1980).

162. R. Gupta, J. McClelland, Z. Jabbour, and R. Celotta, Appl. Phys. Lett. 67, 1378 (1995).

163. J. J. McClelland, J. Opt. Soc. Am. B 12, 1763 (1995).

164. A. Starovoitov and S. Bayliss, CMMP, Institute of Physics Programme and Abstracts, 69 (1996).

165. J. McClelland, R. Gupta, Z. Jabbour, and R. Celotta, Aust. J. Phys. 49, 555 (1996).